Die approbierte gedruckte Originalversion dieser Dissertation ist an der TU Wien Bibliothek verfügbar.
The approved original version of this doctoral thesis is available in print at TU Wien Bibliothek.

TECHNISCHE UNIVERSITÄT WIEN

DISSERTATION

Drops dynamics and heat transfer in turbulence

carried out for the purpose of obtaining the degree of
Doctor technicae (Dr. techn.), submitted to the TU Wien,
Faculty of Mechanical and Industrial Engineering,
by

Francesca Mangani

Mat. Nr.: 12038071

under the supervision of
Univ.-Prof. Alfredo Soldati
Institute of Fluid Mechanics and Heat Transfer

Reviewed by:

Univ-Prof. Eric Climent
Université de Toulouse

Univ-Prof. Carole Planchette
Technische Universität Graz

This work has been partially supported by the MSCA-ITN-EID project COMETE (project no. 813948).

I confirm that going to press of this thesis needs the confirmation of the examination committee.

Affidavit

I declare in lieu of oath, that I wrote this thesis and performed the associated research myself, using only literature cited in this volume. If text passages from sources are used literally, they are marked as such. I confirm that this work is original and has not been submitted elsewhere for any examination, nor is it currently under consideration for a thesis elsewhere. I acknowledge that the submitted work will be checked electronically-technically using suitable and state-of-the-art means (plagiarism detection software). On the one hand, this ensures that the submitted work was prepared according to the high-quality standards within the applicable rules to ensure good scientific practice "Code of Conduct" at the TU Wien. On the other hand, a comparison with other student theses avoids violations of my personal copyright.

Vienna, May 2024

Francesca Mangani

Die approbierte gedruckte Originalversion dieser Dissertation ist an der TU Wien Bibliothek verfügbar.
The approved original version of this doctoral thesis is available in print at TU Wien Bibliothek.
TU Bibliothek Your knowledge hub WIEN

Die approbierte gedruckte Originalversion dieser Dissertation ist an der TU Wien Bibliothek verfügbar.
The approved original version of this doctoral thesis is available in print at TU Wien Bibliothek.
TU Bibliothek Your knowledge hub WIEN

Abstract

In this thesis, the dynamics and heat transfer of large and deformable drops in turbulence are numerically investigated. Direct Numerical Simulation (DNS) is used to resolve the turbulent flow and energy field, while Phase Field Method (PFM) is used to describe the interface behaviour. The first purpose of this work is to study the interaction between drops and turbulence, and in particular to understand how this interaction is affected by density and viscosity differences between the fluids. To this aim, a campaign of simulations of a drop-laden turbulent channel flow is performed, exploring several density and viscosity contrasts and two different surface tensions, and analysing the drops dynamics in terms of deformation, breakage and coalescence. We observe that the effects of density and viscosity are negligible when surface tension is sufficiently high, while they become more significant as surface tension is reduced. In the latter case, they visibly affect drops deformability in opposite ways: while increasing drops viscosity reduces drops deformability, increasing drops density enhances drops deformability. Viscosity, in particular, shows a stronger impact, affecting deformation as well as breakage and coalescence rates. On the contrary, density induces visible deformations of the interface, but does not show any influence on breakage and coalescence events. The flow modifications inside the drops are then evaluated in terms of turbulent kinetic energy (TKE). As expected, an increase of drops density produces a higher internal TKE, while an increase of viscosity causes a strong suppression of turbulence and a reduction of TKE. The drops internal flow can influence the mixing of the heat contained by the drops, and how fast it is transferred to the carrier fluid. The second purpose of this work is to provide a better understanding of this phenomenon, within the passive scalar approximation. The heat transfer in a drop-laden turbulent channel flow is studied by performing numerical simulations, where warm drops are released in a cold carrier fluid. Different Prandtl numbers are considered, which are changed by varying the thermal diffusivity, while keeping a constant momentum diffusivity. Computing the time behaviour of the drops and carrier fluid average temperatures, we find that an increase of Prandtl slows down the heat transfer process. These results are explained by deriving a simplified phenomenological model, showing that the time evolution of the drops average temperature is self-similar, and a universal behaviour can be found upon rescaling by $t/Pr^{2/3}$. This scaling can be explained via the boundary layer theory and is consistent with previous theoretical/numerical predictions. In the last part of this work, the study of heat transfer in drop-laden turbulence is extended to evaluate the influence of viscosity differences between the fluids on the heat transfer process. While keeping a constant density and thermal diffusivity, two viscosity contrasts are considered, in order to mimic respectively the cases of warm oil drops in cold water and warm water drops in cold oil. It is observed that in the oil phase, which is more viscous, the heat transfer is slowed down, while in the water phase, which is less viscous, the heat transfer is accelerated. These effects balance each other in the two cases, which therefore result in having an equal heat transfer rate.

Die approbierte gedruckte Originalversion dieser Dissertation ist an der TU Wien Bibliothek verfügbar.
The approved original version of this doctoral thesis is available in print at TU Wien Bibliothek.

Die approbierte gedruckte Originalversion dieser Dissertation ist an der TU Wien Bibliothek verfügbar.
The approved original version of this doctoral thesis is available in print at TU Wien Bibliothek.

Zusammenfassung

In dieser Arbeit werden die Dynamik und der Wärmeübergang großer und verformbarer Tropfen in Turbulenzen numerisch untersucht. Die Direkte Numerische Simulation (DNS) wird verwendet, um die turbulente Strömung und das Energiefeld aufzulösen, während die Phasenfeldmethode (PFM) verwendet wird, um das Grenzflächenverhalten zu beschreiben. Das erste Ziel dieser Arbeit ist es, die Wechselwirkung zwischen Tropfen und Turbulenzen zu untersuchen und insbesondere zu verstehen, wie diese Wechselwirkung durch Dichte- und Viskositätsunterschiede zwischen den Fluiden beeinflusst wird. Zu diesem Zweck wird eine Kampagne von Simulationen eines durch Tropfen beladenen turbulenten Kanalströmung durchgeführt, wobei verschiedene Dichte- und Viskositätskontraste sowie zwei verschiedene Oberflächenspannungen untersucht werden und die Tropfendynamik in Bezug auf Verformbarkeit, Auseinanderbrechen und Zusammenwachsen analysiert wird. Wir beobachten, dass die Effekte von Dichte und Viskosität vernachlässigbar sind, wenn die Oberflächenspannung ausreichend hoch ist, während sie bei reduzierter Oberflächenspannung signifikanter werden. In letzterem Fall beeinflussen sie die Verformbarkeit der Tropfen in entgegengesetzter Weise: Eine Erhöhung der Viskosität der Tropfen reduziert die Verformbarkeit, während eine Erhöhung der Dichte die Verformbarkeit der Tropfen erhöht. Insbesondere zeigt die Viskosität eine stärkere Auswirkung, die sowohl Verformung als auch das Auseinanderbrechen und das Zusammenwachsen beeinflusst. Im Gegensatz dazu verursacht die Dichte sichtbare Deformationen der Grenzfläche, hat aber keinen Einfluss auf das Auseinanderbrechen und das Zusammenwachsen. Die Strömungsänderungen innerhalb der Tropfen werden dann in Bezug auf die turbulente kinetische Energie (TKE) bewertet. Wie erwartet, führt eine Erhöhung der Dichte der Tropfen zu einer höheren internen TKE, während eine Erhöhung der Viskosität eine starke Unterdrückung der Turbulenz und eine Reduzierung der TKE verursacht. Die innere Strömung der Tropfen kann den Wärmeaustausch beeinflussen, der von den Tropfen enthalten ist, und wie schnell er auf die Trägerflüssigkeit übertragen wird. Das zweite Ziel dieser Arbeit ist es, ein besseres Verständnis dieses Phänomens im Rahmen der passiven Skalaren Annärherung zu erreichen. Der Wärmeübergang in einer durch Tropfen beladenen turbulenten Kanalströmung wird durch numerische Simulationen untersucht, bei denen warme Tropfen in eine kalte Trägerflüssigkeit freigesetzt werden. Es werden verschiedene Prandtl-Zahlen betrachtet, die durch Variation der thermischen Diffusivität geändert werden, während eine konstante Impulsdiffusivität beibehalten wird. Durch Berechnung des zeitlichen Verhaltens der durchschnittlichen Temperaturen der Tropfen und des Trägerfluids finden wir heraus, dass eine Erhöhung der Prandtl-Zahl den Wärmeübertragungsprozess verlangsamt. Diese Ergebnisse werden durch Ableitung eines vereinfachten phänomenologischen Modells erklärt, das zeigt, dass die zeitliche Entwicklung der durchschnittlichen Temperatur der Tropfen selbstähnlich ist und ein universelles Verhalten durch Skalierung mit t/Pr2/3 gefunden werden kann. Diese Skalierung kann durch die Grenzschichttheorie erklärt werden und ist mit früheren theoretischen/numerischen Vorhersagen konsistent. Im letzten

Teil dieser Arbeit wird die Untersuchung des Wärmeübergangs in durch Tropfen beladener Turbulenz erweitert, um den Einfluss von Viskositätsunterschieden zwischen den Fluiden auf den Wärmeübertragungsprozess zu bewerten. Bei konstanter Dichte und thermischer Diffusivität werden zwei Viskositätskontraste betrachtet, um jeweils die Fälle warmer Öltropfen in kaltem Wasser und warmer Wassertropfen in kaltem Öl zu imitieren. Es wird beobachtet, dass im öligen Phasen, das viskoser ist, der Wärmeübertrag verlangsamt wird, während im wässrigen Phasen, das weniger viskos ist, der Wärmeübertrag beschleunigt wird. Diese Effekte balancieren sich in den beiden Fällen aus, wodurch eine gleichmäßige Wärmeübertragungsrate resultiert.

Die approbierte gedruckte Originalversion dieser Dissertation ist an der TU Wien Bibliothek verfügbar.
The approved original version of this doctoral thesis is available in print at TU Wien Bibliothek.
TU Bibliothek Your knowledge hub WIEN

Contents

Die approbierte gedruckte Originalversion dieser Dissertation ist an der TU Wien Bibliothek verfügbar.
The approved original version of this doctoral thesis is available in print at TU Wien Bibliothek.
TU Bibliothek Your knowledge hub WIEN

Die approbierte gedruckte Originalversion dieser Dissertation ist an der TU Wien Bibliothek verfügbar.
The approved original version of this doctoral thesis is available in print at TU Wien Bibliothek.
TU Bibliothek Your knowledge hub WIEN

Die approbierte gedruckte Originalversion dieser Dissertation ist an der TU Wien Bibliothek verfügbar.
The approved original version of this doctoral thesis is available in print at TU Wien Bibliothek.

1 Introduction

Turbulent multiphase flows can be found in a great number of natural phenomena, such as ocean-atmosphere interaction, rain, clouds, waterfalls, geysers, as well as plenty of industrial applications including food processing, spray drying, combustion engines, nuclear reactors cooling and cavitating ship propellers. These flows are characterized by the simultaneous presence of two or more thermodynamic phases (gas, liquid or solid) of the same chemical component (e.g. water vapour in water or ice in water), or by the simultaneous presence of different components, that have either the same or a different thermodynamic phase (e.g. oil in water or air in water). The different phases or components are immiscible, therefore pure gas-gas or solid-solid mixtures are excluded from this category [38]. In two-phase liquid-liquid or gas-liquid systems, when the two immiscible fluids are mixed by turbulence, polydispersed drops or bubbles are formed. Such drops or bubbles, immersed in the continuous phase, are transported by the turbulent flow while they continuously deform, break up and coalesce between each other, due to their interaction with the turbulent structures. Likewise, the turbulent flow field can be modified by the drops/bubbles dynamics (drops hereinafter, without any loss of generality), even when their volume is very low with respect to the volume of the carrier fluid.

Deformation, breakup and coalescence, as well as turbulence modulation, are complex multiscale phenomena, depending on the turbulence intensity, namely on the Reynolds number Re (the ratio of inertial forces over viscous forces), and on the turbulence characteristics (e.g. homogeneity, isotropicity, presence of large-scale shear) [115]. In addition, these phenomena are strongly influenced by the thermophysical properties of the system, namely by the density, viscosity and surface tension of the two fluids. These factors are represented in dimensionless form respectively by the density ratio ρ_r (drops density over carrier fluid density), the viscosity ratio μ_r (drops viscosity over carrier fluid viscosity), and the Weber number We (ratio of inertial forces over surface tension forces). In particular, the important role of the Weber number has been widely confirmed by many studies [89], being surface tension the main opposer to the drop distortion driven by turbulent stresses. More recently several works showed the relevance of density and viscosity contrasts [47, 132], even if their roles and mechanisms still lack of a deep understanding [115].

All these factors compete between each other and have different impacts on deformation, breakup, coalescence and turbulence modifications, making them challenging to predict and fully comprehend. For instance, one of the difficulty in understanding the

causes of breakup and deformation resides in the fact that their occurrence potentially depends on large-scale shear and far-field eddies, as well as on the local turbulence around the drop [115, 159]. As in real applications turbulence is usually inhomogeneous and anisotropic, understanding the synergy between large scales and small local scales in generating breakups is crucial to model and predict these events. Similarly hard is the study of coalescence, which is intrinsically related to phenomena occurring at very small scales, namely to the drainage and rupture of the thin film emerging when two drops approach each other. From a numerical viewpoint, coalescence description lacks of accuracy and would therefore imply the coupling of continuum and molecular simulations or the use of subgrid models [149]. Together with these challenges, studies on the impact of drops dynamics on turbulence modulation or turbulent drag reduction bring further and interesting problems. As concerns turbulence modulation, the main questions are related to the influence of drops dynamics on the turbulent energy spectra [54], as well as to the impact of surface tension on the energy cascade [114, 37] and on vorticity generation [141]. Regarding turbulent drag reduction, several studies investigated the role of bubbles deformability [157, 96, 160] and of coalescence [28], which turned out to be important factors in reducing drag.

In many practical applications, turbulent drop-laden flows also include the presence of heat or the presence of a further substance, that, depending on the temperature gradient or on the concentration gradient respectively, can act as a passive scalar, being only transported and diffused by the flow, or as an active scalar, being transported and diffused while influencing the flow itself. Some examples are flows in heat exchangers and sprays in combustion engines [62], where heat transfer has a central role in the operation of the device, or the transport of CO_2 and oxygen in bubbly flows produced by breaking waves, as well as the washing of pollutants from gas streams in the scrubbing process. The main dimensionless parameter that characterizes the study of active or passive scalars is the Prandtl number, for heat transfer problems, or the Schmidt number, for mass transfer problems. They are defined as the ratio of the momentum diffusivity over the thermal or mass diffusivity, respectively, and therefore quantify the importance of the diffusion of the momentum with respect to the diffusion of the scalar (heat or mass).

While the behaviour of passive or active scalars in turbulent single-phase flows has been extensively analysed with experiments and simulations [83, 123], few studies investigate the mixing of a scalar in turbulent multiphase flows. The analysis of these flows results particularly difficult because of the presence of deformable interfaces which alter/mediate the heat and species transport and mixing. Moreover, phase changes like boiling, condensation [136], evaporation [39] and dissolution [76] often occur in such liquid-liquid or gas-liquid systems, and can be possibly modulated by the drops dynamics and by turbulence. Previous works on heat or mass transfer in two-phase flows mostly considered isolated drops and bubbles [39, 118, 52]. Instead, swarms of drops/bubbles have received less attention and only recently some works on passive scalar transport and active scalars/phase change have appeared [138, 70].

The aim of this thesis is to provide a deeper understanding of the drops-drops and drops-turbulence interaction in two-phase liquid-liquid or gas-liquid systems, with a particular attention at the role played by density and viscosity differences in the system. In addition, this thesis aims at investigating the evolution of a passive scalar in

Die approbierte gedruckte Originalversion dieser Dissertation ist an der TU Wien Bibliothek verfügbar.
The approved original version of this doctoral thesis is available in print at TU Wien Bibliothek.
TU Bibliothek Your knowledge hub WIEN

drop-laden turbulent flows, focusing on the heat transfer process between the phases. These problems will be investigated considering a swarm of drops (or bubbles) released in a turbulent channel flow.

The physics of turbulent dispersed multiphase flows is characterized by a wide range of scales in space and time, from the largest scale of the problem of $O(1m - 10m)$ (or even higher for many environmental applications), to the molecular scale of the interface of $O(1nm)$. This range, which therefore spans about 9 or more orders of magnitude, goes well beyond the range of scales of turbulent single-phase flows, and poses several challenges to both experiments and simulations [8]. From a numerical point of view, the resolution of the full range of scales appears still unfeasible, as modern high performance computing systems can deal at most with 3-4 orders of magnitude. Consequently, different numerical approaches have been developed in order to simulate this type of flows as accurately as possible. The main approaches differentiate between each other based on two criteria: the extent of resolved scales and the range of size of the simulated drops/bubbles [149]. A good description at the nanoscopic level is provided by molecular dynamics simulations, which properly describe the interfacial phenomena but can only simulate very small drops (nanoscopic drops) and do not consider turbulence. When turbulence is considered, instead, direct numerical simulations (DNS) or large eddy simulations (LES) must be employed: in the former the resolved range covers all the turbulent scales of the problem, down to the smallest one, the Kolmogorov scale, while the latter covers all the large scales and uses subgrid models for the small ones. These approaches can simulate larger drops but require specific methods to describe the behaviour of the interface, which is no more resolved down to the molecular level, but rather approximated as modelled at larger scales. A simplification can be introduced in DNS/LES approaches when the dispersed phase has a characteristic size which is below the Kolmogorov scale, namely drops can be assumed as point particles and Lagrangian Particle Tracking methods can be used. If drops are larger than the Kolmogorov scale, the motion and deformation of the interface caused by turbulence becomes non-negligible, therefore interface-resolved simulation methods must be employed to properly investigate the problem. The term "interface-resolved" means here that the interface motion and deformation are simulated, as drops are not pointwise, although they are resolved at the mesoscopic and macroscopic scales [149]. The methods used for the interface description in interface-resolved simulations can be categorized in interface tracking methods and interface capturing methods. In interface tracking methods the interface is defined instantaneously by a set of Lagrangian markers which are advected by the flow. Examples include the Front-Tracking method [155] and the Immersed boundary method [84]. Interface capturing methods, instead, uses an Eulerian concentration field to mark the different phases, thus the interface is defined as the iso-level of this concentration field. Among these, well known methods are Volume of Fluid [74], Level Set [117], Lattice Boltzmann [33] and Phase Field method [25, 26, 27].

Overall, interface-resolved DNS can be considered the most accurate numerical tool to investigate turbulent flows with large and deformable drops. Clearly, the high fidelity of such simulations is obtained at the expense of a higher computational power with respect to LES or Lagrangian Particle Tracking approaches. Moreover, while the cost of a single-phase DNS is exclusively established by the smallest scales of turbulence

Die approbierte gedruckte Originalversion dieser Dissertation ist an der TU Wien Bibliothek verfügbar.
The approved original version of this doctoral thesis is available in print at TU Wien Bibliothek.
TU Bibliothek Your knowledge hub WIEN

(Kolmogorov scale), in the multiphase case the additional cost of the interface description must be considered. It is then essential to mention that when the mixing of an active/passive scalar is taken into account, the cost of a DNS depends also on another scale: the Batchelor scale. This scale represents the smallest scale of the scalar field and becomes smaller than the Kolmogorov scale whenever Prandtl/Schmidt numbers larger than unity are considered, thus implying in the latter cases the necessity of a finer grid. In this thesis, interface-resolved DNS will be used for the investigation of drop/bubble-laden turbulent flows, employing a Phase Field method for the description of the interface.

Thesis outline

This thesis is organised as follows:

- **Chap. 2: Methodology.**

  The governing equations for the resolution of the flow field are introduced, in the context of the one-fluid formulation. Then, following a brief overview of the methods for the interface modelling, the Phase Field method is illustrated. After the energy equation for the description of the temperature field is presented, a dimensional analysis of all the equations is performed. Finally, the space and time discretization of the equations, the numerical method and its implementation are reported.

- **Chap. 3: Density, viscosity and surface tension effects on drops and bubbles in turbulence.**

  The dynamics of a swarm of large and deformable drops or bubbles in a turbulent channel flow is investigated, focusing on the role of density and viscosity differences, as well as surface tension. The impact of these factors is observed in terms of topological (breakage/coalescence) and morphological modifications of the dispersed phase. The effects induced by the drops/bubbles properties on the turbulent flow are also evaluated in terms of turbulent kinetic energy.

- **Chap. 4: Heat transfer in drop-laden turbulence.**

  The heat transfer by large and deformable drops in a turbulent channel flow is studied, with a particular attention on the role played by thermal diffusivity. Specifically, the heat transfer by warm drops to a cold carrier fluid is analysed, computing the evolution in time of the average temperature of each phase and developing a simplified phenomenological model of the process. A self-similarity is found in the time behaviour of the average temperature and of the heat transfer coefficient and universal scalings are introduced.

Die approbierte gedruckte Originalversion dieser Dissertation ist an der TU Wien Bibliothek verfügbar.
The approved original version of this doctoral thesis is available in print at TU Wien Bibliothek.
TU Bibliothek Your knowledge hub WIEN

- **Chap. 5: Viscosity influence on heat transfer in drop-laden turbulence.**

  The influence of viscosity on the heat transfer by large and deformable drops in a turbulent channel flow is investigated. Two viscosity ratios are chosen in order to mimic the cases of water drops in oil and oil drops in water. The temperature and velocity fields are discussed qualitatively, and the time evolution of the heat transfer between the phases is compared in the two cases.

Die approbierte gedruckte Originalversion dieser Dissertation ist an der TU Wien Bibliothek verfügbar.
The approved original version of this doctoral thesis is available in print at TU Wien Bibliothek.
TU Bibliothek Your knowledge hub WIEN

Die approbierte gedruckte Originalversion dieser Dissertation ist an der TU Wien Bibliothek verfügbar.
The approved original version of this doctoral thesis is available in print at TU Wien Bibliothek.

Die approbierte gedruckte Originalversion dieser Dissertation ist an der TU Wien Bibliothek verfügbar.
The approved original version of this doctoral thesis is available in print at TU Wien Bibliothek.

2 Methodology

This chapter presents the mathematical description and the numerical approach used for the simulation of turbulent dispersed multiphase flows. The first section, 2.1, illustrates the flow field description, with the treatment of surface tension forces and non-matched thermophysical properties. The second section, 2.2, briefly reviews some of the most common methods for the interface modelling, analysing in details the Phase Field Method, while the third section, 2.3, presents the energy equation governing the heat transfer phenomenon. Once all the equations have been defined, the dimensionless equations are derived in section 2.4, and their numerical discretization and solution algorithms are illustrated in section 2.5. Finally, some details on the code implementation and validation are given in section 2.6.

2.1 Flow field

Multiphase flows are characterized by the presence of multiple fluids with different properties, separated by a moving and deforming boundary, the interface. The description of the flow field, therefore, must take into account for two additional aspects with respect to single-phase flows: the necessity to track the boundaries separating the phases, where surface tension forces are applied, and the possibility to handle abrupt changes of density and viscosity [128]. Many methods have been developed for direct numerical simulations of such flows. Among them we can distinguish three categories: the one-fluid approach, the body-fitted grid methods and the sharp-interface methods. The one-fluid approach consists in solving one single set of equations for all phases, usually on a structured grid. The boundary conditions are thus imposed at the boundaries of the entire domain, and no jump conditions are used at the interface. On the other hand, a term must be introduced in the Navier-Stokes equations to include the effect of the surface tension forces, and discontinuities of the properties (like density and viscosity) must be also properly included. The use of a one-fluid formulation therefore imply the presence of discontinuities in the flow field, which for numerical reasons must be smoothed on a thin layer. In the body-fitted grid methods, instead, multiple sets of equations are solved, one for each phase, and appropriate jump conditions are imposed at the interface, coupling the different sets of equations. These methods can well represent jumps of properties and surface tension forces (since the interface constitutes the boundary of the phases domains), but they must exploit

unstructured grids that conform to the interface shape. Consequently, they improve the description of complex interfacial phenomena but require higher computational sources. The third category of methods, sharp-interface methods, has then emerged in an attempt to combine the computational advantages of the one-fluid approach with the accuracy of the body-fitted grid methods. Indeed, these methods rely on the solution of multiple sets of equations in separated domains, allowing the explicit imposition of jump conditions at the interface, as well as the resolution of the equations on a structured grid. This category appears promising for its ability to handling discontinuities at the interface, while using still uniform structured grids that benefit from a high computational efficiency. On the other hand, some issues limit their application [44], and their computational cost can be much higher with respect to the one-fluid approach. The one-fluid formulation, despite being the oldest among all numerical formulations for multiphase flows, remains the most widely used for its simplicity and enormous power at the same time [128]. In the following, the one-fluid approach, that has been chosen for the present work, will be explained in more detail.

2.1.1 One-fluid formulation

In the one-fluid formulation the conservation of mass, momentum and energy are written for the whole flow field, regardless of the number of phases present in the problem. Here we restrict to the case of a two-phase incompressible flow. For incompressible two-phase flows the mass conservation equation (or continuity equation) is the same as in single-phase flows [64, 128],

$$\nabla \cdot \mathbf{u} = 0\,, \tag{2.1}$$

being $\mathbf{u} = (u, v, w)$ the velocity field. This equation indicates that the velocity is divergence-free and is valid also when the phases have different densities.[1]
The momentum conservation is expressed by the Navier-Stokes equations, which are modified with respect to the single-phase case, in order to take into account for the surface tension forces and for the discontinuities of density and viscosity. In the most general case for a two-phase incompressible flow they can be written as

$$\rho(\phi)\left(\frac{\partial \mathbf{u}}{\partial t} + \mathbf{u}\cdot\nabla\mathbf{u}\right) = -\nabla p + \nabla\cdot[\mu(\phi)(\nabla\mathbf{u} + \nabla\mathbf{u}^T)] + \mathbf{F}_\sigma\,, \tag{2.2}$$

where p is the pressure, ϕ the phase field variable, $\rho(\phi)$ and $\mu(\phi)$ the local density and dynamic viscosity, respectively, and $\mathbf{F}_\sigma$ the surface tension forces. The term $\mathbf{F}_\sigma$ introduces the surface tension forces at the boundaries between the phases, and is in general expressed by means of δ functions. The phase field variable ϕ is the marker function that identifies the location of the different phases. This marker function is advected by the flow and its behaviour can be modelled with several different methods. Among these, some of the most common methods will be examined in section 2.5, including the Phase Field method that will be used in this work. The density and viscosity discontinuities, which are located at the interface between the phases, can be

[1] Equation 2.1, however, does not hold when phase changes occur in the system [17].

Die approbierte gedruckte Originalversion dieser Dissertation ist an der TU Wien Bibliothek verfügbar.
The approved original version of this doctoral thesis is available in print at TU Wien Bibliothek.
TU Bibliothek Your knowledge hub WIEN

therefore introduced considering a dependency on the local value of the marker function. The term $\mathbf{F}_\sigma$, here left implicit, as well as the relations between density/viscosity and the phase field, $\rho(\phi)$ and $\mu(\phi)$, will be treated in the following paragraphs. For the energy conservation, the passive scalar approximation will be adopted, meaning that the heat transfer does not have any feedback on the mass and momentum conservation equations. Within this framework, the energy equation is decoupled from the continuity and Navier-Stokes equations, therefore it will be analysed separately in section 2.3.

Treatment of surface tension forces

Liquid-gas or liquid-liquid interfaces are characterized by an abrupt change of molecular composition. Since fluid molecules near or at the interface experience uneven molecular forces of attraction, interfaces are in a state of tension. The microscopic forces applied at the interface are called surface tension forces (or interfacial tension forces). They act in the normal and tangential directions and, following [20, 78, 126], can be expressed as

$$\mathbf{F}_\sigma = \underbrace{-\mathcal{K}\sigma(\mathbf{x}_s)\delta(\mathbf{x}_s)\mathbf{n}}_{\mathbf{f}_n} + \underbrace{\nabla_s\sigma(\mathbf{x}_s)\delta(\mathbf{x}_s)}_{\mathbf{f}_t}, \tag{2.3}$$

with $\mathcal{K}$ the interface mean curvature, σ the surface tension, $\mathbf{n}$ the interface normal versor, $\mathbf{x}_s$ the interface position and δ a surface Dirac δ-function. The normal component $\mathbf{f_n}$, that is proportional to the curvature and to the surface tension, is always present, while the tangential component $\mathbf{f_t}$ is present whenever the value of surface tension varies along the interface, creating surface tension gradients. Such gradients can be induced by temperature variations or by the presence of a surfactant in the mixture. The δ-function is non-zero only at the interface and allows the imposition of the forces exclusively along the interface. When the equations are discretized, this function must be approximated along with the rest of the equations; this can be done with different methods [126]. Using the Phase Field method, the following relations can be obtained [150],

$$\delta = \frac{3|\nabla\phi|^2\xi}{\sqrt{8}(\beta/\alpha)} \qquad \mathbf{n} = \frac{\nabla\phi}{|\nabla\phi|} \qquad \mathcal{K} = \nabla\cdot\mathbf{n}\,, \tag{2.4}$$

where $\xi = \sqrt{\kappa/\beta}$ is a measure of the interfacial layer thickness, and β and α are two positive constants of the model [25, 77]. The expression of $\mathcal{K}$ can be rewritten as

$$\mathcal{K} = \nabla\cdot\frac{\nabla\phi}{|\nabla\phi|} = \frac{\nabla^2\phi}{|\nabla\phi|} - \frac{1}{|\nabla\phi|^2}\nabla\phi\cdot\nabla(|\nabla\phi|)\,, \tag{2.5}$$

using the properties of the divergence operator. The surface tension can depend on the presence of surfactants or temperature gradients. In these cases, an equation of state (EOS) can be used to express the surface tension dependency on the surfactant concentration ψ,

$$\sigma(\psi) = \sigma_0(1 + \beta_s\ln(1-\psi))\,, \tag{2.6}$$

Die approbierte gedruckte Originalversion dieser Dissertation ist an der TU Wien Bibliothek verfügbar.
The approved original version of this doctoral thesis is available in print at TU Wien Bibliothek.

or on the temperature θ,

$$\sigma(\theta) = \sigma_0 - \beta_\theta(\theta - \theta_0)\,. \tag{2.7}$$

Equation 2.6 is the Langmuir EOS [1, 93], where σ_0 is the surface tension for the clean interface and β_s is the elasticity number, which represents the strength of the surfactant. Eq. 2.7 assumes a linear dependence of σ on θ, with θ_0 the reference temperature and β_θ the surface tension coefficient, defined as $\beta_\theta = -\partial\sigma/\partial\theta|_{\theta=\theta_0}$. Restricting to the case of a clean surface (without surfactants) and of small temperature differences, the expression of σ can be simplified as $\sigma = \sigma_0$. Combining Eq. 2.3 with Eq. 2.4 and Eq. 2.5, we obtain

$$\mathbf{f}_n = -\frac{3\sigma_0\xi}{\sqrt{8}(\beta/\alpha)}\nabla^2\phi\nabla\phi\,. \tag{2.8}$$

Alternatively, considering the procedure proposed by [86], the following formulation can be obtained:

$$\mathbf{f}_n = \frac{3\sigma_0\xi}{\sqrt{8}(\beta/\alpha)}\nabla\cdot\tau_c\,, \tag{2.9}$$

where $\tau_\mathbf{c}$ is the Korteweg tensor and is defined as

$$\tau_c = (|\nabla\phi|^2\mathbf{I} - \nabla\phi\otimes\nabla\phi)\,. \tag{2.10}$$

The two formulations of Eq. 2.8 and Eq. 2.9 are equivalent; in this work the latter formulation will be adopted.
If σ is constant ($\sigma = \sigma_0$), as previously assumed, there are no surface tension gradients and $\nabla_s\sigma = 0$. Hence, the tangential component $\mathbf{f}_t$ becomes null and $\mathbf{F}_\sigma$ reduces to

$$\mathbf{F}_\sigma = \mathbf{f}_n = \frac{3\sigma_0\xi}{\sqrt{8}(\beta/\alpha)}\nabla\cdot\tau_c\,. \tag{2.11}$$

Treatment of non-matched properties

In two-phase flows, thermophysical properties that are dependent on the phases, like density and viscosity, can be defined as proportional to the marker function. Specifically, in the Phase Field method they are proportional to the phase field variable ϕ. Following the profile of ϕ (shown and discussed in section 2.2.2), they undergo a smooth transition across the interface. This strategy allow to avoid sharp jumps in the flow field that introduce complications from a numerical viewpoint. Here, the treatment of density and viscosity differences is examined, even if this treatment could be employed also for other properties, as for example the thermal diffusivity α. The density and viscosity ratios between the two phases are respectively defined as

$$\rho_r = \frac{\rho_d}{\rho_c}\,, \qquad \mu_r = \frac{\mu_d}{\mu_c} \tag{2.12}$$

with the subscripts d associated to the dispersed phase properties and c to the carrier phase properties. In Fig. 2.1 the profile of a generic thermo-physical property is

Die approbierte gedruckte Originalversion dieser Dissertation ist an der TU Wien Bibliothek verfügbar.
The approved original version of this doctoral thesis is available in print at TU Wien Bibliothek.
TU Bibliothek Your knowledge hub WIEN

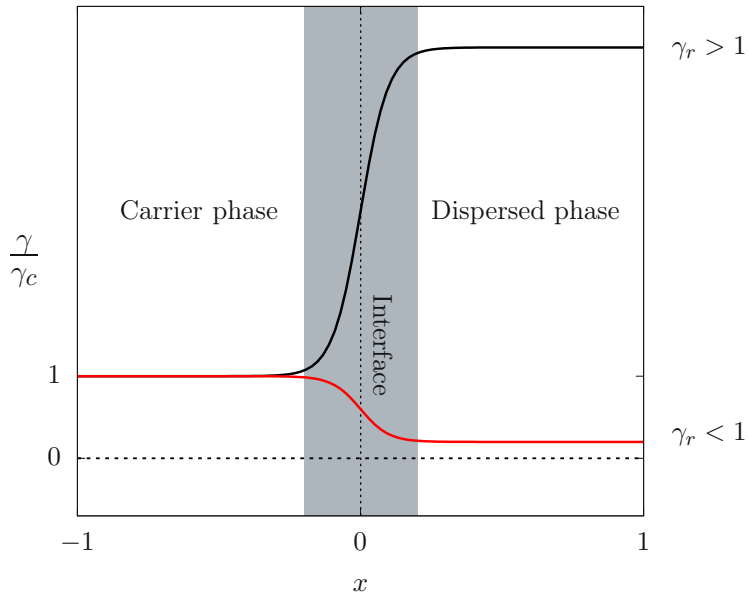

FIGURE 2.1 – Profile of a generic thermo-physical property γ across the interface (vertical dashed line) for two different property ratios γ_r. The interfacial layer (gray area) identifies the region in which the phase field spans ±96% of its bulk value.

shown. The variable γ can represent density or viscosity. The interface is also reported, identified by a dashed black vertical line, while the interfacial layer (±96% of the phase field bulk value) is shown with a gray rectangle. The black solid line and the red solid line show the behaviour of the generic property when the property ratio is greater than one, $\gamma_r > 1$, and less than one, $\gamma_r < 1$, respectively. Since the property of the carrier phase is taken as a reference, the dimensionless thermo-physical property is exactly equal to 1 in the bulk of the carrier phase, while it is equal to the property ratio, γ_r, in the bulk of the dispersed phase.

Thermo-physical are expressed as follows

$$\rho(\phi) = \rho_c \left[1 + \frac{\rho_r - 1}{2} \left(\frac{\phi}{\sqrt{\beta/\alpha}} + 1 \right) \right], \tag{2.13}$$

$$\mu(\phi) = \mu_c \left[1 + \frac{\mu_r - 1}{2} \left(\frac{\phi}{\sqrt{\beta/\alpha}} + 1 \right) \right], \tag{2.14}$$

Since they are defined as a function of the phase field variable, their value never reduces below zero (value which would be unphysical for both density and viscosity) if the phase-field does not overshoot/undershoot the equilibrium profile.

Die approbierte gedruckte Originalversion dieser Dissertation ist an der TU Wien Bibliothek verfügbar.
The approved original version of this doctoral thesis is available in print at TU Wien Bibliothek.
TU Bibliothek Your knowledge hub WIEN

2.2 Interface modelling

In the context of the one-fluid approach, where the governing equations are solved on a fixed grid, the different fluids and the interface must be identified and tracked in space and time [128]. The numerical methods used for this purposes can be divided in two categories: interface tracking methods and interface capturing methods. In interface tracking methods, a set of marker points are used to explicitly track the location of the interface, while in interface capturing methods the interface is defined with a prescribed value of a marker function or phase-concentration field. Each method exploits a specific equation to evolve in time and space the marker points or the marker function. In the following, some of these methods will be examined. A more comprehensive description will be given then for the Phase Field method, that has been chosen for the present work.

2.2.1 Interface tracking

Front tracking

The most popular method among interface tracking methods is the Front Tracking (FT) method, developed by Unverdi and Tryggvason [155] and adopted in several later works [21, 153]. This method defines the interface by a set of Lagrangian marker points which are advected by the flow field according to

$$\frac{\partial \mathbf{x}^i}{\partial t} = \mathbf{u}^i \,, \tag{2.15}$$

with $\mathbf{x}^i$ the position of the i-th marker point, and $\mathbf{u}^i$ the local flow velocity, which needs to be interpolated from the Eulerian grid of the flow field to the marker point position. The interface can be then reconstructed by connecting the marker points. When the interface shrinks or expands, the set of points can be also updated run-time by adding or removing points, in order to achieve an adequate resolution of the interface and to avoid interface wiggles much smaller than the grid size. When the phase is dispersed, the interface is separated in different closed tracts (i.e. one for each drop), which must be described by multiple sets of connected marker points. The different sets of points can approach each other and interact, causing breakage or coalescence phenomena. These topological modifications of the interface, unlike the morphological modifications, are not handled automatically by the method and must be described by including additional ad hoc models [100, 101, 153]. After the interface has been reconstructed, the interface curvature can be calculated and, consequently, surface tension forces can be obtained. These are computed at the marker point positions and therefore have to be redistributed on the Eulerian grid of the flow field by means of a smoothing operation. This method therefore requires continuous interpolation from the Eulerian grid to the Lagrangian grid to get the advection velocity, and from the Lagrangian grid to the Eulerian grid to obtain the distributed surface tension forces.

Die approbierte gedruckte Originalversion dieser Dissertation ist an der TU Wien Bibliothek verfügbar.
The approved original version of this doctoral thesis is available in print at TU Wien Bibliothek.
TU Bibliothek Your knowledge hub WIEN

2.2.2 Interface capturing

Volume of fluid

The Volume of Fluid (VoF) method belongs to the category of interface capturing methods and was first developed by Hirt and Nichols in 1979 [74] as a flexible and efficient method to simulate problems with complex free boundaries. The phases are identified by an Eulerian marker function f, which is defined in the entire domain and evolves according to the advection equation

$$\frac{\partial f}{\partial t} + \mathbf{u} \cdot \nabla f = 0\,, \tag{2.16}$$

where $\mathbf{u}$ is the velocity field. In particular, f represents the concentration of one of the phases and is

$$f = \begin{cases} f = 0 & \text{Phase 1} \\ f = 1 & \text{Phase 2}\,. \end{cases} \tag{2.17}$$

Since the domain is discretized, the cell value of the local concentration, f_{mix}, is defined as the average of the concentration over the volume of the computational cell:

$$f_{mix} = \frac{1}{V_i} \int_V f(x, y, z) dV\,. \tag{2.18}$$

The marker function is initialized as a Heaviside function, which, being a step function, requires specific advection algorithms in order to avoid numerical diffusion over time [128]. These algorithms exploit the value of f_{mix} in the neighbouring computational cells to properly reconstruct the shape of the interface front. Based of the methods used for the interface reconstruction, the VoF methods can be further divided in geometric VoF and algebraic VoF methods. As all the other interface capturing methods, topological changes like breakages and coalescences are automatically handled by this method. It must be mentioned, however, that the reconstruction of the interface is not based on physical arguments and is thus not exact. Consequently, breakages and coalescences may not be properly resolved. An important advantage of the Volume of Fluid method is the exact conservation of the mass of each phase.

Level set

Another method among interface capturing methods is the Level Set (LS) method [60], that has been developed as an alternative to the SLIC-based (simple line interface calculation) VoF methods. This method identifies the phases with a smooth marker function ϕ, where the interface is at the zero-level of the marker function. The smoothness of the marker function allows for a highly accurate calculation of the interface normals and curvature, and consequently for an accurate computation of surface tension forces. The advection equation that describes the evolution of the marker function is

$$\frac{\partial \phi}{\partial t} + \mathbf{u} \cdot \nabla \phi = 0\,, \tag{2.19}$$

Die approbierte gedruckte Originalversion dieser Dissertation ist an der TU Wien Bibliothek verfügbar.
The approved original version of this doctoral thesis is available in print at TU Wien Bibliothek.
TU Bibliothek Your knowledge hub WIEN

with $\mathbf{u}$ the velocity field. In the classic level-set approach the function ϕ is defined as the signed-distance from the interface. Because of numerical diffusion, the marker function may lose its signed-distance property. Therefore, reinitialization operations of ϕ and specific advection schemes are used to maintain this property. The reinitialization of ϕ usually causes mass leakages among the two phases. This issue can be mitigated by refining the grid, even though mass conservation cannot be granted in general with this formulation. In order to improve the mass conservation, other formulations of this method have been introduced, such as the conservative level-set (CSL) or the coupled level-set and volume of fluid (CLS-VoF). More specifically, the CSL approach adopts a hyperbolic tangent function instead of the signed-distance function, and imposes the mass conservation of each phase in the reinitialization process; the CLS-VoF approach combines the accuracy of the normals and curvature computation offered by the level-set, with the mass conservation property of the volume of fluid. All level-set approaches, similarly to all interface-capturing methods, are characterized by the implicit description of breakage and coalescence phenomena, although they are only based on the local grid resolution, without physical considerations.

Phase field method

Classic formulation The Phase Field method was initially developed by Cahn and Hilliard for the description of critical and near critical mixtures [25, 26, 27] and applied in particular to phase separation by spinodal decomposition [23, 24]. The method was later extended to incompressible multiphase flows far from critical conditions [77], by introducing an advection term in the Cahn-Hilliard equation and coupling the interface description with the Navier-Stokes equations. In the Phase Field method, that belongs to the interface capturing methods, the marker function identifying the phases is the phase field, ϕ. The phase field corresponds to the relative concentration of the phases, it has a constant value in the bulk of each phase and follows a smooth variation across the interface. The evolution of the phase field variable is regulated by an advection-diffusion equation,

$$\frac{\partial \phi}{\partial t} + \mathbf{u} \cdot \nabla \phi = -\nabla \cdot \mathbf{J} \,, \tag{2.20}$$

which is the Cahn-Hilliard equation modified including an advection term, being $\mathbf{u}$ the velocity field. The term on the right-hand side of Eq. 2.20 is a diffusive term, where $\mathbf{J} = -\mathcal{M}_\phi \nabla \mu_\phi$ is a phase field flux, responsible for driving the system towards its equilibrium following the chemical potential μ_ϕ. The coefficient $\mathcal{M}_\phi$ is the mobility or Onsager coefficient, that controls the interface relaxation time and is set constant in our case [156]. Inserting the phase field flux definition in Eq. 2.20 we obtain

$$\frac{\partial \phi}{\partial t} + \mathbf{u} \cdot \nabla \phi = \nabla \cdot (\mathcal{M}_\phi \nabla \mu_\phi) \,. \tag{2.21}$$

The chemical potential μ_ϕ is defined as the variational derivative of a Ginzburg-Landau free energy functional $\mathcal{F}[\phi, \nabla\phi]$ [156, 77]:

$$\mu_\phi = \frac{\delta \mathcal{F}[\phi, \nabla \phi]}{\delta \phi} \,. \tag{2.22}$$

Die approbierte gedruckte Originalversion dieser Dissertation ist an der TU Wien Bibliothek verfügbar.
The approved original version of this doctoral thesis is available in print at TU Wien Bibliothek.
TU Bibliothek Your knowledge hub WIEN

In the case of a system with two immiscible fluids, the free energy functional is composed by two contributions. The first one, f_0, accounts for the bulk free energy of the system, that represents the tendency of the system to separate in two pure stable phases. The second one, f_{mix}, accounts for the mixing free energy, namely the energy stored in the interfacial layer, that, for liquid-liquid or gas-liquid systems, corresponds to the surface tension. The functional can be thus expressed as

$$\mathcal{F}[\phi, \nabla\phi] = \int_\Omega (f_0(\phi) + f_{mix}(\nabla\phi)) d\Omega \,, \tag{2.23}$$

being Ω the considered domain. In particular, f_0 is a double well potential and is defined as

$$f_0(\phi) = \frac{\alpha}{4}\left(\phi - \sqrt{\frac{\beta}{\alpha}}\right)^2 \left(\phi + \sqrt{\frac{\beta}{\alpha}}\right)^2 \tag{2.24}$$

where α and β are two positive constants that define the bulk properties of the two fluids. Its behaviour is reported in Fig. 2.2*a*: the two minima correspond to the pure phases, $\phi = \pm\sqrt{\beta/\alpha}$. The mixing term f_{mix} is proportional to the gradient of the phase field,

$$f_{mix}(\nabla\phi) = \frac{\kappa}{2}|\nabla\phi|^2 \tag{2.25}$$

with κ a positive constant representing the magnitude of the surface tension. As shown in Fig. 2.2*b*, f_{mix} has a maximum at the interface and is zero in the bulk of the two phases. By taking the variational derivative of the free energy functional, the chemical potential is obtained:

$$\mu_\phi = \frac{\delta\mathcal{F}\,[\phi, \nabla\phi]}{\delta\phi} = \alpha\phi^3 - \beta\phi - \kappa\nabla^2\phi \,. \tag{2.26}$$

At the equilibrium the chemical potential is constant in the entire domain. Therefore, the equilibrium profile of the phase field can be derived by imposing $\nabla\mu_\phi = 0$. For a flat interface, the phase field equilibrium profile results in

$$\phi = \sqrt{\frac{\beta}{\alpha}} \tanh\left(\frac{x}{\sqrt{2}\xi}\right), \tag{2.27}$$

where $\xi = \sqrt{\kappa/\beta}$ is a measure of the interfacial layer thickness and s is a coordinate normal to the interface. The behaviour of the equilibrium profile is illustrated in Fig. 2.2*b* (dashed line): it can be noticed that the phase field is constant in the bulk of the phases ($s \to \pm\infty$) and, following the hyperbolic tangent profile, has a smooth transition across the interface, whose thickness is proportional to the parameter ξ. The surface tension can be also related to the functional $\mathcal{F}$ by means of the expression

$$\sigma = \frac{\beta\kappa}{\alpha} \int_{-\infty}^{+\infty} \mathcal{F}[\phi, \nabla\phi] dx \,, \tag{2.28}$$

Die approbierte gedruckte Originalversion dieser Dissertation ist an der TU Wien Bibliothek verfügbar.
The approved original version of this doctoral thesis is available in print at TU Wien Bibliothek.
TU Bibliothek Your knowledge hub WIEN

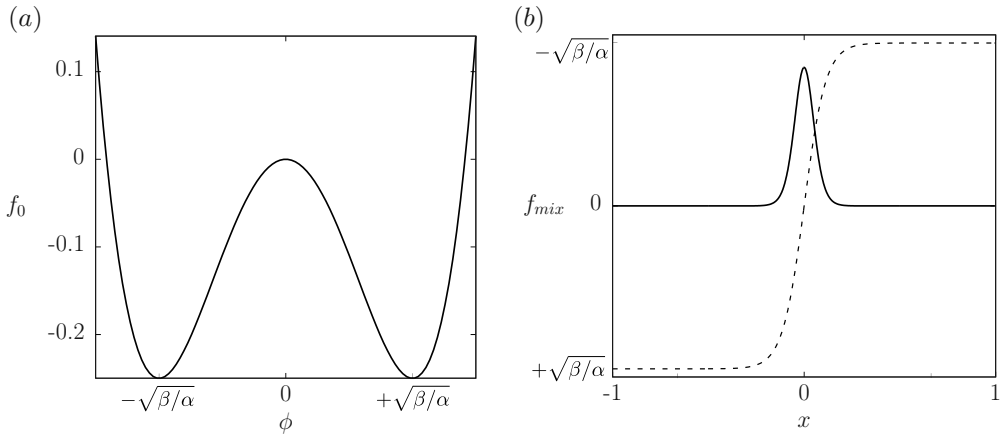

FIGURE 2.2 – Double well potential f_0 (panel a) and mixing free energy f_{mix} (panel b). The interface (iso-contour $\phi = 0$) is marked with a dashed line.

which is enforcing that the integral of the system free energy density across the interface must be equal to the surface tension. Using the equilibrium profile in the integration, the following relation is obtained:

$$\sigma = \frac{2\sqrt{2}}{3}\frac{\beta\kappa}{\alpha\xi} = \frac{2\sqrt{2}}{3}\frac{\sqrt{\beta^3\kappa}}{\alpha}\,. \tag{2.29}$$

The phase field method is an exact approach for critical and near-critical mixtures, where the interface is actually a layer of finite thickness. For multi-fluid systems far-from-critical conditions, the thickness of the interface becomes extremely small (few molecular size, for temperature sufficiently below the critical one [103, 102]), therefore the thickness of the transition layer is usually much bigger than the real one, considering that the grid resolution cannot reach the order of the molecular size. For this kind of systems, the method thus constitutes an approximation, which gradually reduces as the grid is refined.

The advantages of the phase field method are the capability to automatically handle topological changes of the interface (breakups and coalescences) and to provide an accurate description of the interface as well as a precise calculation of the interfacial curvature. Indeed, there is no need for reinitialization operations, and specific advection schemes are not necessary to maintain the marker function profile. The disadvantages of the phase field method are shrinkage, coarsening and misrepresentation of surface tension forces and thermo-physical properties. Shrinkage phenomena occur when the phase field is perturbed from its equilibrium profile: this induces the tendency to restore the correct profile and causes mass leakages between the phases. As a consequence, the total mass of the system is conserved, while the mass of each phase is not necessarily conserved. Coarsening phenomena, instead, are due to the energy minimization criterion, which is intrinsic to the method: larger domains enclosed by an interface tend to grow at the expense of smaller ones, in order to reduce the interfacial energy. Besides shrinkage, phase field deviations from the equilibrium

Die approbierte gedruckte Originalversion dieser Dissertation ist an der TU Wien Bibliothek verfügbar.
The approved original version of this doctoral thesis is available in print at TU Wien Bibliothek.
TU Bibliothek Your knowledge hub WIEN

profile can also cause inaccuracies in the calculation of surface tension forces and misrepresentation of thermo-physical properties, being these quantities a function of the phase field. Undershoots or overshoots of the equilibrium profile can cause unphysical values of surface forces, and unphysical/negative values of density and viscosity. These limitations have been treated in several studies by introducing modified formulations of the method [94, 147, 168], such as the profile-corrected phase field method and the flux-corrected phase field method. In this work the profile-corrected formulation will be used. A brief explanation of this formulation will be given in the following section.

Mass-conservation-improved Phase Field method The profile-corrected formulation of the phase field method differs from the classic formulation only by the introduction of a term in the Cahn-Hilliard equation, which is called penalty flux. The penalty flux is proportional to the magnitude of the perturbation of the equilibrium profile, and it ams at forcing the interfacial profile towards its correct behaviour. The modified Cahn-Hilliard equation is thus

$$\frac{\partial \phi}{\partial t} + \mathbf{u} \cdot \nabla \phi = \mathcal{M}_\phi \nabla^2 \mu_\phi + f_p \,, \tag{2.30}$$

with f_p the penalty flux, considering a constant mobility parameter $\mathcal{M}_\phi$ (which can be therefore taken out of the divergence operator). An explicit definition of the penalty flux will be given in dimensionless form in section 2.4, after the dimensional analysis will be performed.

2.3 Energy equation

Following the one fluid formulation, as introduced in section 2.1.1, the energy conservation equation of a two-fluid system can be written as a single equation for the entire domain, considering, if necessary, property variations between the fluids. For a two-fluid incompressible system the energy equation can be written as

$$\frac{\partial \theta}{\partial t} + \mathbf{u} \cdot \nabla \theta = \nabla \cdot [\alpha(\phi) \nabla \theta] \,, \tag{2.31}$$

where θ is the temperature and $\alpha(\phi)$ is the local thermal diffusivity, defined as

$$\alpha(\phi) = \frac{k(\phi)}{\rho(\phi) c_p(\phi)} \,, \tag{2.32}$$

being $k(\phi)$ and $c_p(\phi)$ the local thermal conductivity and local specific heat respectively. In this work we study the heat transfer considering small temperature differences associated to negligible density variations. As a consequence, buoyancy effects can be ignored and temperature becomes simply a scalar, which is transported and diffused in the system without having any influence on the flow field. Moreover we consider two fluids with the same thermal diffusivity, with $\alpha(\phi) = \alpha$. In this case, Eq 2.33 can be simplified as

$$\frac{\partial \theta}{\partial t} + \mathbf{u} \cdot \nabla \theta = \alpha \nabla^2 \theta \,. \tag{2.33}$$

Die approbierte gedruckte Originalversion dieser Dissertation ist an der TU Wien Bibliothek verfügbar.
The approved original version of this doctoral thesis is available in print at TU Wien Bibliothek.
TU Bibliothek Your knowledge hub WIEN

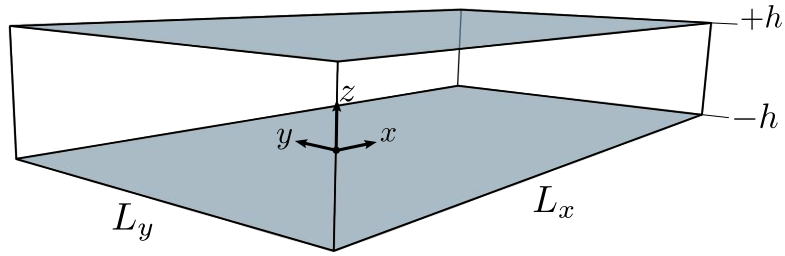

FIGURE 2.3 – Geometry of the simulation domain. The channel is bounded by solid walls at $z \pm h$ and has dimensions L_x in the streamwise direction, L_y in the spanwise direction and $2h$ in the wall-normal direction. The reference system is located at the channel midplane.

2.4 Dimensional analysis

The governing equations have been presented so far in dimensional form. In this section the corresponding dimensionless equations will be derived; all dimensionless variables will be indicated with the superscript $^-$. All simulations presented in this work are performed using the canonical geometrical configuration of the three-dimensional plane channel. A sketch of the channel with the used reference system is reported in Fig. 2.3. The two solid walls bounding the domain are located at $z = \pm h$, with h the channel half height. The channel half height h is chosen as a characteristic length scale of the problem, while the friction velocity u_τ is chosen as a characteristic velocity, since a pressure-driven flow, or Poiseuille flow, is considered (while the wall velocity u_w is usually adopted for a shear-driven flow, or Couette flow). The friction velocity is defined as $u_\tau = \sqrt{\tau_w/\rho_c}$, where τ_w is the shear stress at the wall and ρ_c is the reference density. The characteristic time scale can be derived from the length and velocity scale, thus we obtain

$$\mathbf{x}^- = \frac{\mathbf{x}}{h} \qquad \mathbf{u}^- = \frac{\mathbf{u}}{u_\tau} \qquad t^- = \frac{t u_\tau}{h}\,, \tag{2.34}$$

where $\mathbf{x} = (x, y, z)$ is the position vector, $\mathbf{u} = (u, v, w)$ is the velocity vector and t is the time. The phase field value in the bulk of the phases is used to get a dimensionless phase field,

$$\phi^- = \frac{\phi}{\sqrt{\beta/\alpha}}\,, \tag{2.35}$$

while using the carrier fluid density and the friction velocity we can get the dimensionless pressure

$$p^- = \frac{p}{\rho_c u_\tau^2}\,. \tag{2.36}$$

Die approbierte gedruckte Originalversion dieser Dissertation ist an der TU Wien Bibliothek verfügbar.
The approved original version of this doctoral thesis is available in print at TU Wien Bibliothek.
TU Bibliothek Your knowledge hub WIEN

The dimensionless temperature is then expressed as

$$\theta^- = \frac{\theta - \theta_r}{\Delta\theta} \tag{2.37}$$

where θ_r is the reference temperature, which is chosen as $\theta_r = \theta_{c,0}$, being $\theta_{c,0}$ the initial temperature of the carrier fluid.
The carrier fluid properties are taken as a reference to get dimensionless thermophysical properties. Dimensionless density, viscosity and thermal diffusivity can be thus written as

$$\rho^-(\phi^-) = \frac{\rho(\phi)}{\rho_c} = 1 + \frac{\rho_r - 1}{2}(\phi^- + 1)\,, \tag{2.38}$$

$$\mu^-(\phi^-) = \frac{\mu(\phi)}{\mu_c} = 1 + \frac{\mu_r - 1}{2}(\phi^- + 1)\,, \tag{2.39}$$

$$\alpha^-(\phi^-) = \frac{\alpha(\phi)}{\alpha_c} = 1 + \frac{\alpha_r - 1}{2}(\phi^- + 1)\,. \tag{2.40}$$

Recalling the expression of the surface forces term, Eq. 2.11, and the definition of the Korteweg tensor, Eq. 2.10, the dimensionless surface tension forces can be written, and multiplying by $h/(\rho_c u_\tau^2)$ the following term is obtained

$$\frac{h}{\rho_c u_\tau^2}\mathbf{F}_\sigma{}^- = \frac{h}{\rho_c u_\tau^2}\frac{3\sigma\xi}{\sqrt{8}(\beta/\alpha)}\frac{\beta/\alpha}{h^3}\nabla\cdot\tau_c^- = \frac{3}{\sqrt{8}}\frac{Ch}{We}\nabla\cdot\tau_c^-\,, \tag{2.41}$$

being $\tau_c = \frac{\beta/\alpha}{h^2}\tau_c^-$. The superscript has here been dropped from ∇^-, and will be dropped also in the following. Two dimensionless quantities have been introduced in Eq. 2.41: the Weber number, We, that is the ratio of inertial forces over surface tension forces, and the Cahn number, Ch, that is the dimensionless interface thickness. Their definition is thus

$$We = \frac{\rho_c u_\tau^2 h}{\sigma} \qquad Ch = \frac{\xi}{h}\,. \tag{2.42}$$

The continuity and Navier-Stokes equations in dimensionless form are therefore

$$\nabla\cdot\mathbf{u}^- = 0 \tag{2.43}$$

$$\begin{aligned}\rho^-(\phi^-)\left(\frac{\partial\mathbf{u}^-}{\partial t^-} + \mathbf{u}^-\cdot\nabla\mathbf{u}^-\right) = -\nabla p^- + \frac{1}{Re_\tau}\nabla\cdot[\mu^-(\phi^-)(\nabla\mathbf{u}^- + \nabla\mathbf{u}^{-T})] + \\ + \frac{3}{\sqrt{8}}\frac{Ch}{We}\nabla\cdot\tau_c^-\,.\end{aligned} \tag{2.44}$$

Another dimensionless quantity has been introduced in the dimensionless Navier-Stokes equations, namely the shear Reynolds number, which is defined as

$$Re_\tau = \frac{\rho_c u_\tau h}{\mu_c}\,. \tag{2.45}$$

Die approbierte gedruckte Originalversion dieser Dissertation ist an der TU Wien Bibliothek verfügbar.
The approved original version of this doctoral thesis is available in print at TU Wien Bibliothek.
TU Bibliothek Your knowledge hub WIEN

The energy equation in dimensionless form is

$$\frac{\partial \theta^-}{\partial t^-} + \mathbf{u}^- \cdot \nabla \theta^- = \frac{1}{PrRe_\tau} \nabla \cdot [\alpha^-(\phi^-) \nabla \theta^-] \,. \tag{2.46}$$

The dimensionless groups in Eq. 2.46 are the shear Reynolds number, previously defined, and the Prandtl number, Pr, which is the ratio of the momentum diffusivity (or kinematic viscosity) over the thermal diffusivity

$$Pr = \frac{\nu_c}{\alpha_c} \,. \tag{2.47}$$

Expressing the chemical potential in dimensionless form,

$$\mu_\phi = \sqrt{\frac{\beta^3}{\alpha}} \mu_\phi^- = \sqrt{\frac{\beta^3}{\alpha}} (\phi^{-3} - \phi^- - Ch^2 \nabla^2 \phi^-) \,, \tag{2.48}$$

and defining the dimensionless Péclet number for the phase field,

$$Pe_\phi = \frac{u_\tau h}{\mathcal{M}_\phi \beta} \,, \tag{2.49}$$

we obtain the modified Cahn-Hilliard equation (Eq. 2.20) in dimensionless form:

$$\frac{\partial \phi^-}{\partial t^-} + \mathbf{u}^- \cdot \nabla \phi^- = \frac{1}{Pe_\phi} \nabla^2 \mu_\phi^- + f_p^- \,. \tag{2.50}$$

The penalty flux is defined as

$$f_p^- = \frac{\lambda}{Pe_\phi} \left[\nabla^2 \phi - \frac{1}{\sqrt{2}Ch} \nabla \cdot \left((1 - \phi^2) \frac{\nabla \phi}{|\nabla \phi|} \right) \right] , \tag{2.51}$$

where λ is a positive constant parameter, that can be expressed as proposed by Li et al. [94] with the scaling $\lambda = \alpha / Ch$. The parameter α is here an arbitrary positive constant, related to the importance of the correction term. In the study of Soligo et al. [147], different values of the parameter α have been tested and an optimum value has been identified, in order to mitigate the shrinkage phenomena without affecting the topological changes of the interface.
The phase field equilibrium profile can also be expressed in dimensionless form

$$\phi^- = \tanh \left(\frac{s^-}{\sqrt{2}Ch} \right) \,, \tag{2.52}$$

where s^- is a dimensionless coordinate normal to the interface. The scaling system here used for the non-dimensionalization is the outer units system; the wall units (or inner units) system, used to treat turbulence statistics, is briefly illustrated in Appendix A. In the following sections and chapters the outer units notation will be dropped for ease of reading. All the dimensionless governing equations, and thermophysical properties expressions are reported again below (respectively continuity, Navier-Stokes, energy transport, phase field transport, density, viscosity and thermal diffusivity):

Die approbierte gedruckte Originalversion dieser Dissertation ist an der TU Wien Bibliothek verfügbar.
The approved original version of this doctoral thesis is available in print at TU Wien Bibliothek.
TU Bibliothek Your knowledge hub WIEN

$$\nabla \cdot \mathbf{u} = 0\,; \tag{2.53}$$

$$\rho(\phi)\left(\frac{\partial \mathbf{u}}{\partial t} + \mathbf{u}\cdot\nabla\mathbf{u}\right) = -\nabla p + \frac{1}{Re_\tau}\nabla\cdot[\mu(\phi)(\nabla\mathbf{u} + \nabla\mathbf{u}^T)] + \frac{3}{\sqrt{8}}\frac{Ch}{We}\nabla\cdot\tau_c\,; \tag{2.54}$$

$$\frac{\partial \theta}{\partial t} + \mathbf{u}\cdot\nabla\theta = \frac{1}{PrRe_\tau}\nabla\cdot[\alpha(\phi)\nabla\theta]\,; \tag{2.55}$$

$$\frac{\partial \phi}{\partial t} + \mathbf{u}\cdot\nabla\phi = \frac{1}{Pe_\phi}\nabla^2\mu_\phi + f_p\,; \tag{2.56}$$

$$\rho(\phi) = 1 + \frac{\rho_r - 1}{2}(\phi + 1)\,; \tag{2.57}$$

$$\mu(\phi) = 1 + \frac{\mu_r - 1}{2}(\phi + 1)\,; \tag{2.58}$$

$$\alpha(\phi) = 1 + \frac{\alpha_r - 1}{2}(\phi + 1)\,. \tag{2.59}$$

As concerns the choice of the dimensionless numbers, it must be pointed out that the shear Reynolds, the Weber and the Prandtl numbers are phenomenological parameters that define the physics of the specific problem analysed. The Cahn and Péclet numbers, instead, are numerical parameters that characterize the Phase Field method. In particular, the Cahn number, which is the dimensionless measure of the transition layer thickness, is set to the minimum possible value that satisfies the following requirement: there must be at least five grid points across the interface. As a consequence, the choice of this parameter depends on the available grid resolution. The Péclet number is set based on the Cahn number, according to the scaling $Pe_\phi = 1/Ch$ [103, 147, 167].

2.5 Numerical method

In this section, the numerical procedure for the solution of the dimensionless system of equations is illustrated. A velocity-vorticity formulation is adopted to solve the flow field. This formulation consists in replacing the Navier-Stokes equations by a system composed of a second-order equation for the wall-normal component of the vorticity, a fourth order equation for the wall normal component of the velocity and the definition of the wall-normal vorticity. This approach allows to avoid the time-consuming Poisson solver for the calculation of the pressure field, as the pressure term cancels out from the equations. The Cahn-Hilliard equation is solved in its original form, although a splitting operation is used for the Laplace operator, in order to improve the stability of the numerical scheme [156]. The system of governing equations is now rewritten with a more compact notation: all non-linear terms are collected in single terms, $\mathbf{S}$, S_ϕ and

Die approbierte gedruckte Originalversion dieser Dissertation ist an der TU Wien Bibliothek verfügbar.
The approved original version of this doctoral thesis is available in print at TU Wien Bibliothek.
TU Bibliothek Your knowledge hub WIEN

S_θ (for the Navier-Stokes, energy and phase field transport equations respectively), in order to separate them from the linear terms. Hence, the system becomes

$$\nabla \cdot \mathbf{u} = 0\,, \tag{2.60}$$

$$\frac{\partial \mathbf{u}}{\partial t} = \mathbf{S} - \nabla p' + \frac{1}{Re_\tau}\nabla^2 \mathbf{u}\,, \tag{2.61}$$

$$\frac{\partial \theta}{\partial t} = S_\theta + \frac{1}{PrRe_\tau}\nabla^2 \theta\,, \tag{2.62}$$

$$\frac{\partial \phi}{\partial t} = S_\phi + \frac{s}{Pe_\phi}\nabla^2 \phi - \frac{Ch^2}{Pe_\phi}\nabla^4 \phi\,. \tag{2.63}$$

The pressure term has been decomposed in a mean and a fluctuating component, $p = \overline{p} + p'$; the pressure gradient thus results in the sum of a constant mean pressure gradient, Π, and a fluctuating pressure gradient, $\nabla p'$ [144]. The splitting coefficient, which appears in the phase-field transport equation, is defined as

$$s = \sqrt{\frac{4Pe_\phi Ch^2}{\Delta t}}, \tag{2.64}$$

with Δt the integration step. The non-linear terms can be thus written as follows:

$$\begin{aligned}\mathbf{S} = \begin{bmatrix} S_x \\ S_y \\ S_z \end{bmatrix} = -\mathbf{u}\cdot\nabla\mathbf{u} - \frac{\rho_r - 1}{2}(\phi+1)\left(\frac{\partial \mathbf{u}}{\partial t} + \mathbf{u}\cdot\nabla\mathbf{u}\right) - \Pi + \\ + \frac{1}{Re_\tau}\nabla\cdot\left[\frac{\mu_r - 1}{2}(\phi+1)(\nabla\mathbf{u} + \nabla\mathbf{u}^T)\right] + \frac{3}{\sqrt{8}}\frac{Ch}{We}\nabla\cdot\tau_c\end{aligned} \tag{2.65}$$

$$S_\theta = -\mathbf{u}\cdot\nabla\theta + \frac{1}{PrRe_\tau}\nabla\cdot\left[\frac{\alpha_r - 1}{2}(\phi+1)\nabla\theta\right] \tag{2.66}$$

$$S_\phi = -\mathbf{u}\cdot\nabla\phi + \frac{1}{Pe_\phi}[\nabla^2\phi^3 - (1+s)\nabla^2\phi] + f_p \tag{2.67}$$

The velocity-vorticity formulation, used for the resolution of the Navier-Stokes equations, is now introduced. First, a transport equation for the vorticity $\boldsymbol{\omega}$ is obtained by taking the curl of the Navier-Stokes equations:

$$\frac{\partial \boldsymbol{\omega}}{\partial t} = \nabla \times \mathbf{S} + \frac{1}{Re_\tau}\nabla^2 \boldsymbol{\omega}\,. \tag{2.68}$$

Second, a fourth-order equation for the velocity is obtained by taking the curl of Eq. 2.68 (corresponding to taking twice the curl of the Navier-Stokes equations).

$$\frac{\partial(\nabla^2 \mathbf{u})}{\partial t} = \nabla^2 \mathbf{S} - \nabla(\nabla\cdot\mathbf{S}) + \frac{1}{Re_\tau}\nabla^4 \mathbf{u}\,. \tag{2.69}$$

Die approbierte gedruckte Originalversion dieser Dissertation ist an der TU Wien Bibliothek verfügbar.
The approved original version of this doctoral thesis is available in print at TU Wien Bibliothek.
TU Bibliothek Your knowledge hub WIEN

Both Eq. 2.68 and Eq. 2.69 are then projected on the wall-normal direction. The final system thus results as follows,

$$\begin{cases} \nabla \cdot \mathbf{u} = 0 \\ \boldsymbol{\omega} \cdot \mathbf{n}_z = (\nabla \times \mathbf{u}) \cdot \mathbf{n}_z \\ \dfrac{\partial(\nabla^2 \mathbf{u})}{\partial t} \cdot \mathbf{n}_z = \left[\nabla^2 \mathbf{S} - \nabla(\nabla \cdot \mathbf{S}) + \dfrac{1}{Re_\tau} \nabla^4 \mathbf{u} \cdot \mathbf{n}_z \right] \\ \dfrac{\partial \boldsymbol{\omega}}{\partial t} \cdot \mathbf{n}_z = \left(\nabla \times \mathbf{S} + \dfrac{1}{Re_\tau} \nabla^2 \boldsymbol{\omega} \right) \cdot \mathbf{n}_z \\ \dfrac{\partial \theta}{\partial t} = S_\theta + \dfrac{1}{PrRe_\tau} \nabla^2 \theta \\ \dfrac{\partial \phi}{\partial t} = S_\phi + \dfrac{s}{Pe_\phi} \nabla^2 \phi - \dfrac{Ch^2}{Pe_\phi} \nabla^4 \phi \end{cases} \tag{2.70}$$

where the definition of the wall-normal vorticity has been additionally included. The symbol $\mathbf{n}_z$ represents the wall-normal unit vector. The obtained system is solved for the velocity components u, v, w, the wall-normal component of the vorticity $\boldsymbol{\omega}_z$, the phase field ϕ and the temperature θ. Once the velocity field is obtained, the fluctuating pressure p' can be calculated by applying the divergence operator to the original Navier-Stokes equations, Eq. 2.61, which therefore reduces to a Poisson equation, as follows:

$$\nabla^2 p' = \nabla \cdot \mathbf{S} \,. \tag{2.71}$$

2.5.1 Time discretization

An IMplicit-EXplicit (IMEX) scheme is used for the time-advancement of the system of equations: the non-linear terms $\mathbf{S}$, S_θ and S_ϕ are integrated explicitly with a two-step Adams-Bashforth scheme, while all the other linear terms are integrated implicitly. A Crank-Nicolson scheme is used for the linear terms of the equations for the second-order wall-normal vorticity equation and for the fourth-order wall-normal velocity equation. An implicit Euler scheme is used instead for the linear terms of the energy equation and the Cahn-Hilliard equation: this scheme allows to better damp the high-frequency oscillations that may arise from the steep gradients associated to the phase-field [156, 119]. At the first time step all the non-linear terms are integrated with an explicit Euler scheme. The time-discretized system at a generic time step n (current

Die approbierte gedruckte Originalversion dieser Dissertation ist an der TU Wien Bibliothek verfügbar.
The approved original version of this doctoral thesis is available in print at TU Wien Bibliothek.
TU Bibliothek Your knowledge hub WIEN

time step) is:

$$\begin{cases} \nabla \cdot \mathbf{u}^{n+1} = 0 \\ \boldsymbol{\omega}^{n+1} \cdot \mathbf{n}_z = (\nabla \times \mathbf{u}^{n+1}) \cdot \mathbf{n}_z \\ \dfrac{\nabla^2 \mathbf{u}^{n+1} - \nabla^2 \mathbf{u}^n}{\Delta t} \cdot \mathbf{n}_z = \left[\dfrac{3[\nabla^2 \mathbf{S}^n - \nabla(\nabla \cdot \mathbf{S}^n)] - [\nabla^2 \mathbf{S}^{n-1} - \nabla(\nabla \cdot \mathbf{S}^{n-1}]}{2} + \right. \\ \qquad \left. + \dfrac{1}{Re_\tau} \dfrac{\nabla^4 \mathbf{u}^{n+1} + \nabla^4 \mathbf{u}^n}{2} \right] \cdot \mathbf{n}_z \\ \dfrac{\omega^{n+1} - \omega^n}{\Delta t} = \left(\dfrac{3\nabla \times \mathbf{S}^n - \nabla \times \mathbf{S}^{n-1}}{2} + \dfrac{1}{Re_\tau} \dfrac{\nabla^2 \omega^{n+1} + \nabla^2 \omega^n}{2} \right) \cdot \mathbf{n}_z \\ \dfrac{\theta^{n+1} - \theta^n}{\Delta t} = \dfrac{3S_\theta^n - S_\theta^{n-1}}{2} + \dfrac{1}{PrRe_\tau} \nabla^2 \theta^{n+1} \\ \dfrac{\phi^{n+1} - \phi^n}{\Delta t} = \dfrac{3S_\phi^n - S_\phi^{n-1}}{2} + \dfrac{2}{Pe_\phi} \nabla^2 \phi^{n+1} - \dfrac{Ch^2}{Pe_\phi} \nabla^4 \phi^{n+1} \end{cases} \tag{2.72}$$

2.5.2 Spatial discretization

This dimensionless system of equations is discretized in space using a pseudo-spectral approach [30, 75, 122] with Fourier series in the streamwise (x) and spanwise (y) directions and Chebyshev polynomials in the wall-normal (z) direction. The use of Fourier transforms in the homogeneous directions implicitly enforces periodic boundary conditions on all variables along these directions. All variables are solved on the same computational grid, apart from the temperature, which can be solved on a finer grid when Prandtl numbers larger than one are considered. This allows to properly resolve the temperature field down to the smallest scales, which are below the smallest turbulent scales whenever Prandtl is larger than one. The adoption of the finer grid exclusively for the temperature and the coarse grid for all the other variables limit the overall computational cost. In the streamwise and spanwise directions a uniform grid spacing is adopted, while in the wall-normal direction Chebyshev-Gauss-Lobatto points are chosen in order to have a finer grid close to the channel walls. The points (x_i, y_j, z_k) of the Cartesian grid are defined as

$$\begin{aligned} x_i &= (i-1)\frac{L_x}{N_x - 1} && i = 1, \ldots, N_x \\ y_i &= (j-1)\frac{L_y}{N_y - 1} && j = 1, \ldots, N_y \\ z_k &= \cos\left(\frac{k-1}{N_z - 1}\pi\right) && k = 1, \ldots, N_z \end{aligned} \tag{2.73}$$

where N_x, N_y and N_z are the number of grid points in x, y and z direction, respectively. All equations are solved in spectral space. All variables are brought from a physical to

Die approbierte gedruckte Originalversion dieser Dissertation ist an der TU Wien Bibliothek verfügbar.
The approved original version of this doctoral thesis is available in print at TU Wien Bibliothek.
TU Bibliothek Your knowledge hub WIEN

a spectral representation using Fourier and Chebyshev transforms. A generic variable $f(x,y,z,t)$ in physical space can be represented in spectral space as a truncated series of Fourier wavenumbers and Chebyshev polynomials, T_k,

$$f(x,y,z,t) = \sum_{i=0}^{N_x/2} \sum_{j=-N_y/2+1}^{N_y/2} \sum_{k=0}^{N_z-1} \hat{f}(k_{x,i},k_{y,j},k,t) T_k(z) e^{\iota(k_{x,i}x+k_{y,j}y)} \,, \tag{2.74}$$

where $\iota = \sqrt{-1}$ is the imaginary unit. The Fourier coefficient $\hat{f}$ depends on the wavenumbers, $k_{x,i}$ and $k_{y,j}$, on the k^{th} Chebyshev polynomial and on time. The Fourier wavenumbers $k_{x,i}$ and $k_{y,j}$ are defined as follows:

$$k_{x,i} = \frac{2\pi(i-1)}{L_x} \qquad i = 1,\ldots,N_x/2+1 \,, \tag{2.75}$$

$$k_{y,j} = \begin{cases} \dfrac{2\pi(j-1)}{L_y} & j = 1,\ldots,N_y/2+1 \\ -\dfrac{2\pi(N_y-j+1)}{L_y} & j = N_y/2+2,\ldots,N_y \end{cases} \,. \tag{2.76}$$

The spectral and pseudo-spectral methods are characterized by a high accuracy in the calculations of derivatives, as spatial derivatives in spectral space are exact. A truncation error is however introduced in the variables representation, when truncating the infinite Fourier and Chebyshev series to finite series, although this error is extremely small. The derivatives in the homogeneous directions can be computed from Eq. 2.74:

$$\frac{\partial f(x,y,z,t)}{\partial x} = \sum_{i=0}^{N_x/2} \sum_{j=-N_y/2+1}^{N_y/2} \sum_{k=0}^{N_z-1} \iota k_{x,i} \hat{f} T_k e^{\iota(k_{x,i}x+k_{y,j}y)} \,, \tag{2.77}$$

$$\frac{\partial f(x,y,z,t)}{\partial y} = \sum_{i=0}^{N_x/2} \sum_{j=-N_y/2+1}^{N_y/2} \sum_{k=0}^{N_z-1} \iota k_{y,j} \hat{f} T_k e^{\iota(k_{x,i}x+k_{y,j}y)} \,. \tag{2.78}$$

Once all the variables have been written in spectral space, the system of equations of Eq. 2.72 can be re-written in spectral space. Thanks to the orthogonality of all Fourier modes, the problem can be split in $(N_x/2+1)\times N_y$ independent subproblems, one for each wavenumber couple $(k_{x,i},\ k_{y,j})$. In the following, the symbol $\hat{f}$ will be used to indicate the Chebyshev discretization of Fourier modes at a generic couple of wavenumbers, in order to have a more compact notation. Specifically $\hat{f}$ will indicate the expression

$$\hat{f} = \hat{f}_{i,j} = \sum_{k=0}^{N_z-1} \hat{f}(k_{x,i},k_{y,j},k,t) T_k(z) e^{\iota(k_{x,i}x+k_{y,j}y)} \tag{2.79}$$

Die approbierte gedruckte Originalversion dieser Dissertation ist an der TU Wien Bibliothek verfügbar.
The approved original version of this doctoral thesis is available in print at TU Wien Bibliothek.
TU Bibliothek Your knowledge hub WIEN

for each couple $(i,j) \in ([1, N_x/2+1], [-N_y/2+1, N_y/2])$. The system of discretized equations thus becomes,

$$
\begin{cases}
\iota k_{x,i}\hat{u}^{n+1} + \iota k_{y,j}\hat{v}^{n+1} + \dfrac{\partial \hat{w}^{n+1}}{\partial z} = 0 \\
{\hat{\omega_z}}^{n+1} = \iota k_{x,i}\hat{v}^{n+1} - \iota k_{y,j}\hat{u}^{n+1} \\
\dfrac{1}{\Delta t}\left(\dfrac{\partial^2 \hat{w}^{n+1}}{\partial z^2} - k_{i,j}^2\hat{w}^{n+1} - \dfrac{\partial^2 \hat{w}^{n}}{\partial z^2} + k_{i,j}^2\hat{w}^{n}\right) = \\
\qquad = \dfrac{3}{2}\left(-k_{i,j}^2\hat{S}_z^n - \iota k_{x,i}\dfrac{\partial \hat{S}_x^n}{\partial z} - \iota k_{y,j}\dfrac{\partial \hat{S}_y^n}{\partial z}\right) - \\
\qquad -\dfrac{1}{2}\left(-k_{i,j}^2\hat{S}_z^{n-1} - \iota k_{x,i}\dfrac{\partial \hat{S}_x^{n-1}}{\partial z} - \iota k_{y,j}\dfrac{\partial \hat{S}_y^{n-1}}{\partial z}\right) + \\
\qquad \dfrac{1}{2Re_\tau}\left(k_{i,j}^4\hat{w}^{n+1} + \dfrac{\partial^4 \hat{w}^{n+1}}{\partial z^4} - 2k_{i,j}^2\dfrac{\partial^2 \hat{w}^{n+1}}{\partial z^2}\right) + \\
\qquad \dfrac{1}{2Re_\tau}\left(k_{i,j}^4\hat{w}^{n} + \dfrac{\partial^4 \hat{w}^{n}}{\partial z^4} - 2k_{i,j}^2\dfrac{\partial^2 \hat{w}^{n}}{\partial z^2}\right) \\
\dfrac{\hat{\omega}_z^{n+1} - \hat{\omega}_z^{n}}{\Delta t} = \dfrac{3}{2}\left(\iota k_{x,i}\hat{S}_y^n - \iota k_{y,j}\hat{S}_x^n\right) - \dfrac{1}{2}\left(\iota k_{x,i}\hat{S}_y^{n-1} - \iota k_{y,j}\hat{S}_x^{n-1}\right) + \\
\qquad + \dfrac{1}{2Re_\tau}\left(\dfrac{\partial^2 \hat{\omega}_z^{n+1}}{\partial z^2} - k_{i,j}^2\hat{\omega}_z^{n+1} - \dfrac{\partial^2 \hat{\omega}_z^{n}}{\partial z^2} + k_{i,j}^2\hat{\omega}_z^{n}\right) \\
\dfrac{\hat{\theta}^{n+1} - \hat{\theta}^{n}}{\Delta t} = \dfrac{3\hat{S}_\theta^n - \hat{S}_\theta^{n-1}}{2} + \dfrac{1}{PrRe_\tau}\left(\dfrac{\partial^2 \hat{\theta}^{n+1}}{\partial z^2} - k_{i,j}^2\hat{\theta}^{n+1}\right) \\
\dfrac{\hat{\phi}^{n+1} - \hat{\phi}^{n}}{\Delta t} = \dfrac{3\hat{S}_\phi^n - \hat{S}_\phi^{n-1}}{2} + \dfrac{s}{Pe_\phi}\left(\dfrac{\partial^2 \hat{\phi}^{n+1}}{\partial z^2} - k_{i,j}^2\hat{\phi}^{n+1}\right) - \\
\qquad - \dfrac{Ch^2}{Pe_\phi}\left(k_{i,j}^4\hat{\phi}^{n+1} + \dfrac{\partial^4 \hat{\phi}^{n+1}}{\partial z^4} - 2k_{i,j}^2\dfrac{\partial^2 \hat{\phi}^{n+1}}{\partial z^2}\right).
\end{cases}
\tag{2.80}
$$

being the coefficient $k_{i,j}^2$ the sum of the square of the corresponding wavenumbers: $k_{i,j}^2 = k_{x,i}^2 + k_{y,j}^2$. The terms which are previously known, namely the terms of time n (current time step) and $n-1$ (previous time step) are collected in a history term.

$$
H_x^n = \Delta t\left[\frac{3\hat{S}_x^n - \hat{S}_x^{n-1}}{2} + \frac{1}{2Re_\tau}\frac{\partial^2 \hat{u}^n}{\partial z^2} + \left(\frac{1}{\Delta t} - \frac{k_{i,j}^2}{2Re_\tau}\right)\hat{u}^n\right] \tag{2.81}
$$

$$
H_y^n = \Delta t\left[\frac{3\hat{S}_y^n - \hat{S}_y^{n-1}}{2} + \frac{1}{2Re_\tau}\frac{\partial^2 \hat{v}^n}{\partial z^2} + \left(\frac{1}{\Delta t} - \frac{k_{i,j}^2}{2Re_\tau}\right)\hat{v}^n\right] \tag{2.82}
$$

$$
H^n = \frac{\partial}{\partial z}(\iota k_{x,i}H_x^n + \iota k_{y,j}H_y^n) + k_{i,j}^2 H_z^n \tag{2.83}
$$

Die approbierte gedruckte Originalversion dieser Dissertation ist an der TU Wien Bibliothek verfügbar.
The approved original version of this doctoral thesis is available in print at TU Wien Bibliothek.
TU Bibliothek Your knowledge hub WIEN

$$H_\theta^n = \frac{\Delta t}{2}(3\hat{S}_\theta^n - \hat{S}_\theta^{n-1}) + \hat{\theta}^n \tag{2.84}$$

$$H_\phi^n = \frac{\Delta t}{2}(3\hat{S}_\phi^n - \hat{S}_\phi^{n-1}) + \hat{\phi}^n \tag{2.85}$$

Using the history terms and taking all the unknowns terms (of time $n+1$) to the left hand side, the following system is obtained for each couple (i,j):

$$\begin{cases} \iota k_{x,i}\hat{u}^{n+1} + \iota k_{y,j}\hat{v}^{n+1} + \dfrac{\partial \hat{w}^{n+1}}{\partial z} = 0 \\ \hat{\omega}_z^{n+1} = \iota k_{x,i}\hat{v}^{n+1} + \iota k_{y,j}\hat{u}^{n+1} \\ \left(\dfrac{\partial^2}{\partial z^2} - \beta^2\right)\left(\dfrac{\partial^2}{\partial z^2} - k_{i,j}^2\right)\hat{w}^{n+1} = \dfrac{H^n}{\gamma} \\ \left(\dfrac{\partial^2}{\partial z^2} - \beta^2\right)\hat{\omega}_z^{n+1} = -\dfrac{\iota k_{x,i}H_y^n - \iota k_{y,j}H_x^n}{\gamma} \\ \left(\dfrac{\partial^2}{\partial z^2} - \beta_\theta^2\right)\hat{\theta}^{n+1} = -\dfrac{H_\theta^n}{\gamma_\theta} \\ \left(\dfrac{\partial^2}{\partial z^2} - \beta_\phi^2\right)\left(\dfrac{\partial^2}{\partial z^2} - \beta_\phi^2\right)\hat{\phi}^{n+1} = \dfrac{H_\phi^n}{\gamma_\phi} \end{cases} \tag{2.86}$$

with the parameters γ, β, γ_θ, β_θ, γ_ϕ and β_ϕ defined as:

$$\begin{aligned} \gamma &= \frac{\Delta t}{2Re_\tau}, & \beta^2 &= \frac{1+\gamma k_{i,j}^2}{\gamma} \\ \gamma_\theta &= \frac{\Delta t}{2PrRe_\tau}, & \beta_\theta^2 &= \frac{1+\gamma_\theta k_{i,j}^2}{\gamma_\theta} \\ \gamma_\phi &= \frac{Ch^2\Delta t}{Pe_\phi}, & \beta_\phi^2 &= \frac{s}{2Ch^2} + k_{i,j}^2 . \end{aligned} \tag{2.87}$$

2.5.3 Boundary conditions

Since Fourier and Chebyshev transforms are employed, periodic boundary conditions are implicitly enforced in the streamwise (x) and spanwise (y) directions. A closed channel setup is considered, with solid walls at $z = \pm 1$ outer units (dimensionless units). Hence, no-slip and no-flux boundary conditions are imposed on the flow field:

$$\begin{cases} \mathbf{u}(x, y, z = \pm 1) = [u_w, v_w, 0] \\ \left.\dfrac{\partial w}{\partial z}\right|_{z=\pm 1} = 0 . \end{cases} \tag{2.88}$$

The fluid is constrained to move with the same velocity of the wall, where u_w and v_w are respectively the velocities in x and y directions of the moving wall (which are

Die approbierte gedruckte Originalversion dieser Dissertation ist an der TU Wien Bibliothek verfügbar.
The approved original version of this doctoral thesis is available in print at TU Wien Bibliothek.
TU Bibliothek Your knowledge hub WIEN

zero when a still wall is considered). The boundary condition for the wall-normal component of the vorticity is obtained from the no-slip condition at the wall:

$$\omega_z(x, y, z) = \pm 1) = 0\,. \tag{2.89}$$

For the temperature, adiabatic conditions at the walls are enforced:

$$\left.\frac{\partial \theta}{\partial z}\right|_{z=\pm 1} = 0\,. \tag{2.90}$$

A no-flux condition is imposed on the phase field at the walls. Since the phase field transport equation is a fourth-order equation, an additional no-flux condition is imposed at the walls on the phase field chemical potential:

$$\begin{cases} \left.\dfrac{\partial \phi}{\partial z}\right|_{z=\pm 1} = 0 \\ \left.\dfrac{\partial^3 \phi}{\partial z^3}\right|_{z=\pm 1} = 0\,. \end{cases} \tag{2.91}$$

2.6 Code implementation and validation

The numerical method presented has been implemented in an in-house parallel code, written in Fortran-2003. The parallelization strategy is based on a pure-MPI (Message Passing Interface) approach. The overall workload is divided among the different MPI tasks using a 2D domain decomposition, also called pencil decomposition. Within this strategy, the whole domain is split in so-called pencils: the domain is divided along two out of three directions and each sub-domain is assigned to a different MPI process. With respect to the 1D domain decomposition (slab decomposition), 2D decomposition allows to divide the domain among a much higher number of processes at the cost of an increased number of MPI communications. However, it has been observed that, for the problem size we are interested in, the 2D domain decomposition has better performances than the 1D one. A schematic representation of the steps required to compute a three-dimensional transform is shown is figure 2.4. In physical space, the domain is divided along the y and z directions, while in modal space it is divided along the x and y directions. This change in the parallelization is needed when taking the transforms: to compute the Fourier or Chebyshev transforms each process must hold all the point in the transform direction. Therefore, when in physical space, first Fourier transforms are taken along the x-direction, second the parallelization changes in order to have all the points in the y direction. The domain is thus divided along the x and z directions when taking the Fourier transforms along y. Then the parallelization is changed again, switching to a domain division along x and y directions; therefore each MPI process holds all the points in z direction at a certain (x, y) location (parallelization in modal space). Finally, Chebyshev transforms are taken in the z direction. The only MPI communications occur when the parallelization changes, thus two series of MPI communications are needed for each transform from physical (spectral) to spectral (physical) space. After the calculation of all the terms that appear in

Die approbierte gedruckte Originalversion dieser Dissertation ist an der TU Wien Bibliothek verfügbar.
The approved original version of this doctoral thesis is available in print at TU Wien Bibliothek.
TU Bibliothek Your knowledge hub WIEN

the equations, a Helmholtz problem along the wall-normal direction is solved at each (x, y) location independently: during the solving procedure each MPI process works independently from the others. Fast Fourier transforms and Chebyshev transforms are performed using the functions provided in the library *FFTW*. Parallel input/output instructions are employed to read/write large data files, using MPI I/O library. This choice allows a low usage of memory for each task, improving the performances of the code.

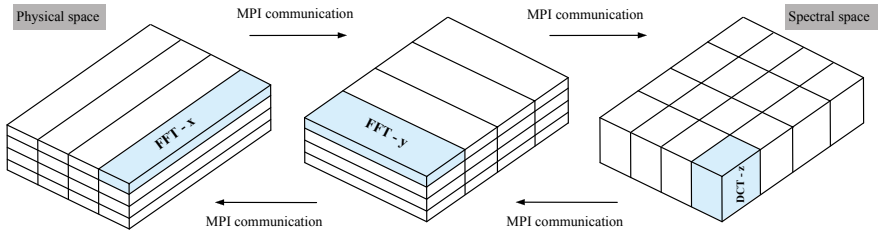

FIGURE 2.4 – Sketch of the parallelization steps and MPI communications required for the computation of a three-dimensional transform. Starting from the physical space (proceeding from left to right in the sketch), the FFT along x is performed; the domain is then reoriented using MPI communications, and the FFT along y is performed; a further reorientation of the domain is then performed to compute the DCT along z. The obtained variables are in the spectral space. The inverse transform can be computed by following analogous steps in the opposite direction (from right to left in the sketch).

The code performances have been evaluated on several High Performance Computing systems, where strong scalability and weak scalability tests have been performed. Among them there are Marconi100, Marconi KNL (CINECA), VSC-4 and VSC-5 (Vienna Scientific Cluster), Discoverer (Sofia-Tech) and LUMI-C (CSC data center). The code has been validated using several benchmarks. The phase field modelling part, in particular, has been validated simulating the cases of the drop deformation in laminar a shear flow, and the Rayleigh Taylor instability. The drop deformation in a laminar shear flow has been compared with an analytical solution. The results from the simulations of the Rayleigh Taylor instability have been instead compared with previous simulations. These benchmarks test various component of the method, as surface tension force, viscosity contrasts and density contrasts.

Die approbierte gedruckte Originalversion dieser Dissertation ist an der TU Wien Bibliothek verfügbar.
The approved original version of this doctoral thesis is available in print at TU Wien Bibliothek.
TU Bibliothek Your knowledge hub WIEN

Die approbierte gedruckte Originalversion dieser Dissertation ist an der TU Wien Bibliothek verfügbar.
The approved original version of this doctoral thesis is available in print at TU Wien Bibliothek.

Die approbierte gedruckte Originalversion dieser Dissertation ist an der TU Wien Bibliothek verfügbar.
The approved original version of this doctoral thesis is available in print at TU Wien Bibliothek.

3

Density, viscosity and surface tension effects on drops and bubbles in turbulence

Reproduced in part from:

F. Mangani, G. Soligo, A. Roccon and A. Soldati, *Influence of density and viscosity on deformation, breakage and coalescence of bubbles in turbulence*, Physical Review Fluids, 7, 053601 (2022).

Large drops or bubbles transported by a turbulent flow are characterized by a complex dynamics, as they deform, break apart or coalesce. This behaviour is governed by the forces generated by the surrounding continuous phase, acting on the surface of the drops/bubbles with shear and normal stresses, and by the response of drops/bubbles, which depends on their surface tension and their density and viscosity. The ultimate competition among these forces determines the number, shape and size distribution of the dispersed phase.

In this chapter the interaction of a swarm of large and deformable drops or bubbles with wall-bounded turbulence will be investigated. The focus of the study is the evaluation of the effect of the density ratio (ratio of dispersed over carrier phase density), the viscosity ratio (ratio of dispersed over carrier phase viscosity) and the surface tension (controlled by the Weber number, ratio of inertial over surface tension forces) on the two-phase dispersed system. Since in most of the considered cases the dispersed phase has a smaller density or viscosity with respect to the carrier phase, the term bubbles, which is more appropriate than drops in this case, will be used hereinafter in this chapter without any loss of generality.

The physical configuration adopted in the study is the bubble-laden turbulent channel flow. This setup has been widely used in the past to investigate different aspects of bubbly flows, from bubbles shape, deformation and clustering to the flow modifications produced by the bubbles themselves. In the pioneering works of Lu & Tryggvason [98, 99], the effects of the bubble size and deformability were investigated: they observed that as bubbles become more deformable, they move towards the middle of the channel and have a relatively small effect on the flow-rate. Scarbolo *et al.* [89, 139], considering a matched density and viscosity system, investigated the effect of the surface tension, observing that surface tension forces play a key role in determining the dispersed phase

topology. Roccon *et al.* [132] studied the effect of the bubble viscosity, finding that for small surface tension values, larger internal viscosities reduce the drop deformability. Recently, Soligo *et al.* [145, 148], considering also the presence of a soluble surfactant, investigated the surfactant effects on drop morphology [145] and flow behaviour [148]. Finally, Hasslberger *et al.*[66] analyzed the coherent structures obtained in a bubble-laden turbulent channel flow while Cannon *et al.* [28] investigated the role played by droplets coalescence on drag in turbulent channel flows.

Building on previous studies [89, 132], this work aims at providing a comprehensive analysis on the effects of density, viscosity and surface tension on the multiphase system. For this purpose, a database of direct numerical simulations is built, where two Weber numbers, $We = 1.5$ and $We = 3.0$, four density ratios, from $\rho_r = 1$ down to $\rho_r = 0.001$, and five viscosity ratios, from $\mu_r = 0.01$ up to $\mu_r = 100$, are considered, while keeping a constant shear Reynolds number, $Re_\tau = 300$, and bubbles volume fraction, $\Phi = 5.4\%$. In order to avoid further complexity in the system, the buoyancy effect associated to the density difference between the fluids will be not taken into account. The first objective is to investigate the effects of these parameters on the dispersed phase topological modifications, namely coalescence and breakage events, and on the morphological modifications, namely bubbles deformation and shape. The second objective is to characterize the global and local modifications produced by the bubbles on the turbulent flow. The numerical framework of the simulations relies on a direct solution of the Navier-Stokes equations coupled with a phase-field method. Direct solutions of the Navier-Stokes equations are used to accurately resolve all the relevant turbulence scales, while the phase-field method [77, 156] is used to describe in a thermodynamically consistent manner the motion of the deformable interface and its topological modifications.

Before proceeding, it is worth to briefly discuss the main capabilities and limitations of interface-resolved simulations in describing topological modifications of the interface [154, 145, 149]. The numerical description of breakages and coalescences is indeed one of the most challenging aspects of interface-resolved simulation methods. As introduced in section 1, fully-resolved simulation of topological changes would require resolving all the scales, from the molecular scale of the interface [131] up to the largest scales of the flow. This type of simulation, however, is way beyond the capabilities of any existing supercomputing facility. A common choice is to avoid resolving the small interfacial scales and to find a way to approximate their dynamics on a much larger scale. Here, following a similar approach, the resolved range is limited to the scales of turbulence: from the Kolmogorov length scale up to the problem size. Thus, phenomena occurring at scales smaller than Kolmogorov are smeared out on the smallest resolved scale. This choice however influences the description of coalescence and breakage events. For coalescences, a part of the physics involved in the coalescence process [81] (i.e. film drainage and rupture) cannot be directly resolved. As a result, regardless of the approach employed to describe coalescence (models for interface tracking methods [153, 100] or implicit description for interface capturing methods [47, 149]), numerical simulations struggle in predicting physical coalescence, with this inaccuracy referred to as numerical coalescence. For breakages, the picture is different and their numerical description is less troublesome. Indeed, being breakage a very quick phenomenon, it can be well approximated without resolving the dynamics at the

Die approbierte gedruckte Originalversion dieser Dissertation ist an der TU Wien Bibliothek verfügbar.
The approved original version of this doctoral thesis is available in print at TU Wien Bibliothek.
TU Bibliothek Your knowledge hub WIEN

molecular scale and there is evidence that the Navier-Stokes equations alone provide an adequate description of a breakage event [50]. Besides, the small time scale of a breakage limits the impact of the approximation on the overall flow dynamics [69, 100]. Therefore, the description of breakages on turbulence-resolved grids is considered to be rather accurate, although in the pinch-off region the smallest interfacial features, characterized by high curvature, may not be perfectly resolved.

The chapter is organized as follows: in section 3.1, the simulation setup and parameters are introduced. Then, in section 3.2, the results obtained from the analysis of the simulations database are presented. The effects of density, viscosity and surface tension are evaluated first on the topology of the dispersed phase and its topological changes (breakage and coalescence), then on the overall interfacial area and interface curvature, and finally on the mean velocity profiles and on the bubbles turbulent kinetic energy (TKE). In section 3.3, the results are summarized and the main conclusions are drawn.

3.1 Simulation setup

A turbulent channel flow at a shear Reynolds number $Re_\tau = 300$ is considered for all the cases. The computational domain has dimensions $L_x \times L_y \times L_z = 4\pi h \times 2\pi h \times 2h$, which corresponds to $L_x^+ \times L_y^+ \times L_z^+ = 3770 \times 1885 \times 600$ wall units. The domain is discretized with $N_x \times N_y \times N_z = 512 \times 256 \times 513$ grid points; the computational grid has uniform spacing in the homogenous directions, while Chebyshev-Gauss-Lobatto points are used in the wall-normal direction. The flow is driven by an imposed constant pressure gradient in the streamwise direction. Two surface tension values are chosen, set through the Weber number: $We = 1.50$ (higher surface tension) and $We = 3.00$ (lower surface tension). The selected values are characteristics of air/water mixtures [79]. For each surface tension value (i.e. for each Weber number), the density ratio is kept unitary and the effect of different viscosity ratios is analysed: from $\mu_r = 0.01$ (less viscous bubbles) up to $\mu_r = 100$ (more viscous bubbles); then, the viscosity ratio is kept unitary and different density ratios are considered: from $\rho_r = 1$ (matched density bubbles) down to $\rho_r = 0.001$ (lighter bubbles). Finally, to evaluate the combined effect of density and viscosity differences, a case in which both bubble density and viscosity are smaller than those of the carrier fluid is considered: $\rho_r = 0.1$ and $\mu_r = 0.1$. In addition, a single-phase flow simulation is performed as a reference case and to provide initial velocity fields for the multiphase simulations. It is worthwhile noting that when different properties (i.e. density and viscosity) are considered, the local value of the Reynolds number changes as well as the range of spatiotemporal scales that needs to be resolved to fulfill the DNS requirements. These modifications can be appreciated from table 3.1 in which we show an estimate of the turbulence length scale inside the dispersed phase (computed from the definition of the Kolmogorov length scale), $\eta_{k,d}^+$, the grid resolution, the final average bubble-size, $\langle d_{eq}^+ \rangle$, and its root mean square value, RMS(d_{eq}^+), for all the different combination of density and viscosity ratios considered as well as for the reference single-phase case. The bubble size has been characterized using the equivalent diameter, d_{eq}^+, i.e. the diameter of an equivalent spherical bubble

Die approbierte gedruckte Originalversion dieser Dissertation ist an der TU Wien Bibliothek verfügbar.
The approved original version of this doctoral thesis is available in print at TU Wien Bibliothek.
TU Bibliothek Your knowledge hub WIEN

with the same volume as the bubble considered [145]:

$$d_{eq}^{+} = \left(\frac{6V^{+}}{\pi}\right)^{1/3} \tag{3.1}$$

where V^{+} is the volume of the bubble. All dimensions are reported in wall units (based on the carrier flow shear Reynolds number) and refer to the channel centre, where most bubbles are located. The Kolmogorov scale, which is used here to provide an estimate of the smallest length scale inside the bubbles, has been computed as follows:

$$\eta_{k,d}^{+} = \left(\frac{\mu_r^2 Re_\tau^2}{\rho_r^2 \epsilon}\right)^{1/4} \tag{3.2}$$

where ϵ is the dissipation at the channel center evaluated in the region characterized by $\phi \geq 0$ (i.e. inside the bubbles), μ_r and ρ_r are the density and viscosity ratios, respectively, and Re_τ is the shear Reynolds number. We can observe that for almost all the cases presented here, the estimated Kolmogorov scale is of the order of the grid spacing thus ensuring a correct resolution of all the relevant flow scales. Only for the cases with $\mu_r \leq 0.1$ (most critical cases due to the largest local Reynolds number increase), the smallest flow scales (which are found inside the bubbles) cannot be completely resolved. From table 3.1, we can also observe that the average bubble size is always at least one order of magnitude larger than the grid spacing.

For the phase field, the Cahn number is set to $Ch = 0.02$. This value is selected based on the grid resolution: at least three grid points are required across the interface to accurately describe the steep gradients present [146]. The phase field Péclet number has been set according to the scaling $Pe_\phi = 1/Ch = 50$, to achieve convergence to the sharp interface limit [167, 103]. More refined grids allow to reduce the thickness of the interface and to adopt smaller Cahn numbers. However, the resulting computational cost is much larger: grid resolution needs to be refined along all three directions, as the orientation of the interfacial layer is arbitrary, and the time step has to be reduced as well to satisfy the Courant–Friedrichs–Lewy condition. Overall, the computational cost of a simulation with an halved Cahn number is roughly 16 times larger: grid refinement makes the simulation eight times more expensive and the time step limitation makes the simulation twice as expensive.

At the beginning of each simulation, a regular array of 256 spherical droplets with diameter $d = 0.4h$ (corresponding to $d^{+} = 120$ wall units) is initialized in a fully-developed single-phase turbulent channel flow. The total volume fraction of the dispersed phase is $\Phi = V_d/(V_c + V_d) \simeq 5.4\%$, being V_d and V_c the volume of the dispersed and carrier phase, respectively. As the array of spherical bubbles is suddenly released in a single-phase turbulent flow, turbulent velocity fluctuations strongly perturb the interfacial profile; during this initial coupling phase, mass leakages among the phases may occur [167, 147] After this initial transient, the mass of each phase keeps constant over time. While the initial condition chosen for the dispersed phase may seem unphysical, after a short transient, memory of the initial condition is completely lost and the results are not affected by the initial condition selected [145]· Different initial conditions have been tested (e.g., the injection of a thin liquid sheet at the channel center) and the same statistically statistically-stationary results were obtained.

Die approbierte gedruckte Originalversion dieser Dissertation ist an der TU Wien Bibliothek verfügbar.
The approved original version of this doctoral thesis is available in print at TU Wien Bibliothek.
TU Bibliothek Your knowledge hub WIEN

System	We	μ_r	ρ_r	Δx^+	Δy^+	Δz^+	$\eta^+_{k,d}$	$\langle d^+_{eq} \rangle$	RMS(d^+_{eq})
SP	-	-	-	7.36	7.36	1.84	4.19	-	-
BL1	1.50	0.01	1	7.36	7.36	1.84	0.20	195.13	176.97
BL2	1.50	0.1	1	7.36	7.36	1.84	1.04	191.16	134.04
BL3	1.50	1	1	7.36	7.36	1.84	5.27	226.72	123.55
BL4	1.50	10	1	7.36	7.36	1.84	26.72	229.84	127.99
BL5	1.50	100	1	7.36	7.36	1.84	145.50	245.04	104.51
BL6	1.50	1	0.001	7.36	7.36	1.84	887.50	208.15	150.61
BL7	1.50	1	0.01	7.36	7.36	1.84	185.80	230.31	142.16
BL8	1.50	1	0.1	7.36	7.36	1.84	30.66	180.60	142.73
BL9	1.50	0.1	0.1	7.36	7.36	1.84	5.86	186.00	138.08
BL10	3.00	0.01	1	7.36	7.36	1.84	0.19	81.37	74.77
BL11	3.00	0.1	1	7.36	7.36	1.84	0.94	84.06	76.15
BL12	3.00	1	1	7.36	7.36	1.84	4.87	87.56	79.55
BL13	3.00	10	1	7.36	7.36	1.84	24.96	89.70	77.94
BL14	3.00	100	1	7.36	7.36	1.84	140.3	203.62	111.09
BL15	3.00	1	0.001	7.36	7.36	1.84	818.2	87.58	77.74
BL16	3.00	1	0.01	7.36	7.36	1.84	142.0	86.54	76.25
BL17	3.00	1	0.1	7.36	7.36	1.84	27.45	91.16	81.28
BL18	3.00	0.1	0.1	7.36	7.36	1.84	4.63	83.62	75.41

TABLE 3.1 – Grid resolution, Δx^+, Δy^+ and Δz_c^+, Kolmogorov scale at the channel centre in the dispersed phase, $\eta^+_{k,d}$, average equivalent diameter of the bubbles, $\langle d^+_{eq} \rangle$, and root mean square of the bubble equivalent diameter, RMS(d^+_{eq}), for all the different simulations performed. All dimensions are reported in wall units; Kolmogorov scale is measured at the channel centre. Single-phase flow values at the channel centre have been also reported as a reference.

We selected the current initial configuration as it reduces the time required to reach statistically-stationary conditions.

3.2 Results

We present here the results obtained from the analysis of the simulation database, starting from the effects of the density ratio, viscosity ratio, and Weber number on the topology of the dispersed phase (number of bubbles) and on its topological changes (coalescence and breakage rates). Then we evaluate the effects of these parameters on the shape and deformation of the bubbles studying the local curvature of the interface and the time evolution of the interfacial area. Finally, we investigate the flow modifications produced by the bubbles by analyzing the mean velocity profiles and the turbulent kinetic energy inside the bubbles. All the results will be presented according to the following color code: a red-colors scale is used to show the density ratio variations and a blue-colors scale to show the viscosity ratio variations. The case with both non-matched density and viscosity is represented in green, while the reference case (matched density and matched viscosity) is shown in black.

Die approbierte gedruckte Originalversion dieser Dissertation ist an der TU Wien Bibliothek verfügbar.
The approved original version of this doctoral thesis is available in print at TU Wien Bibliothek.
TU Bibliothek Your knowledge hub WIEN

System	Re_τ	We	μ_r	ρ_r	Ch	Pe_ϕ
SP	300	-	-	-	-	-
BL1	300	1.50	0.01	1	0.02	50
BL2	300	1.50	0.1	1	0.02	50
BL3	300	1.50	1	1	0.02	50
BL4	300	1.50	10	1	0.02	50
BL5	300	1.50	100	1	0.02	50
BL6	300	1.50	1	0.001	0.02	50
BL7	300	1.50	1	0.01	0.02	50
BL8	300	1.50	1	0.1	0.02	50
BL9	300	1.50	0.1	0.1	0.02	50
BL10	300	3.00	0.01	1	0.02	50
BL11	300	3.00	0.1	1	0.02	50
BL12	300	3.00	1	1	0.02	50
BL13	300	3.00	10	1	0.02	50
BL14	300	3.00	100	1	0.02	50
BL15	300	3.00	1	0.001	0.02	50
BL16	300	3.00	1	0.01	0.02	50
BL17	300	3.00	1	0.1	0.02	50
BL18	300	3.00	0.1	0.1	0.02	50

TABLE 3.2 – Overview of simulations parameters. We analyze two Weber numbers: $We = 1.50$ and $We = 3.00$. For each Weber number, we consider four density ratios: from $\rho_r = 0.001$ up to $\rho_r = 1$; five viscosity ratios: from $\mu_r = 0.01$ up to $\mu_r = 100$ and a combined case $\rho_r = 0.1$ and $\mu_r = 0.1$. In addition, a single-phase flow simulation has been also conducted.

3.2.1 Bubbles topological modifications

Number of bubbles

The topology of the dispersed phase is the direct consequence of the ultimate competition between breakage and coalescence events. To obtain a first qualitative insight of the effects of density ratio, viscosity ratio and Weber number on the statistically-stationary number of bubbles (i.e. once the effect of the initial condition is completely dissipated), we can consider figure 3.2. Panel (a) refers to $We = 1.5$, while panel (b) to $We = 3.0$. In each panel of figure 3.2, four snapshots of the multiphase system at statistically-stationary are arranged in a plot according to the values of density (horizontal axis) and viscosity (vertical axis) ratio of each case. The surface of the bubbles, identified as the iso-contour $\phi = 0$, is reported at the time instant $t^+ = 4000$ (statistically-stationary conditions); in the background the contour map of the turbulent kinetic energy, TKE= $(\rho/\rho_c)(u'^2+v'^2+w'^2)/2$ (where ρ identifies the local density value, ρ_d in the bubbles and ρ_c in the carrier phase), on a $x^+ - y^+$ plane located at the channel centre is shown. Among all cases, we select those with the extreme values of the density ($\rho_r = 0.001$ - $\mu_r = 1$) and viscosity ratio ($\rho_r = 1$ - $\mu_r = 100$ and $\rho_r = 1$ - $\mu_r = 0.01$). As a reference, also the matched density and viscosity case ($\rho_r = 1$ - $\mu_r = 1$) is shown. We can observe that for $We = 1.5$ (figure 3.2a), the number of bubbles remains almost unchanged when both density and viscosity contrasts are

Die approbierte gedruckte Originalversion dieser Dissertation ist an der TU Wien Bibliothek verfügbar.
The approved original version of this doctoral thesis is available in print at TU Wien Bibliothek.
TU Bibliothek Your knowledge hub WIEN

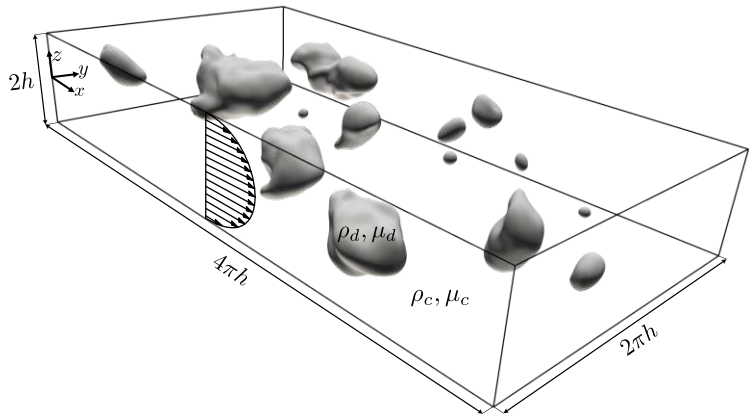

FIGURE 3.1 – Sketch of the computational domain. A swarm of drops with density ρ_d and viscosity μ_d is released in turbulent carrier fluid with density ρ_c and viscosity μ_c. The wall-bounded channel has dimensions $4\pi h \times 2\pi h \times 2h$; the flow is driven by a constant pressure gradient imposed along the streamwise direction (x). A sketch of the mean velocity profile is also reported.

introduced in the system. For $We = 3.0$ (figure 3.2*b*), the number of bubbles is higher in all the cases, compared to $We = 1.5$. If we then look along the density axis (namely to the pictures in the central row) of figure 3.2*b*, we see that the number of bubbles is quite similar in the two cases, suggesting a negligible effect of density for the range of values considered here. By opposite, looking along the viscosity axis (thus to the pictures on the right column), we notice that viscosity does play an important role, as the number of bubbles significantly reduces from $\mu_r = 0.01$ to $\mu_r = 100$, with a more marked difference between $\mu_r = 1$ and $\mu_r = 100$, than between $\mu_r = 0.01$ and $\mu_r = 1$, thus hinting that the viscosity difference among the phases may actually be the relevant factor, rather than the viscosity ratio.

To evaluate these results more quantitatively, we compute at each time the number of bubbles, $N(t^+)$, normalized by the initial bubbles number, N_0. Figure 3.3 shows the results obtained for all the combination of density and viscosity ratios considered, and for the two Weber numbers as well. Left column refers to $We = 1.5$ (figure 3.3*a*,*c*,*e*), while the right column to $We = 3.0$ (figure 3.3*b*,*d*,*f*). The top, middle and bottom rows show, in order, the effects of the density ratio, viscosity ratio and of their combination.

We start by analyzing the effect of Weber number solely and we consider the matched density and viscosity case (black lines in figure 3.3*a*-*d*).

For $We = 1.5$, the number of bubbles decreases monotonically: coalescence events dominate the initial transient phase (up to $t^+ = 2000$). Then a balance between breakage and coalescence events is attained and the number of bubbles settles on a stationary value, $N(t^+)/N_0 \simeq 0.1$.

Likewise, for $We = 3.0$, an initial transient mainly characterized by coalescence events can be also observed. However, this phase ends at an earlier time (about $t^+ = 500$) and is followed by a statistically-stationary condition where breakups and coalescences alternately prevail on each other.

Die approbierte gedruckte Originalversion dieser Dissertation ist an der TU Wien Bibliothek verfügbar.
The approved original version of this doctoral thesis is available in print at TU Wien Bibliothek.
TU Bibliothek Your knowledge hub WIEN

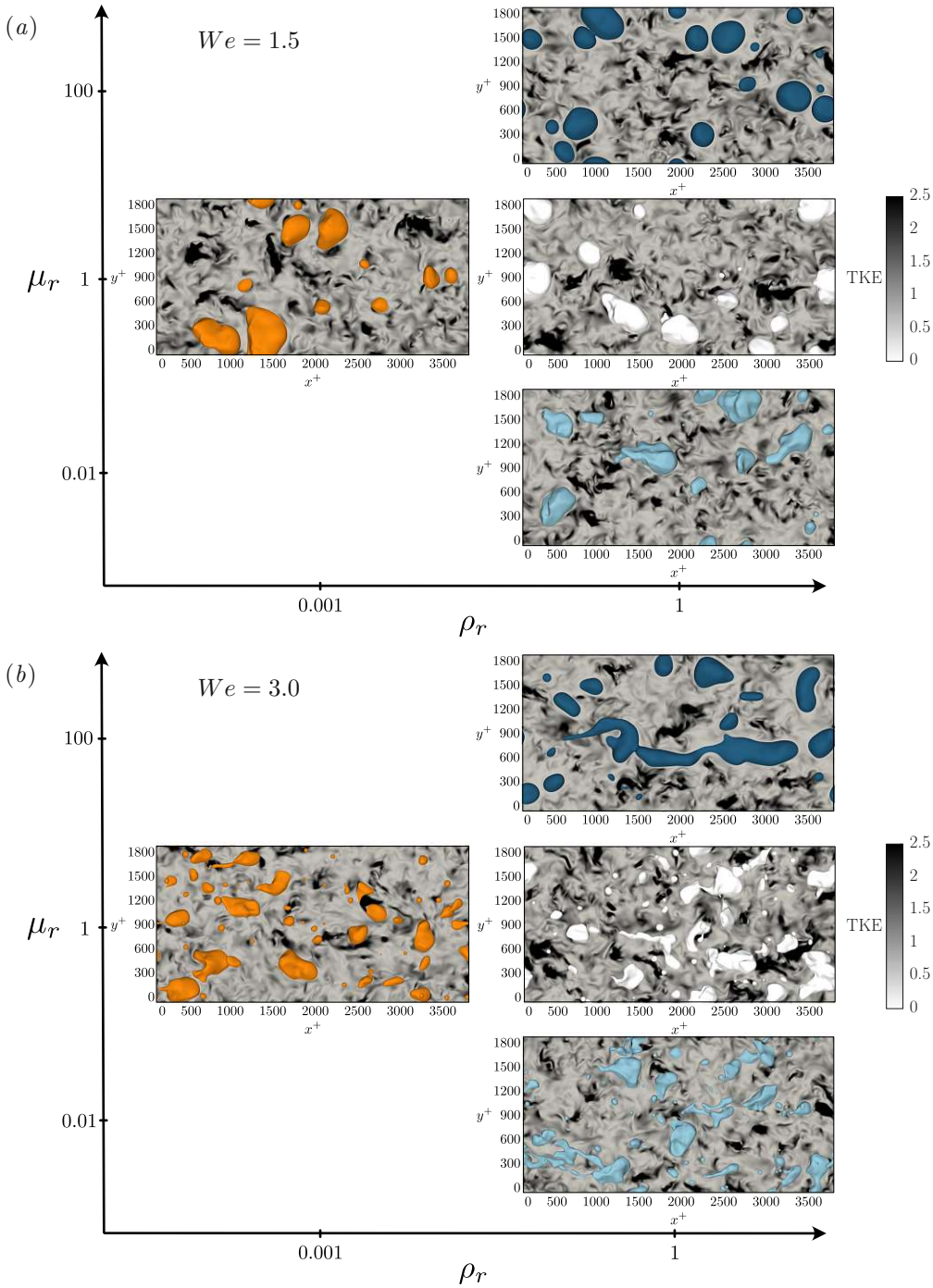

FIGURE 3.2 – Top view of four statistically-stationary configurations ($t^+ = 4000$) for different combinations of density ratios ($\rho_r = 0.001$ and 1) and viscosity ratios ($\mu_r = 0.01, 1$ and 100). Panel (a) refers to $We = 1.5$, while panel (b) to $We = 3.0$. The sub-panels are arranged in a plot using ρ_r as x-coordinate and μ_r as y-coordinate. The effect of density can be appreciated in the sequence of panels on the middle row, while that of viscosity in the right column. The background of the plot shows the turbulent kinetic energy, TKE= $(\rho/\rho_c)(u'^2 + v'^2 + w'^2)/2$ (white-low; black-high), computed on the central $x^+ - y^+$ plane of the channel.

Die approbierte gedruckte Originalversion dieser Dissertation ist an der TU Wien Bibliothek verfügbar.
The approved original version of this doctoral thesis is available in print at TU Wien Bibliothek.
TU Bibliothek Your knowledge hub WIEN

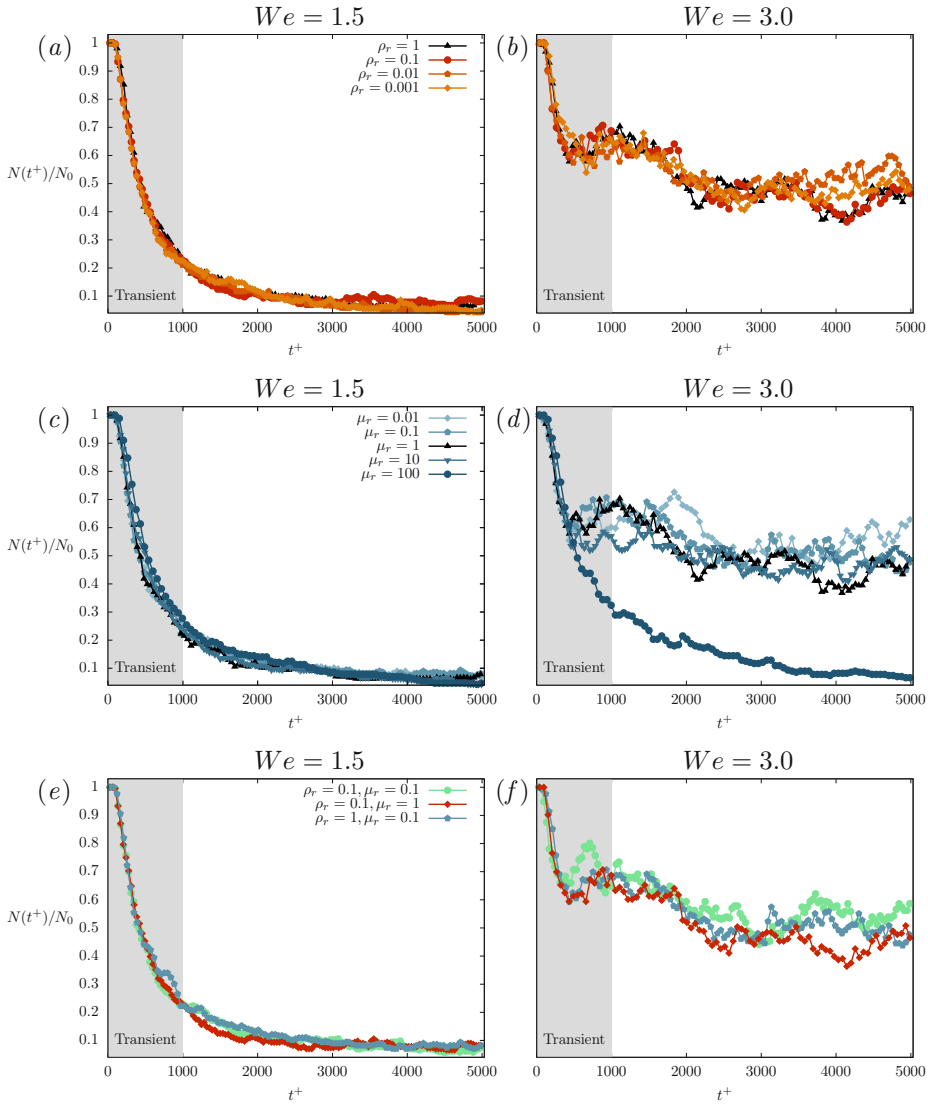

FIGURE 3.3 – Time evolution of the number of bubbles, $N(t^+)$, normalized by its initial value N_0. Left column refers to $We = 1.5$, while the right column to $We = 3.0$. Top row: effect of density ratio, for $\rho_r = 0.001, 0.01, 0.1$ and 1 (with $\mu_r = 1$); Middle row: effect of viscosity ratio, for $\mu_r = 0.01, 0.1, 1, 10$ and 100 (with $\rho_r = 1$); Bottom row: combined effect of density and viscosity, for the case with $\rho_r = 0.1$, the cases $\rho_r = 0.1$, $\mu_r = 1$ and $\rho_r = 1$, $\mu_r = 0.1$ are reported for reference. On each line the left plot also includes the color code and a sketch with the definition of the property ratio considered (ρ_r, μ_r or both ratios).

Die approbierte gedruckte Originalversion dieser Dissertation ist an der TU Wien Bibliothek verfügbar.
The approved original version of this doctoral thesis is available in print at TU Wien Bibliothek.
TU Bibliothek Your knowledge hub WIEN

Comparing simultaneously the plots at $We = 1.5$ (figure 3.3*a*,*c*,*e*), we can observe that the effects of both density and viscosity ratios (and of their combination) are very small. This behaviour can be traced back to the dominant role played by surface tension forces. The Weber number quantifies the relative importance of surface tension forces with respect to inertial forces: the lower is the Weber number, the stronger is the action of surface tension in controlling bubbles dynamics. Thus, for $We = 1.5$, the surface tension forces are dominant and are those determining the topology of the dispersed phase (i.e. number of bubbles). For the higher Weber, surface tension forces are weaker in comparison, and density and viscosity ratios effects become more significant. In particular, for $We = 3.0$ (figure 3.3*b*,*d*,*f*), the statistically-stationary value obtained for the number of bubbles shows a marked dependence on the viscosity ratio.

As the dispersed phase dynamics for the cases at $We = 1.5$ are dominated by surface tension forces, we focus on the cases at $We = 3.0$ to investigate the effects of density and/or viscosity ratios. First, we consider the effects of the density ratio solely. Figure 3.3*b* shows the time evolution of the number of bubbles for different density ratios (from $\rho_r = 1.0$ down to $\rho_r = 0.001$) and a fixed unitary viscosity ratio. We notice that the influence of the density ratio on the number of bubbles is small: the red-colors lines do not depart in average from the black reference line, nor from each other. Hence, no significant modifications are introduced in the topology of the dispersed phase when density contrasts are present between the phases (with respect to a two-phase system with uniform density). This behaviour suggests that, for the range of density ratios considered, the external inertial forcing is the main factor that determines the bubble size and thus the dispersed phase topology. In contrast, the density (and thus the inertia) of the bubble plays a negligible role in determining the dispersed phase topology.

On the other hand a marked effect of the viscosity ratio alone can be observed, figure 3.3*d*. We observe in this case a much clearer trend: after the initial transient the curves depart from each other and set on different equilibrium values once statistically-stationary conditions are reached. In particular, as the viscosity ratio is increased, the statistically-stationary number of bubbles is reduced. For high viscosity ratio ($\mu_r > 1$) fragmentation is prevented, coalescence dominates and only a few bubbles are present in the channel. By opposite, for low viscosity ratio ($\mu_r < 1$) breakups are favored, the average bubble size decreases, and the resulting number of bubbles is slightly larger when smaller viscosity ratios are considered. Hence, it is evident that viscosity acts as a stabilizing factor, in a similar way as surface tension does. Indeed, it is interesting to observe that the behaviour of the number of bubbles for $\mu_r = 100$ at $We = 3.0$ (high viscosity) resembles those of the cases at $We = 1.5$ (high surface tension, figure 3.3*c*). This suggests that a very high viscosity ratio can compensate a low surface tension and produce similar results in terms of topology. A physical argument that can explain the action of viscosity is related to the deformations that the external turbulent flow is able to induce on the bubble. When the internal viscosity is larger than the external one, the larger internal viscous dissipation damps all the turbulent fluctuations produced by the external flow. This hinders large deformations of the bubble surface and, as a consequence, it reduces the possibility of bubble breakage.

Finally, we analyze the combined effects of density and viscosity ratios. In figure 3.3*f*,

Die approbierte gedruckte Originalversion dieser Dissertation ist an der TU Wien Bibliothek verfügbar.
The approved original version of this doctoral thesis is available in print at TU Wien Bibliothek.
TU Bibliothek Your knowledge hub WIEN

we report the results obtained from the case $\rho_r = 0.1$ and $\mu_r = 0.1$ and from two cases with one matched property and one non-matched property, $\rho_r = 0.1$ and $\mu_r = 1$ (red line) and $\rho_r = 1$ and $\mu_r = 0.1$ (blue line). We can first note that these two latter cases, where only one property is non-matched, exhibit a very similar behaviour for the entire duration of the simulation. This is consistent with our previous observation: the influence of the density ratio is almost negligible (figure 3.3*b*) and the effects of the viscosity ratio are relatively small for $\mu_r = 0.1$ (figure 3.3*d*). Then, we observe that the combined case (green line) does not deviate largely from the other two cases. This indicates that a simultaneous reduction of the density and viscosity ratios does not remarkably modify the general picture for the range of density and viscosity ratios here tested. Nevertheless, it is interesting to observe that the green line lies above the red and blue lines for a longer timespan, indicating that the number of bubbles for the combined case is slightly higher than in the other two cases.

Breakage and coalescence rates

The evolution of the number of bubbles provides useful insights on the time behaviour of the dispersed phase topology, although it only shows the net outcome of the competition between breakage and coalescence events.
To evaluate whether density and viscosity differences among the phases affect breakage and coalescence dynamics, we compute the instantaneous number of breakage and coalescence events. Evaluating these effects is not only crucial to better understand the involved physics, but is also extremely important for the development of accurate coalescence and breakage kernels [51]. The time behaviour of the breakage and coalescence is directly linked to the number of bubbles present in the channel, as hinted by the balance population equation [90]:

$$\frac{dN(t^+)}{dt^+} = \dot{N}_b(t^+) - \dot{N}_c(t^+) \,, \tag{3.3}$$

where $N(t^+)$ is the number of bubbles and $\dot{N}_b(t^+)$ and $\dot{N}_c(t^+)$ are respectively the breakage and coalescence rates.
We compute the breakage and coalescence rates counting the number of breakage or coalescence events that occur within a set temporal window Δt^+:

$$\dot{N}_b(t^+) = \frac{N_b}{\Delta t^+}, \qquad \dot{N}_c(t^+) = \frac{N_c}{\Delta t^+} \,, \tag{3.4}$$

where the temporal window has been chosen equal to $\Delta t^+ = 300$. As the number of breakage and coalescence events that occur in a certain temporal window is also influenced by the number of bubbles present in the channel [145], we normalize the breakage and coalescence rates, $\dot{N}_b(t^+)$ and $\dot{N}_c(t^+)$, by the instantaneous number of bubbles $N(t^+)$. Being the description of coalescence and breakage events in numerical simulations influenced by grid resolution [62, 154, 145, 149], a convergence study has been also performed to ensure that the grid employed is sufficient to obtain convergent results.
Figure 3.4 shows the results obtained for all cases examined: breakage rate is plotted over time as a positive quantity, while coalescence rate as a negative quantity, being them related to an increase and decrease of the number of bubbles, respectively.

Die approbierte gedruckte Originalversion dieser Dissertation ist an der TU Wien Bibliothek verfügbar.
The approved original version of this doctoral thesis is available in print at TU Wien Bibliothek.
TU Bibliothek Your knowledge hub WIEN

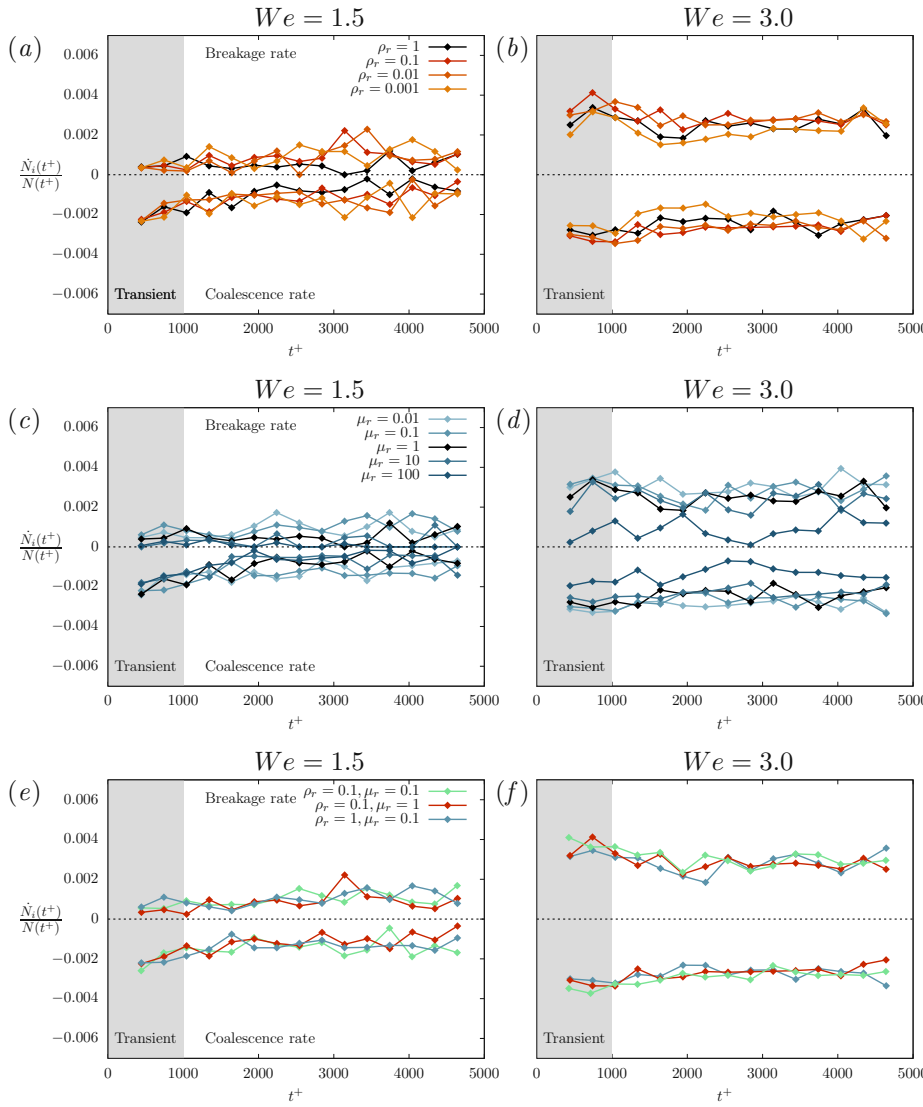

FIGURE 3.4 – Time evolution of the normalized breakage rate, $\dot{N}_b(t^+)/N(t^+)$, and coalescence rate, $\dot{N}_c(t^+)/N(t^+)$. Left column refers to $We = 1.5$, while right column to $We = 3.0$. Top row: effect of density ratio, for $\rho_r = 0.001, 0.01, 0.1$ and 1 (with $\mu_r = 1$); Middle row: effect of viscosity ratio, for $\mu_r = 0.01, 0.1, 1, 10$ and 100 (with $\rho_r = 1$); Bottom row: combined effect of density and viscosity ratios, for the case with $\rho_r = 0.1$, $\mu_r = 0.1$. Cases $\rho_r = 0.1$, $\mu_r = 1$ and $\rho_r = 1$, $\mu_r = 0.1$ are reported for reference. For each row of plots, the left plot also shows the color code and a sketch with the definition of the ratio considered (ρ_r, μ_r or both).

Die approbierte gedruckte Originalversion dieser Dissertation ist an der TU Wien Bibliothek verfügbar.
The approved original version of this doctoral thesis is available in print at TU Wien Bibliothek.
TU Bibliothek Your knowledge hub WIEN

We will first discuss the effect of the Weber number comparing the left column (figure 3.4*a*,*c*,*e*) with the right column (figure 3.4*b*,*d*,*f*). For $We = 1.5$ (left column), the breakage and coalescence rates behave nearly in the same way for all the combinations of density and viscosity ratios. After the initial transient where the behaviour of the rates is influenced by the selected initial condition for the phase-field, an equilibrium is reached at about $t^+ = 1000$ where both rates set on a constant value. At this stage, bubbles keep on breaking and coalescing, but with the same rate, thus maintaining their number in statistical equilibrium. This value of the Weber number does not allow density and viscosity contrasts to substantially modify the evolution of bubbles topology, as a good correspondence among the curves can be noticed in all the plots. Indeed, when a low Weber number is considered the deformability, which is a crucial factor for coalescence and breakage events, is mainly determined by surface tension forces that dominate over density and viscosity contributions. For $We = 3.0$ (right column), the results are qualitatively and quantitatively different: breakage and coalescence rates reach in general larger values, and some significant deviations among the curves are visible. This is a direct consequence of the larger Weber number: surface tension forces, which are smaller in magnitude, weakly counteract turbulent velocity gradients, that can more easily deform and break the bubbles.

Thus, we observe a larger number of breakage and coalescence events due to the larger deformability of the bubbles, as can be appreciated from figure 3.3*b*,*d*,*f*. In addition, for this larger Weber number, we can clearly observe how the density and viscosity ratios play a much more important role in the dynamics of breakage and coalescence events (with respect to $We = 1.5$).

For this reason, we move now to discuss the effect of non-matched density or viscosity on the cases at $We = 3.0$ in more detail. Figure 3.4*b* shows the breakage and coalescence rate for different values of the density ratios. In the first transient phase, all cases manifest a very high frequency of both breakage and coalescence events, slightly larger for coalescences at the very beginning (coherently with the evolution of the number of bubbles shown in figure 3.3*b*). Later on, both rates stabilize and set on two equal (in magnitude) stationary values. Although a clear trend among the different density ratios cannot be observed, it is worth noticing that all the rates seem slightly larger when sub-unitary density ratios are considered (especially in the early stage of simulations).

Overall, these observations suggest that density differences between the phases do not introduce remarkable changes in the dispersed phase topology and on its modifications: the number of bubbles and breakage and coalescence rates are weakly influenced by changing the density ratio.

Moving now to the effect of the viscosity ratio, figure 3.4*d* depicts the time evolution of the breakage and coalescence rates obtained for different viscosity ratios (and a fixed unitary density ratio). Again, once the initial transient is finished, a statistically-stationary phase can be distinguished for all cases. From a qualitative viewpoint, coalescence is predominant at the beginning of the transient (consistently with the behaviour reported in figure 3.3*d*); then relatively high values for both rates are maintained during the rest of the transient, until they stabilize on steady values. The cases, however, deeply differ from a quantitative point of view. We see in this case that the rates significantly change when the viscosity ratio is changed: both break-

Die approbierte gedruckte Originalversion dieser Dissertation ist an der TU Wien Bibliothek verfügbar.
The approved original version of this doctoral thesis is available in print at TU Wien Bibliothek.
TU Bibliothek Your knowledge hub WIEN

age and coalescence rates decrease in magnitude as the viscosity ratio is increased (i.e. when bubble viscosity is increased). This modification of the breakage and coalescence rates is clear when the case $\mu_r = 100$ is considered: the statistically-steady value of both rates is smaller than the one attained by the other cases. A similar trend was experimentally measured by Eastwood et al. [49] for the breakup of immiscible fluid particles in a turbulent jet: it was observed that the breakage rate of the droplets scales inversely with the inner bubble capillary number (ratio between bubble viscous forces and surface tension forces). Present results seem to confirm this finding: bubble viscosity and the corresponding viscous forces, acting as a damper of external velocity fluctuations [132], make bubbles less deformable and the probability of breakage and coalescence decreases.

Finally, we discuss the combination of density and viscosity contrasts (figure 3.4*f*). The three curves do not deviate considerably from each other and a clearcut trend cannot be appreciated.

As the density effect is generally unimportant and the viscosity one shall be small for $\mu_r = 0.1$, the case $\rho_r = 0.1$ - $\mu_r = 0.1$ does not give us clear information on how density and viscosity effects combine together.

3.2.2 Bubbles morphological modifications

Interfacial area

A bubble released in a turbulent flow is constantly subjected to deformations due to the action of turbulent fluctuations [137, 159]. Turbulence fluctuations deform and stretch the bubble and, if strong enough, can lead to breakage of the bubble. The result of turbulence actions in terms of deformation can be evaluated by computing the total interfacial area. This quantity gives a general indication of the average bubble deformation and also provides a quantification of the amount of energy stored at the interface [80, 47, 134]. Indeed, in the hypothesis of constant surface tension (as in the present case), surface tension energy is proportional to the amount of interfacial area available [80, 47, 134].

With the aim of evaluating the effects of the simulations parameters (density ratio, viscosity ratio, and Weber number) on the interfacial energy, we compute the time behaviour of total interfacial area, $A(t^+)$, for all cases considered. The results are presented normalized by the initial value A_0. In figure 3.5, the results are shown using the same arrangement adopted in the previous figures. To correctly interpret these results, it is necessary to make a preliminary remark. The area of the interface between the dispersed phase and the carrier fluid evolves in time depending on two factors: the evolution of the number of bubbles and the modifications of the shape of the bubbles. This concept can be explained by considering the following example: to have a minimal interface area, the dispersed phase should consist of a unique spherical bubble, since, for a given volume, the spherical shape is the one that minimizes the surface area. If we split this bubble into several smaller spherical bubbles the total interface area will increase, being the total volume constant. If these smaller spherical bubbles are then deformed and elongated the area will further increase, as for each bubble the same mass will be redistributed in a way that makes it more exposed to the

Die approbierte gedruckte Originalversion dieser Dissertation ist an der TU Wien Bibliothek verfügbar.
The approved original version of this doctoral thesis is available in print at TU Wien Bibliothek.
TU Bibliothek Your knowledge hub WIEN

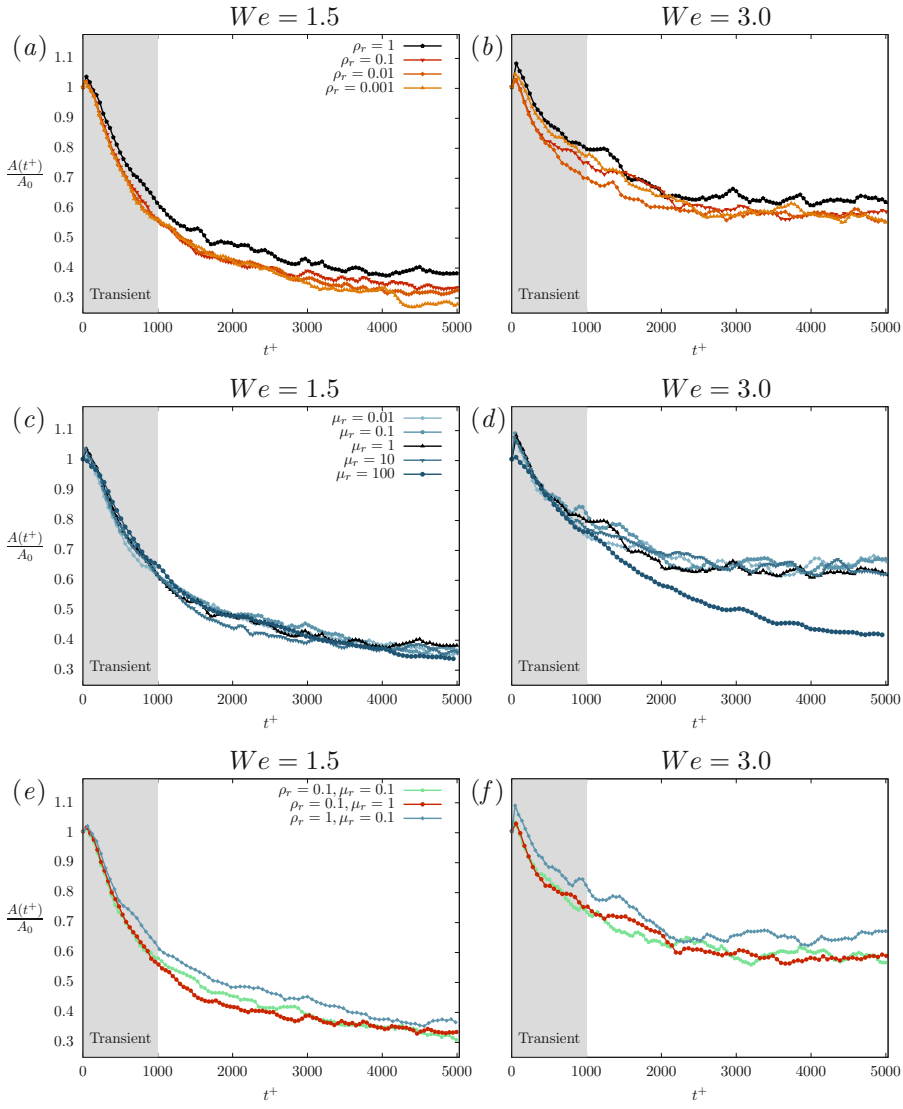

FIGURE 3.5 – Time evolution of the total interface area $A(t^+)$, normalized by its initial value A_0. Top row: effect of density, for $\rho_r = 0.001, 0.01, 0.1$ and 1 (with $\mu_r = 1$); Middle row: effect of viscosity, for $\mu_r = 0.01, 0.1, 1, 10$ and 100 (with $\rho_r = 1$); Bottom row: combined effect of density and viscosity, for the case with $\rho_r = 0.1$, $\mu_r = 0.1$. Cases with $\rho_r = 0.1$, $\mu_r = 1$ and $\rho_r = 1$, $\mu_r = 0.1$ are reported for reference. These effects are shown for two different Weber numbers: (a)-(c)-(e) $We = 1.5$ and (b)-(d)-(f) $We = 3.0$. On each row the left plot also includes the colour code and a sketch with the definition of the ratio considered (ρ_r, μ_r or both ratios).

Die approbierte gedruckte Originalversion dieser Dissertation ist an der TU Wien Bibliothek verfügbar.
The approved original version of this doctoral thesis is available in print at TU Wien Bibliothek.
TU Bibliothek Your knowledge hub WIEN

external flow. Thus, when we look at the evolution of the total interface area we are simultaneously observing the effect of the number of bubbles and of their deformation.

We start by analyzing the effects of the density ratio for the cases at $We = 1.5$, figure 3.5*a*. We notice an initial transient that is characterized by a nearly monotonic decrease of $A(t^+)/A_0$, for all the considered cases. In particular, during this transient, the curves corresponding to sub-unitary density ratios are superposed, while a remarkable discrepancy is visible between them and $\rho_r = 1$. As soon as the flow reaches a steady behaviour, all the curves differentiate and a trend becomes visible, where the higher is the density ratio the larger is the total interface area. Considering that for $We = 1.5$ the number of bubbles is almost unaffected by the density ratio (figure 3.3*a*), this indicates that the trends observed in figure 3.5*a* are mainly caused by the bubble deformation: when smaller density ratios are considered, bubbles tend to be less deformed with respect to the case $\rho_r = 1$. The origin of this behaviour can be traced back to the local Reynolds number (i.e. evaluated using the bubble proprieties): as the density ratio is decreased, the inertial forces become smaller, the local Reynolds number decreases and less deformed bubbles are obtained.

For $We = 3.0$ (figure 3.5*b*), we notice a similar but more irregular behaviour. For all density ratios, the normalized interfacial area decreases and sets on stationary values that are higher than the final stationary values obtained for $We = 1.5$ (figure 3.5*a*). This is coherent with the fact that increasing the Weber number, the number of bubbles increases, and so does the interfacial area. For this larger Weber number, the trend among the different density ratios is now less clear and the differences between the curves are slightly smaller. Nevertheless, consistently with the results obtained for $We = 1.5$ (figure 3.5*a*), the matched density case ($\rho_r = 1$) is clearly above all the other curves ($\rho_r < 1$) for almost the entire time range of the simulations. Being the number of bubbles similar for all the cases shown in figure 3.5*b*, this seems to confirm that for smaller density ratios the overall interfacial area is reduced.

The viscosity effect can be appreciated in figure 3.5*c,d*. For $We = 1.5$ (panel *c*), the total interface area is practically independent on the viscosity ratio and no significant changes can be observed. As the number of bubbles is similar for all cases (figure 3.3*c*), this indicates that no significant effects on the average bubble deformation are observed. Even though bubble viscosity does not play an important role in the average bubble deformation, we can anticipate that it still plays a role when more local quantities are analyzed (e.g. local curvature), as discussed in the following section. For $We = 3.0$, a remarkable difference is present between $\mu_r = 100$ (larger bubble viscosity) and all the other cases. This is consistent with the time evolution of the number of bubbles (figure 3.3*d*). Indeed, when the statistically-stationary configuration is reached, the number of bubbles for $\mu_r = 100$ is much lower than that obtained for the other ratios. As a result, the interfacial area is much lower than the other cases. For the other cases (from $\mu_r = 10$ down to $\mu_r = 0.01$), a clear trend cannot be observed thus suggesting that no large modifications of the average bubble deformation are obtained for $\mu_r < 10$. However, as already anticipated for $We = 1.5$, larger modifications are observed when local quantities are analyzed, see next section for details.

Finally, we discuss the combined effect of density and viscosity ratios (figure 3.5*e,f*). For $We = 1.5$, the case with both non-matched density and viscosity (green line)

Die approbierte gedruckte Originalversion dieser Dissertation ist an der TU Wien Bibliothek verfügbar.
The approved original version of this doctoral thesis is available in print at TU Wien Bibliothek.
TU Bibliothek Your knowledge hub WIEN

overlaps the case with non-matched density (red line) during the transient and in the final steady configuration, while in the first steady part it is intermediate between the two other cases, $\rho_r = 0.1$ - $\mu_r = 1$ and $\rho_r = 1$ - $\mu_r = 0.1$. On average the combined case is therefore closer to the non-matched density case, suggesting that the density ratio has a larger influence on the total interfacial area (and thus on the stretching of the bubbles) with respect to the viscosity ratio. This is confirmed by the plot for $We = 3.0$, where the green line shows again values that on average are much closer to the non-matched density case (i.e. $\rho_r = 0.1$).

Probability density function of mean curvature

The evolution of the total interface area gives us an idea of the overall behaviour of the average deformation of the bubbles in presence of density and viscosity contrasts. However, being an average indication, it does not provide a clear indication of the local deformations of the bubbles surface. To obtain a deeper understanding of the deformation, we examine the probability density function (PDF) of the local interface mean curvature in the final statistically-stationary configuration. The mean curvature, $\mathcal{K}^+$, can be computed as the divergence of the local normal vector $\mathbf{n}$, which in turn can be defined from the phase variable ϕ [4, 150]:

$$\mathbf{n} = -\frac{\nabla\phi}{|\nabla\phi|}, \qquad \mathcal{K}^+ = \nabla \cdot \left(-\frac{\nabla\phi}{|\nabla\phi|} \right). \tag{3.5}$$

We compute the mean curvature, $\mathcal{K}^+$, for each point on the surface of the bubbles, corresponding to the points of the iso-level $\phi = 0$. The resulting curvature values tell us how much the bubbles deviate from their spherical equilibrium shape, giving rise to small bumps and ripples in the surface when $\mathcal{K}^+$ is highly positive, or small dimples when $\mathcal{K}^+$ is highly negative.

From figure 3.6, we can appreciate the effect of density and viscosity on the mean curvature from a qualitative point of view. The figure shows for $We = 1.5$ (figure 3.6*a*) and $We = 3.0$ (figure 3.6*b*) four top views of the statistically-stationary configurations of the system. Bubbles are colored according to the local value of the mean curvature (blue-low; red-high). Red areas correspond to bumps and ripples of the interface (positive curvatures), while blue areas to dimples (negative curvatures).

For $We = 1.5$ (figure 3.6*a*), the effect of the density ratio can be observed by looking at the horizontal sequence of pictures (central row): we notice that moving from $\rho_r = 1$ down to $\rho_r = 0.001$ there is a slight decrease in the extension of both red and blue saturated regions, which correspond to very high and very low curvatures respectively. Therefore a reduction of the density ratio (i.e. a decrease of bubble density), leads to a smoother bubble surface, characterized by fewer ripples and dimples.

In the vertical sequence of pictures on the right column, we can appreciate the effect of viscosity. We notice that the shape of the bubbles is qualitatively unchanged increasing the viscosity from $\mu_r = 0.01$ to $\mu_r = 1$. However, from $\mu_r = 1$ to $\mu_r = 100$ the shape changes remarkably: the irregularities that characterize the bubbles surface at $\mu_r = 1$ disappear completely at $\mu_r = 100$, where the surface becomes very smooth and the bubbles shape very closely resembles the spherical shape. Thus, the action of viscosity seems opposite to the one of density in terms of local deformation of the

Die approbierte gedruckte Originalversion dieser Dissertation ist an der TU Wien Bibliothek verfügbar.
The approved original version of this doctoral thesis is available in print at TU Wien Bibliothek.
TU Bibliothek Your knowledge hub WIEN

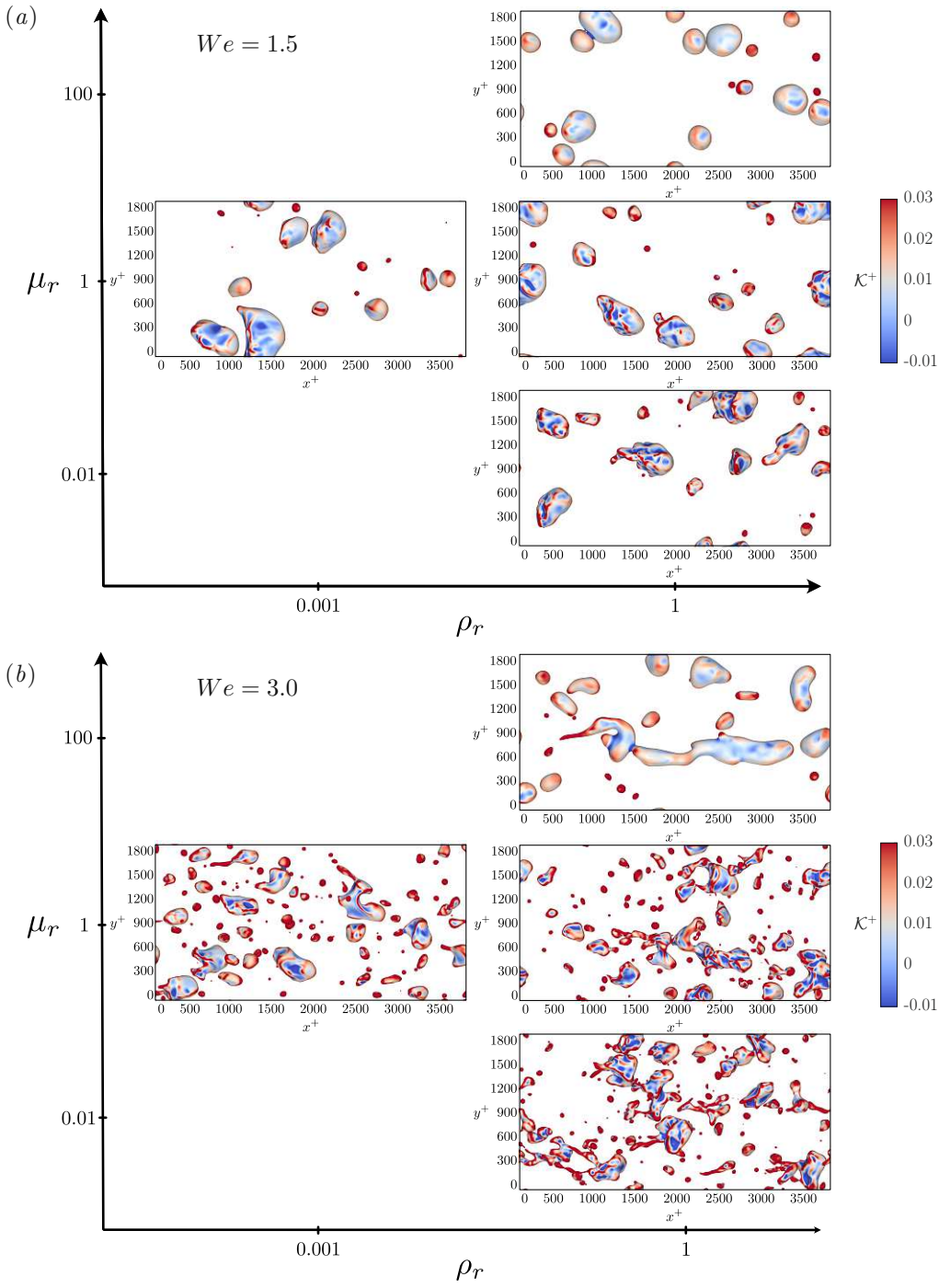

FIGURE 3.6 – Top view of the mean curvature of the bubble surface, $\mathcal{K}^+$, for four different combinations of density ratios ($\rho_r = 0.001$ and 1) and viscosity ratios ($\mu_r = 0.01, 1$ and 100) once a statistically-stationary configuration is reached ($t^+ = 4000$). Panel (a) refers to $We = 1.5$ while panel (b) to $We = 3.0$. The sub-panels are arranged in a plot using ρ_r as x-coordinate and μ_r as y-coordinate. The effect of density can be appreciated in the sequence of panels on the middle row, while that of viscosity in the right column. Bubble surface (iso-level $\phi = 0$) is colored according to the local value of the mean curvature (low-blue; high-red).

Die approbierte gedruckte Originalversion dieser Dissertation ist an der TU Wien Bibliothek verfügbar.
The approved original version of this doctoral thesis is available in print at TU Wien Bibliothek.
TU Bibliothek Your knowledge hub WIEN

bubble surface: an increase of viscosity prevents the formation of high curvatures values (in magnitude), while an increase of density promotes the formation of large interface deformations. The two opposite trends obtained increasing the density or viscosity ratios can be interpreted in terms of local Reynolds or capillary numbers (i.e. evaluated using the bubble proprieties). An increase of the density ratio leads to an increase of the local Reynolds number and as a consequence, a more irregular surface of the bubbles is obtained. In contrast, an increase of the viscosity ratio, produces a decrease of the local Reynolds number (which also corresponds to an increase of the capillary number) and a smoother surface of the bubbles is attained. Interestingly, the entity of these effects depends on the value of the ratio considered: a slight effect of the density ratio can be observed when it is decreased of three orders of magnitude (from $\rho_r = 1$ down to $\rho_r = 0.001$), as well as for the viscosity ratio when reduced by two orders of magnitude (from $\mu_r = 1$ down to $\mu_r = 0.01$), while a more noticeable difference is visible when it is increased of two orders of magnitude (from $\mu_r = 1$ up to $\mu_r = 100$). Similar considerations can be obtained from the qualitative results obtained at $We = 3.0$ (figure 3.6*b*). In this case, we can qualitatively appreciate similar effects for the density and viscosity ratios. These modifications, however, are now reflected on a much larger number of bubbles (larger Weber number).

To confirm these first qualitative observations, we compute the probability density function (PDF) of the mean curvature. Results are reported in figure 3.7 for different combinations of the density ratio, viscosity ratio, and Weber number. Left column (figure 3.7*a*,*c*,*e*) refers to $We = 1.5$, while right column (figure 3.7*b*,*d*,*f*) to $We = 3.0$.

Before analyzing each curve in detail, we can do some general observations. All curves are centered on a positive value of curvature and present an asymmetry with respect to the null value. Since positive curvatures correspond to convex surfaces and the null curvature corresponds to a flat surface, this is consistent with the fact that bubbles are in average convex, considering an outwards normal vector. Then, comparing the results shown in the left column (cases at $We = 1.5$) against those reported in the right column (cases at $We = 3.0$), we can appreciate the effect of the Weber number: for $We = 3.0$ the curves are extended on a wider range of curvature values with respect to $We = 1.5$. In particular, the curves are extended slightly towards negative values and considerably towards positive values, meaning that a higher Weber leads to a higher probability of having irregularities in the surface of the bubbles, especially bump or ripples-like irregularities. The higher probability of having large curvature values is also due to the presence of many smaller bubbles, which are intrinsically more convex (smaller radius) and closer to a spherical shape.

We study now the effects of the density ratio (figure 3.7*a*,*b*). We notice a trend for $We = 1.5$ that becomes clearer for $We = 3.0$: the cases with $\rho_r = 0.1, 0.01, 0.001$ present a lower probability of having large curvatures (in magnitude) with respect to $\rho_r = 1$. This effect is small for positive curvatures and more pronounced for negative curvatures. We can also observe that while the discrepancy between the reference case ($\rho_r = 1$) and all other cases is clear, there is almost no difference among the cases $\rho_r = 0.1, 0.01$, and 0.001. Interestingly, a similar trend was also reported in a previous work [29] that investigated the rise of bubbles in quiescent liquid. In particular, Cano-Lozano et al. [29] reported that for density ratios smaller than 0.128, a further decrease of the density ratio does not produce significant changes in the shape of the

Die approbierte gedruckte Originalversion dieser Dissertation ist an der TU Wien Bibliothek verfügbar.
The approved original version of this doctoral thesis is available in print at TU Wien Bibliothek.
TU Bibliothek Your knowledge hub WIEN

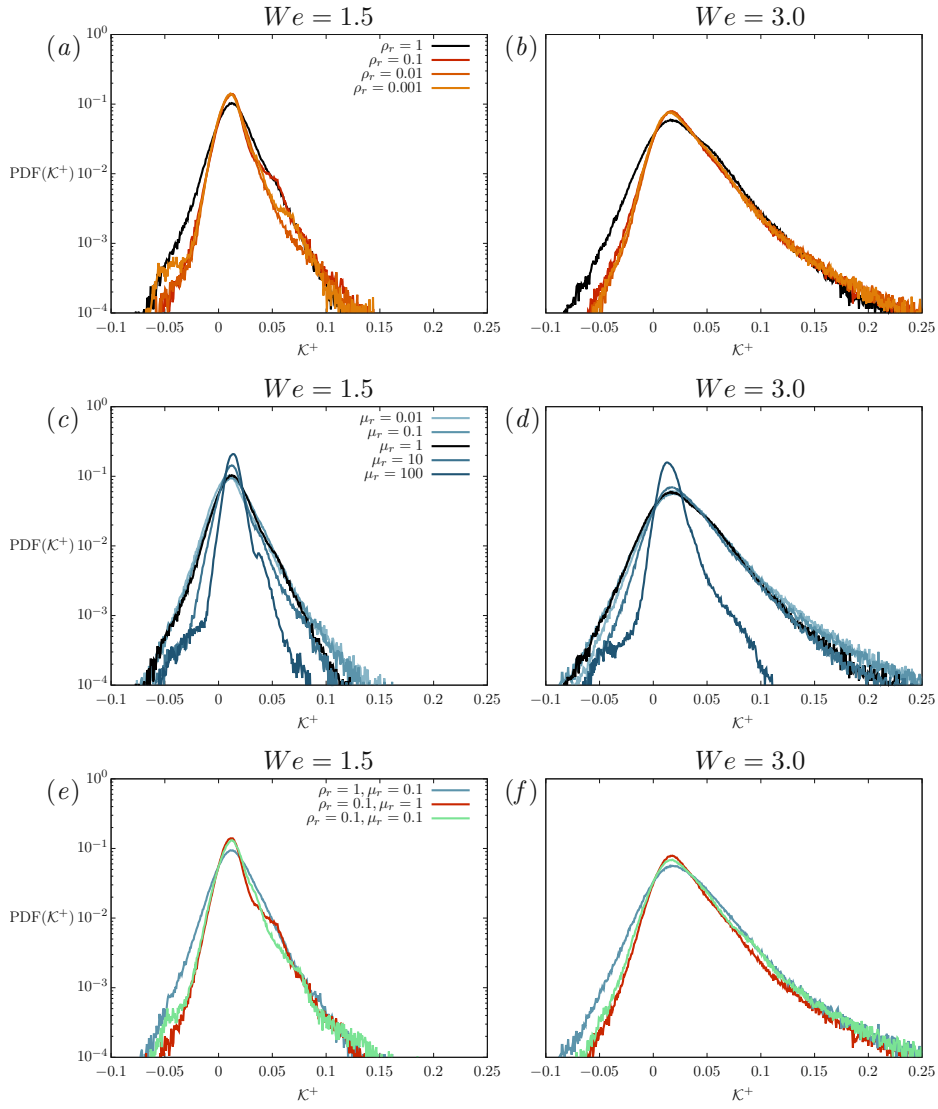

FIGURE 3.7 – Probability density function of the mean curvature, $\mathcal{K}^+$. Left column refers to $We = 1.5$, while right column to $We = 3.0$. Effect of density ratio can be appreciated on the top row for $\rho_r = 0.001, 0.01, 0.1$ and 1 (with $\mu_r = 1$). The effect of bubble viscosity can be observed in the middle row for $\mu_r = 0.01, 0.1, 1, 10$ and 100 (with $\rho_r = 1$). Finally, the combined effect of the density and viscosity ratio is shown on the bottom row for the case with $\rho_r = 0.1$, $\mu_r = 0.1$, with respect to the cases where a single effect is considered (with $\rho_r = 0.1$, $\mu_r = 1$ and $\rho_r = 1$, $\mu_r = 0.1$).

Die approbierte gedruckte Originalversion dieser Dissertation ist an der TU Wien Bibliothek verfügbar.
The approved original version of this doctoral thesis is available in print at TU Wien Bibliothek.
TU Bibliothek Your knowledge hub WIEN

bubbles. This seems to suggest that the modifications produced by the density with respect to the case with $\rho_r = 1$ (matched density case), are likely to be proportional to the density difference between the two phases (i.e. $\rho_c - \rho_d$) rather than their ratio (i.e. ρ_d/ρ_c). Further simulations, which consider super-unitary density ratios, are however required to confirm this indication. Overall, present results (figure 3.5) indicate that when sub-unitary density ratios are considered, the probability of having large curvatures values, especially negative, and very stretched bubbles decreases. In other words, when the density of the bubbles is decreased with respect to the carrier density, it becomes more difficult for turbulence fluctuations to locally deform and stretch the bubbles, and in particular, it is difficult to create dimples and concave areas. A possible physical mechanism that supports present observations is the following: when an external perturbation reaches the deformable interface of a bubble, the bubble surface is modified and the perturbation then propagates to the internal bubble fluid. As bubble density is reduced, however, the propagation of this perturbation to the bubble fluid and thus to the rest of the bubble interface becomes less effective. Indeed, the inertia of the perturbation is modulated by the smaller bubble density and thus the magnitude of the inertial forces is reduced. As a result, viscous and surface tension forces increase their relative importance with respect to inertial forces, and the resulting bubble deformation is reduced. This behaviour can be also justified considering the dispersed phase Reynolds number, i.e. the Reynolds number evaluated considering the dispersed phase density. As bubble density is reduced, so does the dispersed phase Reynolds number and the bubbles become less deformable and distorted, as can be also graphically appreciated from figure 3.2 comparing the case $\rho_r = 0.001$ (orange bubbles) against the case $\rho_r = 1.000$ (white bubbles).

To evaluate the influence of the viscosity, we consider figure 3.7*c,d*. A trend can be distinguished for both the Weber numbers: the PDFs become narrower as the viscosity increases. More specifically, the largest effect can be seen for $\mu_r = 100$, where the range of possible curvatures is significantly reduced. The shrinkage of the pdf is less but still evident for $\mu_r = 10$, and it becomes almost negligible for $\mu_r = 0.1$ and $\mu_r = 0.01$. Unlike density, the impact of viscosity is important for $\mu_r = 100$ and $\mu_r = 10$, while it becomes less important for $\mu_r = 0.1$ and $\mu_r = 0.01$. Indeed, for these two latter cases, no significant modifications can be appreciated from both Weber numbers.

Finally, the combined effects of the density and viscosity ratio can be evaluated from figure 3.7*e,f*. Interestingly, we observe that when both density ratio and viscosity ratios are decreased, the resulting PDF of the mean curvature lies in between the case $\rho_r = 0.1$ (and matched viscosity) and $\mu_r = 0.1$ (and matched density). This intermediate behaviour can be traced back to the two opposite actions of density and viscosity on the mean curvature of the surface of the bubbles: while a decrease of the bubble density (i.e. of the density ratio) makes the bubbles surface more rigid and thus smoother, when bubble viscosity is decreased the bubbles become more deformable and ripples or dimples can be more easily formed on the interface. Thus, when we combine these two effects, these actions balance out and we obtain an intermediate trend. This result is already visible for $We = 1.5$ and becomes clearer for $We = 3.0$ where, thanks to the higher number of bubbles, a smoother statistic is obtained.

Die approbierte gedruckte Originalversion dieser Dissertation ist an der TU Wien Bibliothek verfügbar.
The approved original version of this doctoral thesis is available in print at TU Wien Bibliothek.
TU Bibliothek Your knowledge hub WIEN

3.2.3 Flow modifications

Mean velocity profiles

Once detailed the evolution of the dispersed phase topology, its modifications and the deformation and curvature of the bubbles, we move to analyze the flow modifications produced by the bubbles. We start by analyzing the macroscopic behaviour of the multiphase mixture, in terms of flow-rate and mean flow statistics. In particular, we investigate the wall-normal behaviour of the mean velocity profiles of the multiphase flow, and we compare them with the single-phase flow statistics at the same $Re_\tau = 300$. Indeed, we aim at understanding whether the injection of bubbles in a turbulent flow induces modifications to the mean velocity profile, especially when density or viscosity contrasts are present between the two phases. This aspect is widely studied and a common question that persists in the field concerns the capability of bubbles in generating drag reduction [96, 31, 157, 160, 139, 28].
Figure 3.8 shows the wall-normal behaviour of the mean velocity profiles, computed by averaging the streamwise velocity along the streamwise and spanwise directions in the entire domain (both dispersed and carrier phase). The results are illustrated for all combinations of density and viscosity ratios considered, following the same arrangement of the previously presented statistics. In addition, the velocity profile relative to the single-phase case is shown with a black dashed line, and the classical law of the wall, $u^+ = z^+$ and $u^+ = (1/\kappa)\ln z^+ + 5.2$ [125], is reported as a reference (with $\kappa = 0.41$ the Von Kármán constant [161]). We observe that in all the plots the velocity profiles perfectly collapse on each other in the vicinity of the wall, while tiny deviations can be observed in the central part of the channel, where most bubbles are located. In particular, in the core region of the channel, no differences can be appreciated varying the density and viscosity ratios. However, all multiphase cases are characterized by a slightly greater velocity with respect to the single-phase case.
As in our simulations a constant mean pressure gradient is used to drive the flow, the observed flow-rate enhancement corresponds to a slight drag reduction. The drag reduction we observe is rather low in all the simulated cases (roughly 1 to 2%), and current results suggest that the presence of density and viscosity contrasts among the phases does not visibly impact it. These results are in agreement with previous works [101, 28], which found that drag significantly depends on the bubble size. Specifically, they observe that large and deformable bubbles (obtained allowing bubbles to coalesce) migrate towards the central part of the channel and do not influence the drag significantly [96, 98, 99, 97]. By opposite, smaller bubbles (obtained not allowing bubbles to coalesce) move towards the near-wall region and lead to an increase of the drag [96, 98, 99, 97]. To support this argument, we can consider figure 4.9, which shows the scatter plot of the wall-normal location of each bubble over its equivalent diameter. Panel *a* refers to $We = 1.5$ while panel *b* to $We = 3.0$. The bottom and top walls are located at $z^+ = 0$ *w.u.* and $z^+ = 600$ *w.u.*. Two black dashed lines identify the critical condition for which the upper (or lower) part of the bubble interface intercepts the top (or bottom) wall. From a mathematical point of view, this condition can be identified imposing:

$$z_b^+ = d_{eq}^+/2\,, \tag{3.6}$$

where z_b^+ is the distance of the center of the mass of the bubble from the closer wall,

Die approbierte gedruckte Originalversion dieser Dissertation ist an der TU Wien Bibliothek verfügbar.
The approved original version of this doctoral thesis is available in print at TU Wien Bibliothek.
TU Bibliothek Your knowledge hub WIEN

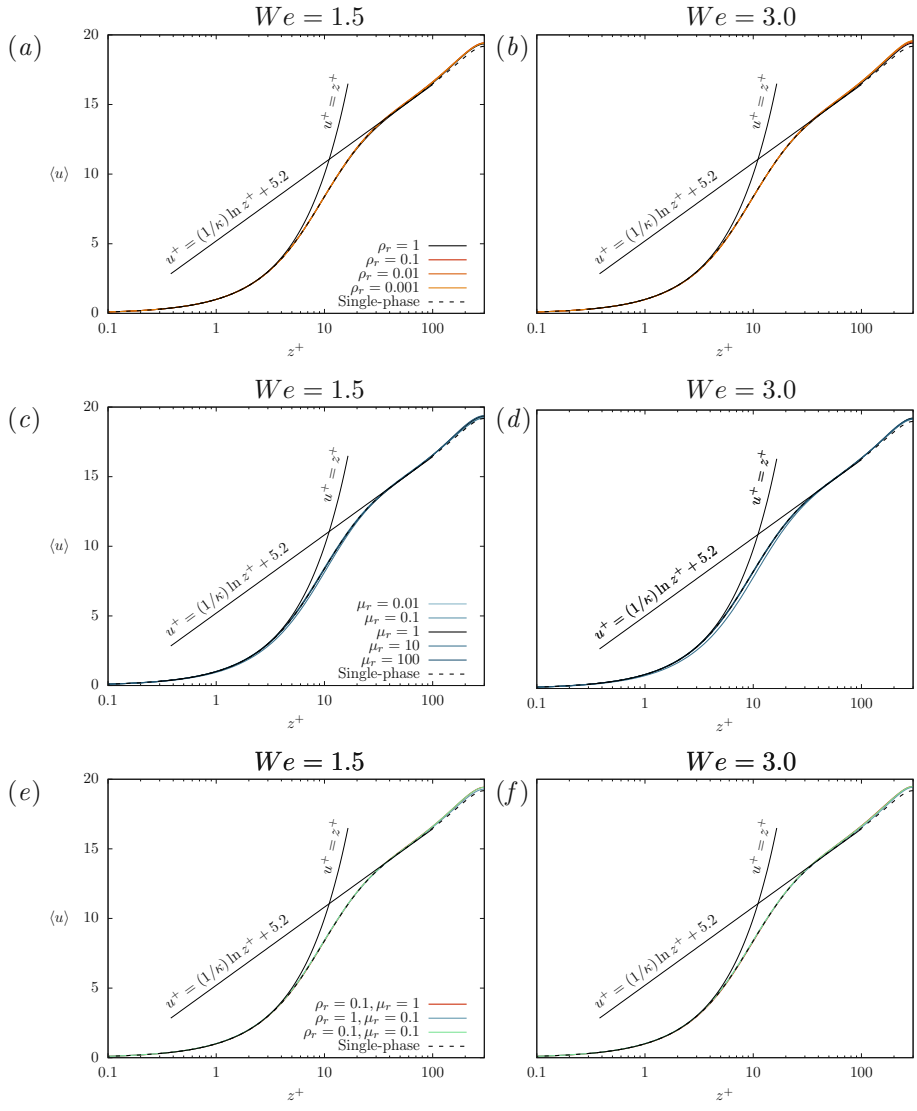

FIGURE 3.8 – Wall-normal behaviour of the streamwise mean velocity profiles. Left column refers to $We = 1.5$, while the right column to $We = 3.0$. Density ratios effects are shown on the top row for $\rho_r = 0.001, 0.01, 0.1, 1$. Viscosity ratio effects are shown on the middle row for $\mu_r = 0.01, 0.1, 1, 10, 100$. Finally, the combined effect of the density and viscosity ratios is shown on the bottom row for the case $\rho_r = 0.1$ and $\mu_r = 0.1$, with respect to the cases where only one effect is considered. As a reference, the classical law of the wall, $u^+ = z^+$ and $u^+ = (1/k)\log z^+ + 5$ (with $k = 0.41$ the von Kármán constant) is also reported with a dashed line. For all cases, with respect to single-phase, we observe a minor increase of the mean velocity.

Die approbierte gedruckte Originalversion dieser Dissertation ist an der TU Wien Bibliothek verfügbar.
The approved original version of this doctoral thesis is available in print at TU Wien Bibliothek.
TU Bibliothek Your knowledge hub WIEN

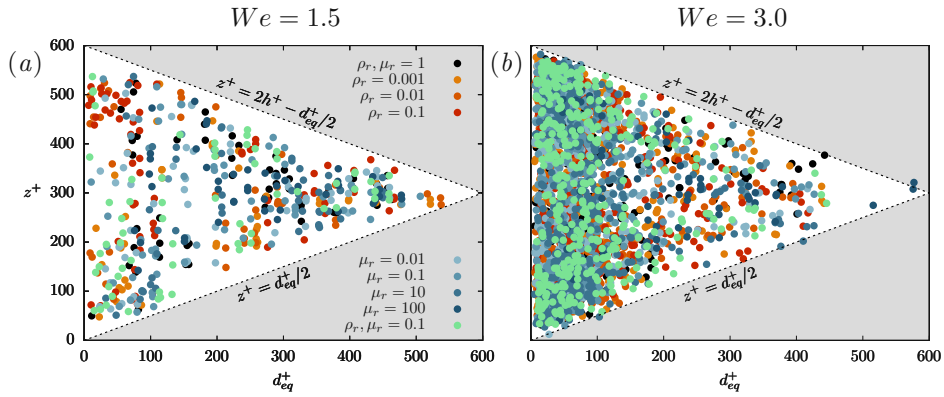

FIGURE 3.9 – Scatter plot of the wall-normal location of each bubble over its size for the different cases considered. The two black dashed lines identify the condition for which the interface of the bubble intercepts the closer wall in the hypothesis of a perfectly spherical bubble. Smaller bubbles tend to disperse along the entire channel height can get rather close to one of the two walls while larger bubbles tend to accumulate at the center of the channel.

which can be computed as follows:

$$z_b^+ = \min(z_i^+, 2h^+ - z_i^+)\,, \tag{3.7}$$

where z_i^+ is the wall-normal location of the i-th bubble and $h^+ = 300$ $w.u.$ is the channel half-height in wall units. Hence, the equations that identify these conditions are:

$$z^+ = d_{eq}^+/2\,, \qquad z^+ = 2h^+ - d_{eq}^+/2\,. \tag{3.8}$$

Analyzing the dispersion of the bubbles along the wall-normal direction, we can confirm previous intuitions: smaller bubbles tend to disperse along the entire height of the channel and can get rather close to the two walls while, by opposite, larger bubbles tend to accumulate at the center of the channel and stay farther away from the two walls. It is worth pointing that despite a few points are located above (or below) the two black dashed lines (i.e. in the gray region), no collisions with the walls are detected. Instead, these points represent bubbles elongated along the streamwise or spanwise directions and thus with a larger d_{eq}^+ with respect to the actual wall-normal size. Overall, the results presented in figure 3.8 corroborated by those reported in figure 4.9 seem to confirm the idea that bubble deformability is a crucial parameter for obtaining drag reduction [143, 98, 31, 160, 28]. Indeed, bubble deformability plays a central role in determining the preferential distribution of the bubbles [98, 100], which is directly linked to drag reduction [160, 139].

Turbulent Kinetic Energy (TKE) of bubbles

After having analyzed the flow field in terms of mean velocity, we focus on the turbulence behaviour inside the bubbles. The characterization of the flow inside the bubbles is of paramount importance in many applications. Indeed, internal circulation controls the transport of heat, mass, momentum and chemical species through the interface

Die approbierte gedruckte Originalversion dieser Dissertation ist an der TU Wien Bibliothek verfügbar.
The approved original version of this doctoral thesis is available in print at TU Wien Bibliothek.
TU Bibliothek Your knowledge hub WIEN

[6, 61], the motion and deformation of the bubbles [93, 109] and particle removal efficiency in scrubbing process [59, 65]. To characterize the mixing and flow behaviour in the dispersed phase, we consider the turbulent kinetic energy (TKE) inside the bubbles. Since the shear Reynolds is set in the turbulent channel flow based on the carrier phase properties, namely ρ_c and μ_c, when a density and viscosity ratio is imposed, modifications of the flow field are expected to occur inside the dispersed phase, where density and viscosity are different (i.e. ρ_d and μ_d). As the magnitude of inertial and viscous forces inside the bubbles differs from the one in the carrier fluid, the turbulence characteristics must also change inside the bubbles, where a local Reynolds number could be evaluated using the dispersed phase properties and the bubble size.
To give a first qualitative idea of these modifications, we can consider the specific turbulent kinetic energy, TKE, whose definition is here recalled:

$$\mathrm{TKE} = \frac{\rho}{\rho_c}\frac{(u'^2 + v'^2 + w'^2)}{2}, \tag{3.9}$$

where ρ is the local density (ρ_d in the bubbles and ρ_c in the carrier phase). Figure 3.10 shows the specific turbulent kinetic energy for two different simulations: panel (a) refers to the case with $\rho_r = 0.01$ and matched viscosity and panel (b) to the case with $\mu_r = 0.01$ and matched density. Both panels refer to the higher Weber number analyzed ($We = 3.0$) and to the time instant $t^+ = 4000$, when for both cases a statistically-stationary configuration is attained. The two snapshots illustrate with a white-black scale the contour map of specific TKE on an $x^+ - y^+$ plane located at the channel center ($z^+ = 0$). The interface of the bubbles is marked with a white thin line. We notice that the flow structures in the carrier phase are qualitatively similar in the two pictures, while inside the bubbles the contour maps of specific TKE look very different and for $\rho_r = 0.01$ and $\mu_r = 1$ (panel a), low values of specific TKE inside the bubbles are observed. In evaluating the results presented in panel a, however, it is important to make a clarification: although the energy content of the bubbles is rather low, velocity fluctuations are still present inside the bubbles. Indeed, the low values of specific TKE in the bubbles obtained for the case $\rho_r = 0.01$ and $\mu_r = 1$ are due to the low density that characterizes the bubbles: the prefactor ρ/ρ_c present in the definition of specific TKE reduces the values obtained inside the bubbles. Shifting our focus to the case $\mu_r = 0.01$ and $\rho_r = 1$ (panel b), we can appreciate here the presence of many vortical structures characterized by an energy content similar to that of the carrier phase. Interestingly, the characteristic length scale of these turbulence structures is much smaller than that of the carrier phase. This observation can be traced back to the smaller viscosity of the dispersed phase that results in a larger local Reynolds number, as also observed in other multiphase flow instances [133, 134].
To quantify these qualitative observations, we compute the mean value of the specific turbulent kinetic energy inside the bubbles for all simulated cases, except for the combined case, and we collect the results in figure 3.11. To better evaluate the contribution of density and velocity fluctuations, the specific turbulent kinetic energy is shown in panel a (according to equation 3.9), while the turbulent kinetic energy is shown in panel b (i.e. the specific TKE is reported normalized by the local density contribution ρ/ρ_c). The mean values of specific TKE and TKE are reported as a function of the density ratio (scale on the bottom part of the plot), viscosity ratio (scale on the top

Die approbierte gedruckte Originalversion dieser Dissertation ist an der TU Wien Bibliothek verfügbar.
The approved original version of this doctoral thesis is available in print at TU Wien Bibliothek.
TU Bibliothek Your knowledge hub WIEN

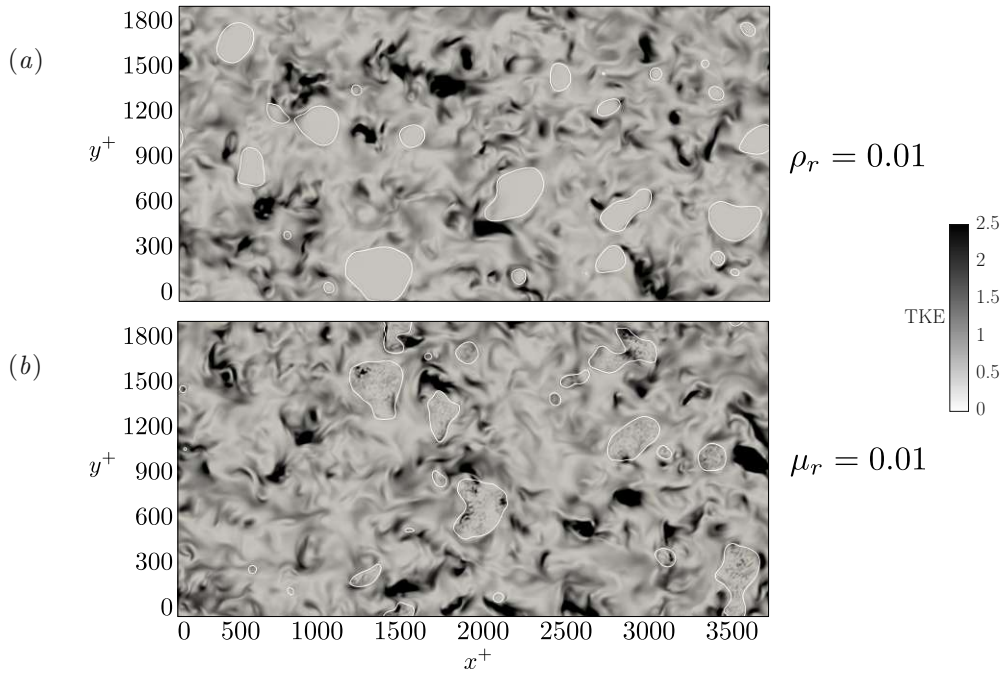

FIGURE 3.10 – Contour map of the specific turbulent kinetic energy in a $x^+ - y^+$ plane located at the channel center ($z^+ = 0$). Panel (a) refers to the case $\rho_r = 0.01$ and $\mu_r = 1$ while panel (b) refers to the case $\rho_r = 1$ and $\mu_r = 0.01$. Both panels refer to the lower surface tension case ($We = 3.0$) and to the time instant $t^+ = 4000$ (statistically-steady configuration). The interface of the bubbles is highlighted with a white line. For $\rho_r = 0.01$, bubbles and characterized by a low and uniform value of the specific TKE while, for $\mu_r = 0.01$, the specific TKE map is non-uniform and characterized by small scales fluctuations.

part of the plot), and Weber number (full circles for $We = 1.5$ and empty circles for $We = 3.0$). We start by analyzing the effects of the density and viscosity ratios shown in panel *a*. Two opposite trends can be observed: as the viscosity ratio increases, the mean value of specific TKE inside the bubbles decreases of about one order of magnitude while, by opposite, increasing the density ratio, the mean value of specific TKE inside the bubbles rapidly increases of about four orders of magnitude. This behaviour reflects the modifications of the inertial and viscous forces inside the bubbles produced by the different dispersed phase density and viscosity. As the viscosity ratio is increased from $\mu_r = 0.01$ up to $\mu_r = 100$ (from left to right), viscous forces become dominant over inertial forces and thus the local Reynolds number decreases. As a result, for low viscosity ratios, small turbulent structures can be observed inside the bubbles, characterized by significative turbulent kinetic energy levels, while for viscosity ratios larger than unity turbulence structures cannot be sustained inside the bubbles (larger viscous dissipation) and bubbles are characterized by a low level of specific turbulent kinetic energy. A similar trend, albeit in a slightly different simulation setup, was reported by Cano-Lozano et al. [29], that investigated the rise of bubbles in still liquid and observed a reduction of the velocity gradients for increasing

Die approbierte gedruckte Originalversion dieser Dissertation ist an der TU Wien Bibliothek verfügbar.
The approved original version of this doctoral thesis is available in print at TU Wien Bibliothek.
TU Bibliothek Your knowledge hub WIEN

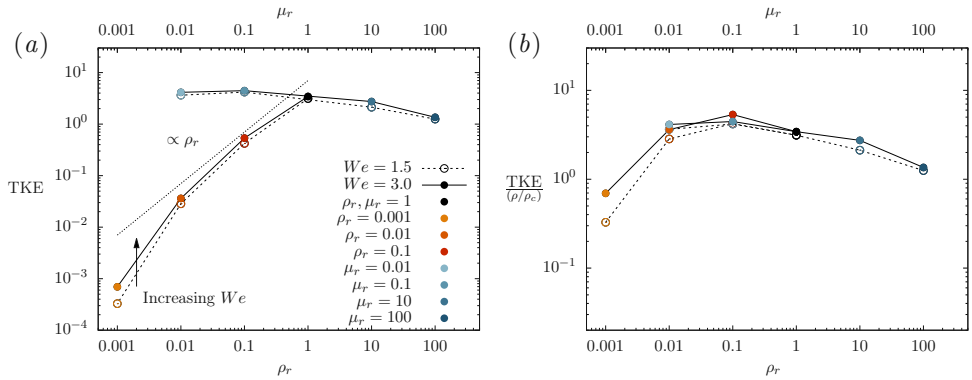

FIGURE 3.11 – Mean value of the turbulent kinetic energy (TKE) inside the bubbles. In panel *a*, TKE is evaluated using the complete definition of specific TKE (i.e. including the prefactor ρ/ρ_c) while, in panel *b*, TKE is evaluated considering only the velocity contribution (i.e. not considering the prefactor ρ/ρ_c). For both panels, a dashed line ($We = 1.5$) and a continuous line ($We = 3.0$) are used to show the behaviour of TKE as the density or viscosity ratios are changed. Each value of TKE is marked with a circle (empty for $We = 1.5$ and filled for $We = 3.0$), with a red-color scale for the non-matched density cases and a blue-color scale for the non-matched viscosity cases, while the black color is used for the reference case.

values of the viscosity ratio. On the other hand, increasing the density ratio from $\rho_r = 0.001$ up to $\rho_r = 1$, inertial forces become dominant over viscous forces, the local Reynolds number increases and the bubbles result to be characterized by higher specific turbulent kinetic energy. Interestingly, we observe a much stronger action of the density ratio on the mean value of the bubbles specific TKE. Indeed, the specific turbulent kinetic energy directly depends on the bubble density and, as we can see from panel *a*, present results roughly follow the ρ_r scaling law reported with a dotted line. However, it is worthwhile observing that when the smallest density ratio is considered ($\rho_r = 0.001$), results start to deviate from the ρ_r scaling law: as the density ratio is reduced, we observe a reduction in the magnitude of the velocity fluctuations of about one order of magnitude. This deviation can be better appreciated in panel *b*, where the specific TKE values are reported normalized by the prefactor ρ/ρ_c, so that the contribution from velocity fluctuations alone can be better appreciated. The magnitude of velocity fluctuations is roughly constant when considering different density ratios, exception made for the lowest density ratio, $\rho_r = 0.001$, thus indicating that the specific TKE scales with the density ratio.

Finally, the effect of the Weber number is considered: we observe that increasing the Weber number, thus decreasing the surface tension, the TKE is slightly increased for all the cases. This trend can be attributed to the larger transfer of momentum that occurs when surface tension forces are weaker: as the interface becomes more deformable, the modulation effect of the interface becomes weaker and energy and momentum can be more easily exchanged between the phases. When the surface tension is reduced, in fact, the bubbles become more deformable and reasonably they are more likely to contain a greater amount of TKE.

Die approbierte gedruckte Originalversion dieser Dissertation ist an der TU Wien Bibliothek verfügbar.
The approved original version of this doctoral thesis is available in print at TU Wien Bibliothek.
TU Bibliothek Your knowledge hub WIEN

3.3 Conclusions

In this work, we studied the behaviour of bubbles in a turbulent channel flow for different values of the density ratio, viscosity ratio, and Weber number. The investigation is based on direct numerical simulation of turbulence coupled with a phase-field method. First, we investigated the topology of the dispersed phase and its modifications. We found that the number of bubbles present in the channel is strongly influenced by the surface tension value (i.e. by the Weber number), in accordance with the results of previous studies [89, 132, 145]. Besides, we observe that an increase of bubble viscosity with respect to the carrier (i.e. an increase of the viscosity ratio) has an important stabilizing role and leads to a remarkable increase of the maximum bubble stable diameter and thus to a decrease of the number of bubbles. By opposite, a reduction of the bubble density (i.e. a reduction of the density ratio), does not remarkably affect the dispersed phase topology. Similar findings are obtained from the analysis of the coalescence and breakage rates: an increase of bubble viscosity or surface tension (i.e. a decrease of the Weber number) leads to a reduction of the breakage and coalescence rates. In contrast, a modification of the density ratio has a marginal effect on the behaviour of the breakage and coalescence rates. Secondly, we studied the surface stretching and curvature of the bubbles. We observed that these indicators are influenced by all three parameters investigated. In particular, larger viscosity ratios or lower density ratios or Weber numbers hinder the stretching of the bubbles and as a result the overall amount of interfacial area obtained is lower (with respect to the reference matched density and viscosity cases). These observations are also reflected in the probability density function of the mean curvature: an increase of bubble viscosity, a decrease of bubble density or a decrease of the Weber number hinder the formation of ripples and dimples on the surface of the bubbles and thus high curvature values are less likely to be found. Thirdly, we evaluated the flow modifications produced by the swarm of bubbles in the background turbulent flow and in the dispersed phase. From a macroscopic point of view, no significant modifications are observed in the wall-normal behaviour of the mean velocity profiles and only a minor increase of the flow-rate is observed for all bubbles-laden cases with respect to a single-phase flow, in accordance with previous results [89, 132, 145]. Finally, as bubbles internal circulation play a key role in controlling the transport of heat, mass, momentum through the interface [6, 61], we characterized the mixing in the bubbles by studying the turbulent kinetic energy of the bubbles. We observe a clear action of density and viscosity in modulating the turbulent kinetic energy of the bubbles. In particular, a decrease of the bubble density or an increase of the bubble viscosity lead to a remarkable decrease of the turbulent kinetic energy levels in the bubbles.

Die approbierte gedruckte Originalversion dieser Dissertation ist an der TU Wien Bibliothek verfügbar.
The approved original version of this doctoral thesis is available in print at TU Wien Bibliothek.
TU Bibliothek Your knowledge hub WIEN

Die approbierte gedruckte Originalversion dieser Dissertation ist an der TU Wien Bibliothek verfügbar.
The approved original version of this doctoral thesis is available in print at TU Wien Bibliothek.

4

Heat transfer in drop-laden turbulence

Reproduced in part from:
F. Mangani, A. Roccon, F. Zonta and A. Soldati, *Heat transfer in drop-laden turbulence, Journal of Fluid Mechanics*, 978, A12 (2024).

In turbulent dispersed multiphase flows, drops or bubbles that are deformable and larger than the smallest turbulent scales are characterized by an internal circulation and secondary flow. The characteristics and the developement of such internal flow depend on many different factors, such as the drop/bubble size, the forcing produced by the surrounding turbulent flow and the drop/bubble thermophysical properties, as discussed in section 3.2.3 of the previous chapter. This internal flow plays a crucial role in the mixing of scalar quantities, like heat or mass, whose distribution can be as much inhomogeneous and non-uniform as the internal turbulence is. The assumption of a uniformly distributed scalar inside the drops/bubbles, which is often used in simple analytical models, can be therefore a substantial approximation, leading to inaccurate predictions of the scalar motion and transfer rate between the fluids. In this chapter, the mixing of a scalar in a turbulent two-phase flow will be investigated, with particular attention at the scalar transfer between the phases.

Transport of passive and active scalars in turbulent dispersed multiphase flows is very important in many industrial processes and natural phenomena, from vaporization of atomized fuel jets [62, 5, 56, 19], to rain formation and atmosphere-ocean heat/mass exchanges [48, 42] or even to the uptake of nutrients and other biochemicals by cells in complex flows [2, 104]. In turbulent single-phase flows, the mixing of active or passive scalars has been widely investigated in the last decades using experiments and simulations [3, 82, 83, 123, 170, 171, 172]. Only recently, instead, these phenomena have been included in the study of turbulent multiphase flows. Indeed, when multiphase flows are considered the situation becomes much more challenging [58, 115], due to the presence of interfaces that dynamically move and deform in time and space according to the flow conditions and that clearly alter or modulate heat and species transport and mixing[41, 63, 95, 120, 135]. In this context, previous works mostly focused on the heat/mass transfer from/to isolated drops and bubbles using analytical [18, 92, 12], numerical [16, 53, 68, 39, 118, 52] and experimental techniques [116, 73, 166, 14, 107].

When swarms of drops/bubbles are considered, the number of available investigations is more limited. For very small drops/bubbles, numerical investigations usually rely on the Lagrangian approach, in which drops/bubbles are assumed to have sub-Kolmogorov size and are treated as material points [88, 110, 34, 162, 163]. When larger drops/bubbles are considered (i.e. larger than the Kolmogorov scale), the problem becomes more complex, since the interface shape and deformation play a crucial role. Not surprisingly, remarkable works in this context have appeared only lately, both for the case of passive scalar transport and for the case of active scalars/phase change [111, 46, 138, 22, 70]. Relevant to the present work is the observation done by [46] and [138], and also confirmed by the experiments of [111], that the Sherwood number (i.e. dimensionless mass transfer coefficient) measured during drop evaporation in turbulence is larger compared to that obtained from widely-used correlations [130, 55, 13].

This work is focused on the numerical simulation of the heat transfer process in a drop-laden turbulent channel flow, particularly at the role of the Prandtl number Pr, i.e. the ratio between momentum and thermal diffusivity, in the process. Compared to single-phase turbulence, where the range of scales that must be resolved to perform a direct numerical simulation (DNS) is purely dictated by the smallest scales of turbulence (Kolmogorov scale), when the mixing of scalars in multiphase turbulence is analyzed, two further additional scales come into the picture. The first one is the Batchelor scale [9, 10], which determines the smallest scale of the temperature/concentration field. The second important scale is the Kolmogorov-Hinze scale [85, 72], and is linked to the multiphase nature of the flow. This scale can be used, perhaps with some limitations [129], to determine the critical size of a drop/bubble that will not undergo breakage in turbulence. These two scales – and their corresponding ratio to the Kolmogorov scale, i.e. the smallest length scale of the turbulent flow field – control the system dynamics and define the minimal grid requirements that must be satisfied to perform a DNS of scalar mixing in multiphase turbulence (keeping always in mind that performing a simulation that resolves the interface dynamics down to the molecular scale is at present almost unfeasible). In this context, the major constraint is usually posed by the Batchelor scale, which becomes smaller than the Kolmogorov length scale when Prandtl numbers larger than unity are considered. Overall, the wide range of scales involved in the process makes simulations of scalar mixing in multiphase turbulence a challenging task and limits the space parameters that can be explored by means of DNS. Our simulations are initialized by injecting a swarm of large and deformable drops (initially warmer) inside a turbulent channel flow (initially colder). The system is described by coupling the DNS of turbulent heat transfer with a phase-field method, employed to describe the drops topology [169, 113]. We simulate realistic values of the Prandtl number up to $Pr = 8$, similar to those obtained in liquid-liquid systems. We remark here that simulations of mass transfer problems in wall-bounded flow configurations, where the typical Schmidt number Sc (i.e. the mass transfer counterpart of Pr) is $\mathcal{O}(10^2 \sim 10^3)$, e.g. $Sc \simeq 600$ for CO_2 in freshwater [164], are currently out of reach even using the most advanced computing. Indeed, the resulting Batchelor scale would be at least one order of magnitude smaller, thus requiring grid resolutions comparable or larger than those employed for state-of-the-art single-phase DNS [91, 124] but with a much larger computational cost as the systems of equations

Die approbierte gedruckte Originalversion dieser Dissertation ist an der TU Wien Bibliothek verfügbar.
The approved original version of this doctoral thesis is available in print at TU Wien Bibliothek.
TU Bibliothek Your knowledge hub WIEN

to be solved is more complex and restrictive (also from the temporal discretization point of view).
The present study has three main objectives. First, we want to investigate the macroscopic dynamic of the drops and of the heat transfer process by analyzing the drop size distribution and the mean temperature behaviour of the two phases over time. Second, we want to characterize the influence of the Prandtl number, i.e. of the microscopic flow properties, on the macroscopic flow properties (mean temperature, heat transfer coefficient) and, building on top of the numerical results, we want to develop a physically-based model to explain the observed results. Third, we want to study the influence of the Prandtl number and drop size on the temperature distribution inside the drops, so to evaluate the corresponding flow mixing/ homogenization.
The chapter is organized as follows. In section 4.1 the simulation setup is presented. Then in section 4.2, the simulation results, in terms of drop size distribution and mean temperature of the two phases and heat transfer coefficient are carefully characterized and discussed. A simplified model is also developed to explain the observed results. The temperature distribution inside the drops is then evaluated at different Prandtl numbers and drop sizes. Finally, conclusions are presented in 4.3.

4.1 Simulation setup

The turbulent channel flow, driven by an imposed constant pressure gradient in the streamwise direction, has a shear Reynolds number $Re_\tau = 300$. The computational domain has dimensions $L_x \times L_y \times L_z = 4\pi h \times 2\pi h \times 2h$, which corresponds to $L_x^+ \times L_y^+ \times L_z^+ = 3770 \times 1885 \times 600$ wall units.
The value of the Weber number is kept constant and is equal to $We = 3.00$, so to be representative of liquid/liquid mixtures [151]. To study the influence of the Prandtl number Pr on the heat transfer process, we consider four different values of Pr: $Pr = 1$, $Pr = 2$, $Pr = 4$ and $Pr = 8$. These values cover a wide range of real-case scenarios: from low-Prandtl number fluids to water-toluene mixtures. A single-phase flow simulation is also performed as a reference case, and to provide initial velocity fields for the multiphase simulations.
As the characteristic length scales of the flow and temperature fields, represented by the Kolmogorov scale, η_k^+, and the Batchelor scale, η_θ^+, are different when non-unitary Prandtl numbers are employed (being these two quantities linked by the following relation $\eta_\theta^+ = \eta_k^+/\sqrt{Pr}$), a dual grid approach is employed to reduce the computational cost of the simulations and, at the same time, to fulfil the DNS requirements. In particular, when super-unitary Prandtl numbers are simulated, a finer grid is used to resolve the energy equation. Spectral interpolation is used to upscale/downscale the fields from the coarse to the refined grid and *vice versa* when required (e.g. upscaling of the velocity field to compute the advection terms in the energy equation).
The grid resolution used to resolve the continuity, Navier-Stokes and Cahn-Hilliard equations is equal to $N_x \times N_y \times N_z = 1024 \times 512 \times 513$ for all the cases considered in this work. For the energy equation, the same grid used for the flow field and phase field is employed at the lower Prandtl numbers ($Pr = 1$ and $Pr = 2$), while a more refined grid, with $N_x \times N_y \times N_z = 2048 \times 1024 \times 513$ points, is used when the larger Prandtl numbers are considered ($Pr = 4$ and $Pr = 8$). The computational grid

Die approbierte gedruckte Originalversion dieser Dissertation ist an der TU Wien Bibliothek verfügbar.
The approved original version of this doctoral thesis is available in print at TU Wien Bibliothek.
TU Bibliothek Your knowledge hub WIEN

Case	Re_τ	We	Pr	$N_x \times N_y \times N_z$ (NS+CH)	$N_x \times N_y \times N_z$ (Energy)
SP	300	-	-	$512 \times 256 \times 257$	-
DL1	300	3.0	1.0	$1024 \times 512 \times 513$	$1024 \times 512 \times 513$
DL2	300	3.0	2.0	$1024 \times 512 \times 513$	$1024 \times 512 \times 513$
DL3	300	3.0	4.0	$1024 \times 512 \times 513$	$2048 \times 1024 \times 1025$
DL4	300	3.0	8.0	$1024 \times 512 \times 513$	$2048 \times 1024 \times 1025$

TABLE 4.1 – Overview of the simulation parameters. For a fixed shear Reynolds number $Re_\tau = 300$ and Weber number $We = 3$, we consider a single-phase flow case and four non-isothermal drop-laden flows characterized by different Prandtl numbers: from $Pr = 1$ to $Pr = 8$. The grid resolution is modified accordingly so as to satisfy DNS requirements.

has uniform spacing in the homogeneous directions, while Chebyshev-Gauss-Lobatto points are used in the wall-normal direction. We refer the reader to table 4.1 for an overview of the main physical and computational parameters of the simulations. For the employed grid resolution, the Cahn number is set to $Ch = 0.01$ while, to achieve convergence to the sharp interface limit, the corresponding phase field Péclet number is $Pe_\phi = 1/Ch = 100$.

All simulations are initialized by releasing a regular array of 256 spherical drops with diameter $d = 0.4h$ (corresponding to $d^+ = 120$ *w.u.*) inside a fully-developed turbulent flow field (obtained from the preliminary single-phase simulation). To ensure the independence of the results from the initial flow field condition, each case is initialized with a slightly different flow field realization. Naturally, the fields are equivalent in terms of statistics as they are all obtained from a statistically steady turbulent channel flow. The volume fraction of the drops is $\Phi = V_d/(V_c + V_d) = 5.4\%$, with V_d and V_c the volume of the drops and carrier fluid, respectively.

The initial condition for the temperature field is such that all drops are initially warm (initial temperature $\theta_{d,0} = 1$), while the carrier fluid is initially cold (initial temperature $\theta_{c,0} = 0$). To avoid numerical instabilities that might arise from a discontinuous temperature field, the transition between drops and carrier fluid is initially smoothed using a hyperbolic tangent kernel. Figure 4.1 (which is an instantaneous snapshot captured at $t^+ = 1000$, for $Pr = 1$) shows a volume rendering of the temperature field (blue-cold, red-hot), inside which deformable drops (whose interface, iso-level $\phi = 0$, is shown in white) are transported.

4.2 Results

Results obtained from the numerical simulations will be first discussed from a qualitative viewpoint, by looking at instantaneous flow and drops visualizations, and then analyzed from a more quantitative viewpoint, by looking at the drop size distribution (DSD), and at the effect of the Prandtl number Pr on the average drops and fluid temperature. To explain the numerical results, and to offer a possible parametrization of the heat transfer process in drop-laden flows, we will also develop a simplified phenomenological model of the system. Finally, we will characterize the temperature distribution inside the drops, elucidating the effects of Pr and of the drop size on

Die approbierte gedruckte Originalversion dieser Dissertation ist an der TU Wien Bibliothek verfügbar.
The approved original version of this doctoral thesis is available in print at TU Wien Bibliothek.
TU Bibliothek Your knowledge hub WIEN

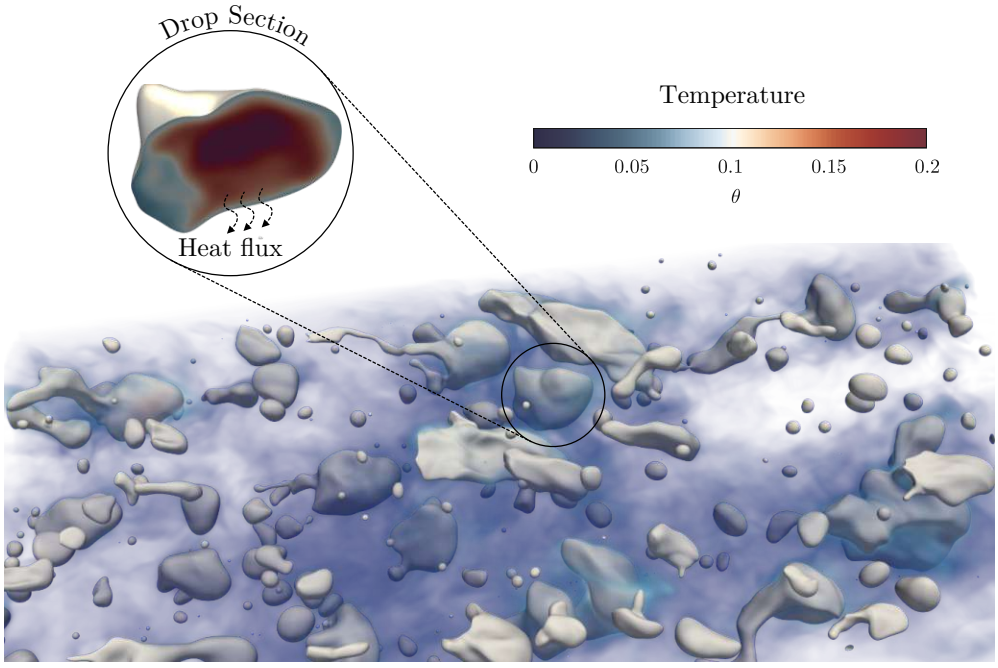

FIGURE 4.1 – Rendering of the computational setup employed for the simulations. A swarm of large and deformable drops is released in a turbulent channel flow. The temperature field is volume-rendered (blue-low, red-high) and the drops interface is shown in white (iso-level $\phi = 0$). Drops have a temperature higher than the carrier fluid (close-up view). The snapshot refers to $Pr = 1$ and $t^+ = 1000$.

it. Note that, unless differently mentioned, results are presented using the wall-unit scaling system but for the temperature field, which is made dimensionless using the initial temperature difference as a reference scale (which is a natural choice in the present case).

4.2.1 Qualitative discussion

The complex dynamics of drops immersed in a non-isothermal turbulent flow is visualized in figure 4.1, where the drops (identified by iso-contour of $\phi = 0$) are shown together with a volume-rendered distribution of temperature in the carrier fluid. Also shown in figure 4.1 is a close-up view of the temperature distribution inside the drop. We can notice that most of the drops – because of their deformability – gather at the channel center, as also observed in previous studies in similar configurations [140, 148, 106].

Once injected into the flow, each drop starts interacting with the flow and with the neighboring drops. The result of the drop-turbulence and drop-drop interactions is the occurrence of breakage and coalescence events. A breakage event happens when

Die approbierte gedruckte Originalversion dieser Dissertation ist an der TU Wien Bibliothek verfügbar.
The approved original version of this doctoral thesis is available in print at TU Wien Bibliothek.
TU Bibliothek Your knowledge hub WIEN

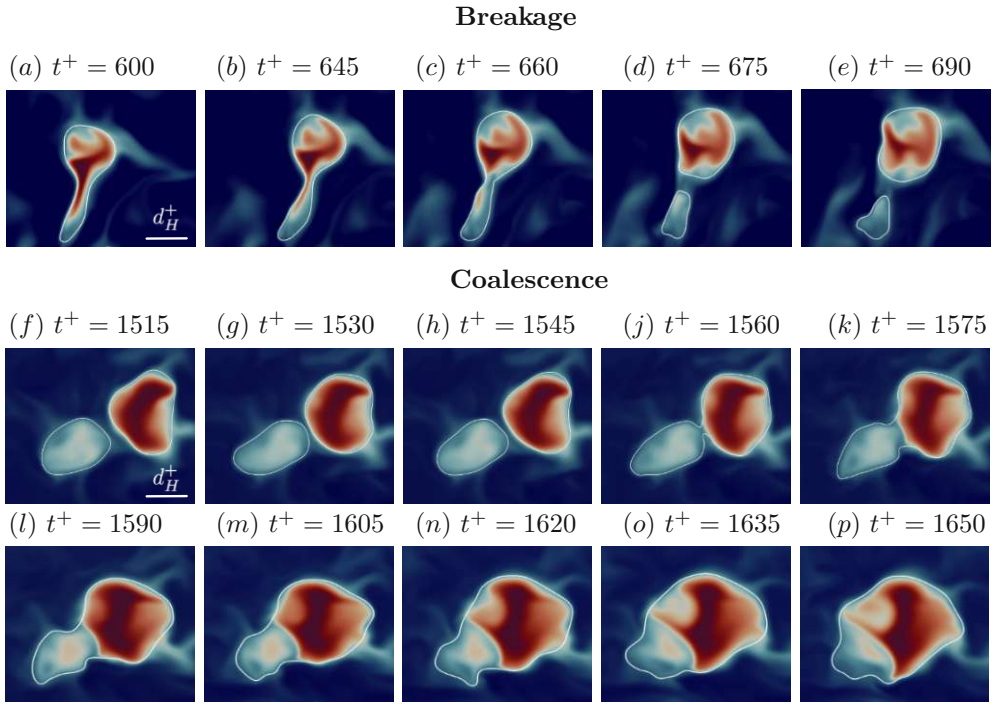

FIGURE 4.2 – Influence of topology changes on heat transfer: Time sequence of a breakage event (top row, panels *a*-*e*) and of a coalescence event (middle and bottom rows, panels *f*-*p*). During a breakage event, heat is transferred from the drops to carrier fluid thanks to the high surface/volume ratio of the pinch-off region. In the middle and bottom rows, the mixing between parcels of fluid with different temperatures can be appreciated. The two sequences refer to the case $Pr = 1$ and snapshots are separated by $\Delta t^+ = 15$. As a reference, the Kolmogorov-Hinze scale, d_H^+, is also reported.

the flow vigorously stretches the drop, leading to the formation of a thin ligament that breaks and generates two child drops. Upon separation, surface tension forces tend to retract the broken filaments and restore the drop spherical shape. A coalescence event is observed when two drops come close to each other. The small liquid film that separates the drops starts to drain, and a coalescence bridge is formed. Later, surface tension forces enter the picture, reshaping the drop and completing the coalescence process. The dynamic competition between breakage and coalescence events, and their interaction with the turbulent flow, determines the number of drops, their size distribution, and their shape/morphology (i.e., curvature, interfacial area, etc.).

In the present case, drops not only exchange momentum with the flow and with the other drops but also heat. Starting from an initial condition characterized by warm drops (with uniform temperature) and cold carrier fluid, and because of the imposed adiabatic boundary conditions, the system evolves towards an equilibrium isothermal state. During the transient to attain this thermal equilibrium state, heat is transported by diffusion and advection inside each of the two phases, and across the interface of the drops (see the temperature field inside and outside the drops, figure 4.1). The picture

Die approbierte gedruckte Originalversion dieser Dissertation ist an der TU Wien Bibliothek verfügbar.
The approved original version of this doctoral thesis is available in print at TU Wien Bibliothek.
TU Bibliothek Your knowledge hub WIEN

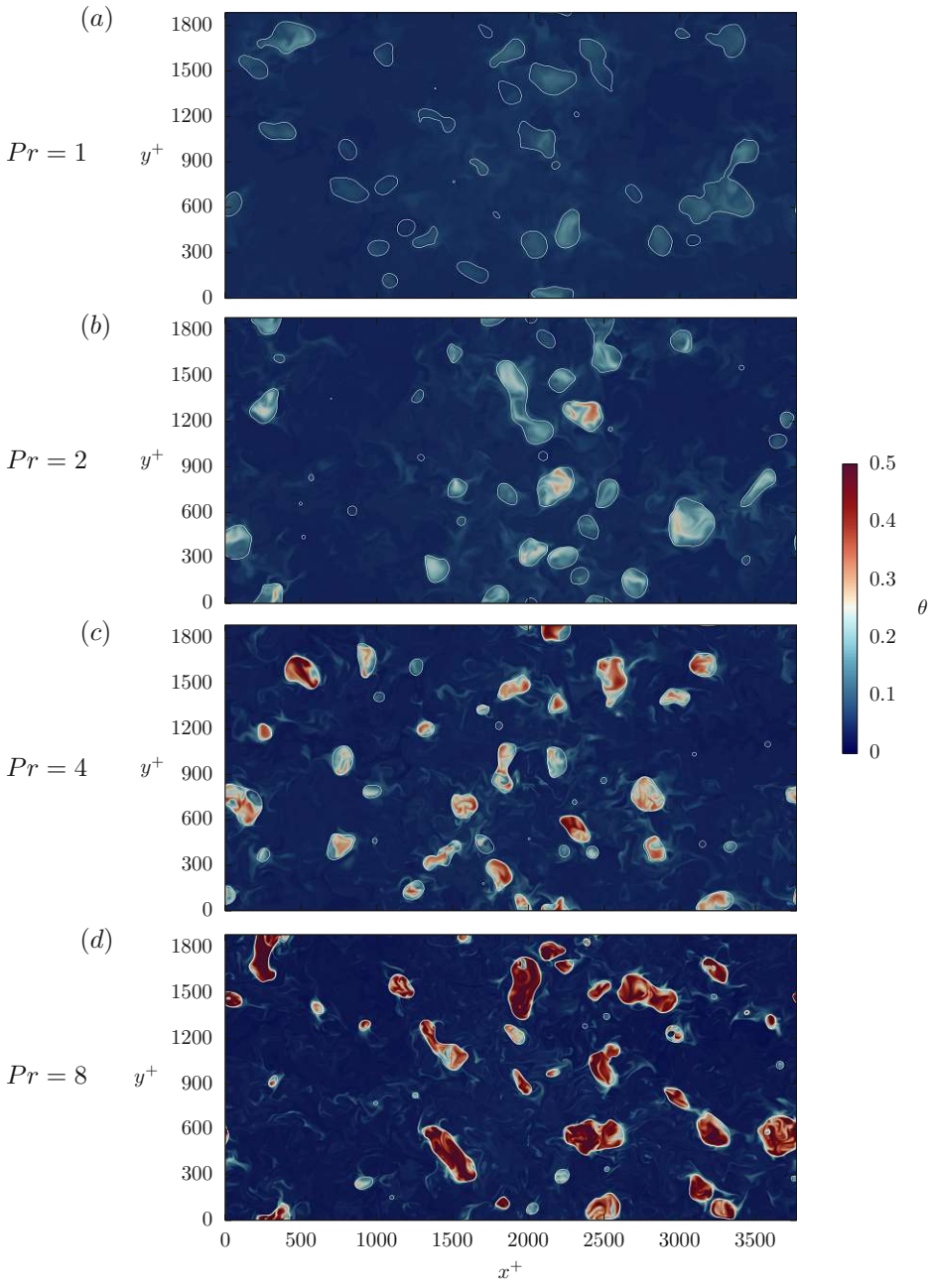

FIGURE 4.3 – Instantaneous visualization of the temperature field (red-hot; blue-cold) on a $x^+ - y^+$ plane located at the channel center for $t^+ = 1500$. Drops interface (iso-level $\phi = 0$) are reported using white lines. Each panel refers to a different Prandtl number: $Pr = 1$ (panel *a*), $Pr = 2$ (panel *b*), $Pr = 4$ (panel *c*) and $Pr = 8$ (panel *d*). By increasing the Prandtl number (from top to bottom), the heat transfer becomes slower.

Die approbierte gedruckte Originalversion dieser Dissertation ist an der TU Wien Bibliothek verfügbar.
The approved original version of this doctoral thesis is available in print at TU Wien Bibliothek.
TU Bibliothek Your knowledge hub WIEN

is then further complicated by the occurrence of breakage and coalescence events. This is represented in figure 4.2. When breakage occurs (figure 4.2, top row), a thin filament is generated (figure 4.2a-c), which then leads to the formation of a smaller satellite drop (figure 4.2d-e). The filament and the satellite drop, given the large surface-to-volume ratio, exchange heat very efficiently, and become rapidly colder. In contrast, when a coalescence occurs (figure 4.2, bottom row), two drops having different temperatures merge together. This induces an efficient mixing process, during which cold parcels of one drop become warmer and vice versa, warm parcels of the other drops become colder. Overall, breakup and coalescence events induce heat transfer modifications that are in general hard to predict *a priori*, since they do depend on the relative size of the involved parents/child drops.

Naturally, the problem of heat transfer in drop-laden turbulence is strongly influenced by the Prandtl number of the flow. This can be appreciated by looking at figure 4.3, where we show the instantaneous temperature field, together with the shape of the drops, at a certain instant in time ($t^+ = 1500$) and at the different Prandtl numbers: $Pr = 1$ (panel *a*), $Pr = 2$ (panel *b*), $Pr = 4$ (panel *c*) and $Pr = 8$ (panel *d*). In each panel, the temperature field is shown on a wall-parallel x^+-y^+ plane located at the channel center ($z^+ = 0$) and is visualized with a blue-red scale (blue-low, red-high). We observe that the temperature field changes significantly with Pr. In particular, we notice an increase in the drop-to-fluid temperature difference for increasing Pr, going from $Pr = 1$ (top panel) where this difference is small, to $Pr = 8$ (bottom panel) where this difference is large. The heat transfer from the drops to the carrier fluid becomes slower as Pr increases, consistently with a physical situation in which the Pr number is increased by reducing the thermal diffusivity of the fluid while keeping the momentum diffusivity constant (i.e. constant kinematic viscosity, and hence shear Reynolds number). Also, the temperature structures, both inside and outside the drop, become thinner and more complicated at higher Pr, since their characteristic length scale, the Batchelor scale $\eta_\theta^+ \propto Pr^{-1/2}$, becomes smaller for increasing Pr [9, 10]. In addition, smaller drops have, on average, a lower temperature compared to larger drops, regardless of the value of Pr. All these aspects will be discussed in more detail in the next sections.

4.2.2 Drop Size Distribution

To characterize the collective dynamics of the drops, we compute the drop size distribution (DSD) at steady-state conditions, averaging over a time window $\Delta t^+ = 3000$, from $t^+ = 3000$ to 6000. The achievement of steady-state conditions is here evaluated by monitoring global flow properties, like flow rate and wall stress, and drop properties, like the number of drops and the overall drops surface. It is worth mentioning that a quasi-equilibrium DSD, very close to the steady one, is already achieved around $t^+ \simeq 750$, and only minor changes occur to the DSD afterward.

Figure 4.4 shows the DSD obtained for the different cases considered here: $Pr = 1$ (dark violet), $Pr = 2$ (violet), $Pr = 4$ (pink), and $Pr = 8$ (light pink). Drop size distribution profiles are statistically the same. Small differences are due to the initial turbulence field, which is different for each simulation (see 4.1). The DSDs have been computed considering, for each drop, the diameter of the equivalent sphere computed

Die approbierte gedruckte Originalversion dieser Dissertation ist an der TU Wien Bibliothek verfügbar.
The approved original version of this doctoral thesis is available in print at TU Wien Bibliothek.
TU Bibliothek Your knowledge hub WIEN

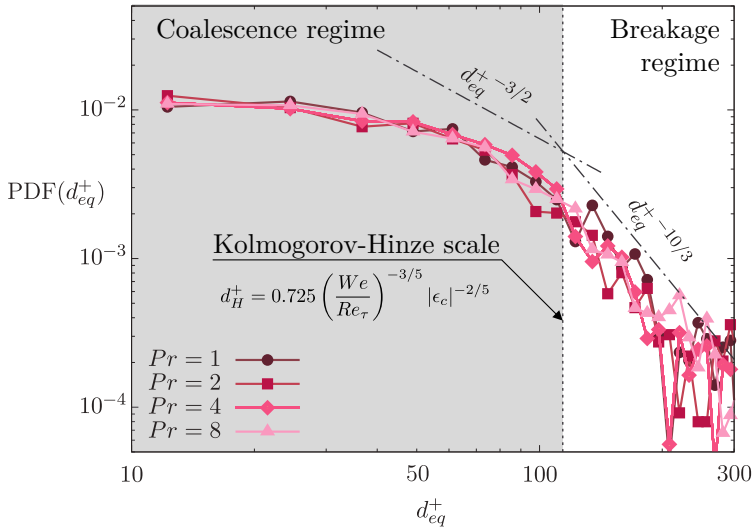

FIGURE 4.4 – Steady-state drop size distributions (DSD) obtained for: $Pr = 1$ (dark violet, circles), $Pr = 2$ (violet, squares), $Pr = 4$ (pink, diamonds) and $Pr = 8$ (light pink, triangles). The Kolmogorov-Hinze (KH) scale d_H^+ is reported with a vertical dashed line while the two analytical scaling laws: ${d_{eq}^+}^{-3/2}$ for the coalescence-dominated regime (small drops, gray region) and ${d_{eq}^+}^{-10/3}$ for the breakage-dominated regime (larger drops, white region) are reported with dash-dotted lines.

as:

$$d_{eq}^{+} = \left(\frac{6V^{+}}{\pi}\right)^{1/3}, \tag{4.1}$$

where V^+ is the volume of the drop. Also reported in figure 4.4 is the Kolmogorov-Hinze scale, d_H^+, which can be computed as [121, 132, 145]:

$$d_H^+ = 0.725 \left(\frac{We}{Re_\tau}\right)^{-3/5} |\epsilon_c|^{-2/5}, \tag{4.2}$$

where ϵ_c is the turbulent dissipation, here evaluated at the channel center where most of the drops collect because of their deformability [98, 148, 106]. Although recently challenged [129, 158, 115], the Kolmogorov-Hinze scale [85, 72] still represents a convenient estimate to evaluate the critical diameter below which drop breakage is unlikely to occur. Based on the Kolmogorov-Hinze scale, we can identify two different regimes [57, 40, 42]. For drops smaller than the Kolmogorov-Hinze scale, we find the coalescence-dominated regime (left, gray area), in which drops, that are smaller than the critical scale, are generally not prone to break (although violent breakages can happen also for smaller drops). For drops larger than the Kolmogorov-Hinze scale, we find the breakage-dominated regime (right, white area) in which drops breakage is more likely to happen. Each regime is characterized by a specific scaling law, which describes the behaviour of the drops number density as a function of the drop size [57, 40, 32]: $PDF \sim {d_{eq}^+}^{-3/2}$, below Kolmogorov-Hinze scale, and $PDF \sim {d_{eq}^+}^{-10/3}$ above it. The two scalings are represented by dot-dashed lines in figure 4.4.

Die approbierte gedruckte Originalversion dieser Dissertation ist an der TU Wien Bibliothek verfügbar.
The approved original version of this doctoral thesis is available in print at TU Wien Bibliothek.
TU Bibliothek Your knowledge hub WIEN

We note that, for equivalent diameters above the Hinze scale, our results follow quite well the theoretical scaling law and match the drops/bubbles size distributions obtained in literature considering similar flow instances [43, 45, 149, 42, 37]. Below the Hinze scale, for equivalent diameters in the range $25 < d_{eq}^{+} < d_{H}^{+}$ our results match reasonably well the theoretical scaling law. For equivalent diameters $d_{eq}^{+} < 25$ $w.u.$, we observe an underestimation of the DSD compared to the proposed scaling. This is linked to the grid resolution, and in particular to the problem in describing very small drops [149, 135].

Time evolution of the drop size distribution

We report here the drop size distributions obtained at different time instants. In particular, we show here the results obtained for the case $Pr = 1$, which with any loss of generality, can be applied to all the cases analyzed being the Reynolds and Weber numbers considered the same ($Re_{\tau} = 300$ and $We = 3.0$). Figure 4.5 shows the resulting time evolution of the drop size distribution. The different time instants are reported with different colors, from black (initial stages of the simulation) to gray (later stages of the simulation). The Kolmogorov-Hinze (KH) scale, $d_{H}^{+} = 114$ $w.u.$, and the initial drop size, $d^{+} = 120$ $w.u.$, are reported with vertical dashed lines. Likewise, the scaling laws for the coalescence and breakage-dominated regime are reported with dash-dotted lines. Analyzing the results, we can observe that for the first time instant reported ($t^{+} = 735$; black-full circles), the drop size distribution partially deviates from the steady-state distribution obtained for $t^{+} \geq 3000$. It is worth observing that memory of the initial condition is somehow visible as there is a peak at approximately the initial size, this peak is slightly shifted towards smaller values due the initial mass leakage that occurs in the initial stages of the simulations. However, already at $t^{+} = 1100$ (light black, full squares) and for the subsequent time instants, the deviation from the steady-state size distribution ($t^{+} \geq 3000$) becomes marginal and memory of the initial conditions is completely lost and the peak vanishes. For these latter stages, the size distribution can be well approximated using a combination of the two scaling laws: ${d^{+}}^{-3/2}$ for the coalescence-dominated regime and ${d^{+}}^{-10/3}$ in the breakage-dominated regime.

4.2.3 Mean temperature of drops and carrier fluid

We now focus on the average temperature of the drops and of the carrier fluid. We consider the ensemble of all drops as one phase, and the carrier fluid as the other phase (using the value of the phase field as a phase discriminator), and we compute the average temperature for each phase. The evolution in time of the drops and carrier fluid temperature, $\overline{\theta}_d$ and $\overline{\theta}_c$ respectively, is shown in figure 4.6, for the different values of Pr. Together with the results obtained by current DNSs, filled symbols, in figure 4.6 we also show the predictions obtained by a simplified phenomenological model (solid lines), the details of which will be described and discussed later (see section 4.2.4). We start considering the DNS results only. As expected, we observe that the average temperature of the drops (violet to pink symbols) decreases in time, while the average temperature of the carrier fluid (blue to cyan symbols) increases in time, until the thermodynamic equilibrium, at which both phases have the same

Die approbierte gedruckte Originalversion dieser Dissertation ist an der TU Wien Bibliothek verfügbar.
The approved original version of this doctoral thesis is available in print at TU Wien Bibliothek.
TU Bibliothek Your knowledge hub WIEN

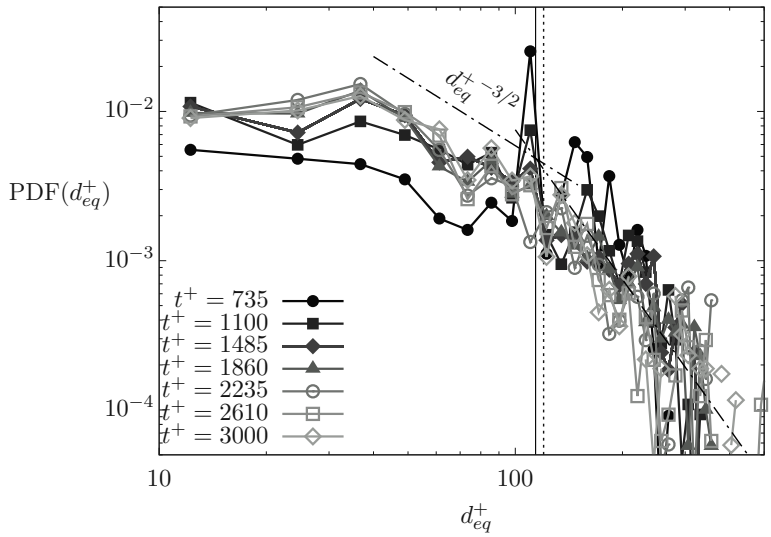

FIGURE 4.5 – Time evolution of the drop size distribution for $Pr = 1$. The different time instants are reported with different combination of colors and symbols (black-initial stages; gray-late stages). The Kolmogorov-Hinze (KH) scale ($114w.u.$) and the initial drop size (120 $w.u.$) are reported with a vertical continuous and dashed line, respectively. The two analytical scaling laws, ${d_{eq}^+}^{-3/2}$ for the coalescence-dominated regime (small drops, gray region) and ${d_{eq}^+}^{-10/3}$ for the breakage-dominated regime (larger drops, white region) are reported with dash-dotted lines.

temperature, is asymptotically reached. For this reason, simulations have been run long enough for the average temperature of both phases to be sufficiently close to the equilibrium temperature. In particular, we stopped the simulations at $t^+ \simeq 6000$, when the condition

$$\frac{(\overline{\theta}_d - \theta_{eq})}{(\theta_{d,0} - \theta_{eq})} \leq 0.05\,, \tag{4.3}$$

with $\theta_{d,0}$ the initial temperature of the drops, is satisfied by all simulations. The equilibrium temperature, θ_{eq}, can be easily estimated a-priori: since the two walls are adiabatic, and the homogeneous directions are periodic, the energy of the system is conserved over time. After some algebra, and recalling the definition of volume fraction, $\Phi = V_d/(V_d + V_c)$, we obtain the equilibrium temperature:

$$\theta_{eq} = \theta_{c,0}(1 - \Phi) + \theta_{d,0}\Phi\ , \tag{4.4}$$

which is represented by the horizontal dashed line in figure 4.6.
Figure 4.6 provides also a clear indication that the higher the Prandtl number, the larger the time it takes for the system to reach the equilibrium temperature, θ_{eq}. The trend can be observed for both the drops and carrier fluid, as the two phases are mutually coupled (the heat released from the drops is adsorbed by the carrier fluid). This result confirms our previous qualitative observations, see figure 4.3 and discussion therein, that a large Pr (small thermal diffusivity) reduces the heat released by the drops. It is also interesting to observe that the behaviour of the mean temperature of the two phases appears self-similar at the different Pr.

Die approbierte gedruckte Originalversion dieser Dissertation ist an der TU Wien Bibliothek verfügbar.
The approved original version of this doctoral thesis is available in print at TU Wien Bibliothek.
TU Bibliothek Your knowledge hub WIEN

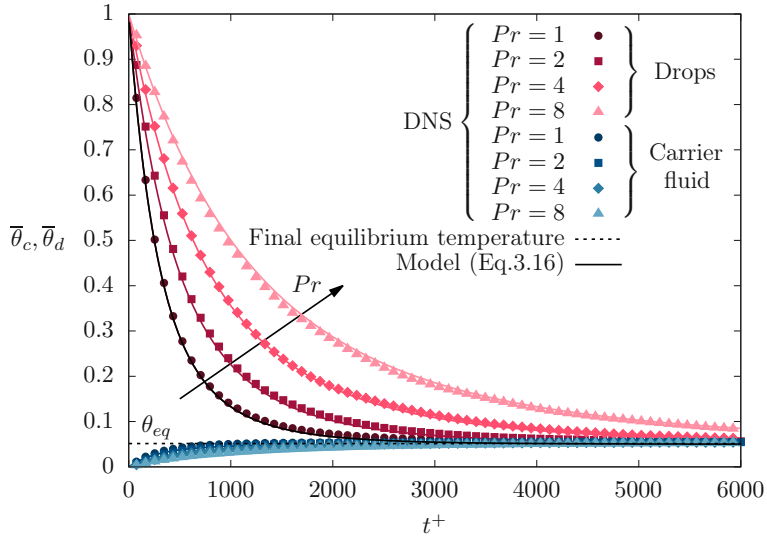

FIGURE 4.6 – Time evolution of the mean temperature of drops (violet to pink colors, different symbols) and carrier fluid (blue to cyan colors, different symbols) for the different Prandtl numbers considered. DNS results are reported with full circles while the predictions obtained from the model are reported with continuous lines. The equilibrium temperature of the system, θ_{eq}, is reported with a horizontal dashed line.

4.2.4 A phenomenological model for heat transfer rates in droplet laden flows

In an effort to provide a possible interpretation of the previous results – and in particular to explain the average temperature behaviour shown in figure 4.6 –, we develop a simple physically sound model of the heat transfer in drop-laden turbulence. We start by considering the heat transfer mechanisms from a single drop of diameter d^* to the surrounding fluid:

$$m_d^* c_p^* \frac{\partial \theta_d^*}{\partial t^*} = \mathcal{H}^* A_d^* \left(\theta_c^* - \theta_d^*\right) , \tag{4.5}$$

where m_d^*, A_d^*, and c_p^* are the mass, external surface, and specific heat of the drop, $\mathcal{H}^*$ is the heat transfer coefficient, while θ_d^* and θ_c^* are the drops and carrier fluid temperature. The heat transfer coefficient can be estimated as the ratio between the thermal conductivity of the external fluid, λ^*, and a reference length scale, here represented by the thermal boundary layer thickness δ_t^*:

$$\mathcal{H}^* \sim \lambda^* / \delta_t^* . \tag{4.6}$$

With this assumption, and recalling that $\rho^* = \rho_c^* = \rho_d^*$, equation 4.5 becomes:

$$\frac{\partial \theta_d^*}{\partial t^*} = \frac{6}{Pr} \frac{\nu^*}{d^* \delta_t^*} \left(\theta_c^* - \theta_d^*\right) . \tag{4.7}$$

Die approbierte gedruckte Originalversion dieser Dissertation ist an der TU Wien Bibliothek verfügbar.
The approved original version of this doctoral thesis is available in print at TU Wien Bibliothek.
TU Bibliothek Your knowledge hub WIEN

Reportedly [142], the thermal boundary layer thickness, δ_t^*, can be expressed as $\delta_t^* = \delta^* Pr^{-\alpha}$ where δ^* is the momentum boundary layer thickness, and α is an exponent that depends on the flow condition in the proximity of the boundary where the boundary layer evolves. In particular, the exponent α ranges from $\alpha = 1/3$ for no-slip conditions, usually assumed for solid particles, to $\alpha = 1/2$, usually assumed for clean gas bubbles. For an in-depth discussion on the topic, we refer the reader to appendix B. As a consequence, the heat transfer rate observed from drops/bubbles is expected to be larger than that observed from solid particles, since the no-slip boundary condition generally weakens the flow motion near the interface [92, 68, 12]. We can now rewrite the equation of the model in dimensionless form, using the initial drop-to-carrier fluid temperature difference $\Delta\theta^* = \theta_{d,0}^* - \theta_{c,0}^*$ as reference temperature, and ν^*/u_τ^{*2} as reference time:

$$\frac{\partial \theta_d}{\partial t^+} = 6 Re_\delta^{-1} Pr^{-1+\alpha} \left(d^+\right)^{-1} (\theta_c - \theta_d) \,, \tag{4.8}$$

where d^+ is the drop diameter in wall units, while $Re_\delta = u_\tau^* \delta^* / \nu^*$ is the Reynolds number based on the boundary layer thickness (which can be assumed constant among the different cases). Equation 4.8 can be rewritten as:

$$\frac{\partial \theta_d}{\partial t^+} = \mathcal{C} Pr^{-1+\alpha} \left(d^+\right)^{-1} (\theta_c - \theta_d) \,, \tag{4.9}$$

where $\mathcal{C}$ is a constant whose value depends only on the flow structure, i.e. on Re_δ. Equation 4.9 describes the heat released by a single drop of dimensionless diameter d^+. Assuming now that the turbulent flow is laden with drops of different diameters the general equation describing the heat released by the i-th drop of diameter d_i^+ becomes:

$$\frac{\partial \theta_{d,i}}{\partial t^+} = \mathcal{C} Pr^{-1+\alpha} \left(d_i^+\right)^{-1} (\theta_c - \theta_d) = \mathcal{F}_i \,, \tag{4.10}$$

where $\mathcal{F}_i$ is the lumped-parameters representation of the right-hand side of the temperature evolution equation for the i-th drop. As widely observed in literature [40, 147], and also confirmed by the present study (figure 4.4), we can hypothesize an equilibrium drops-size-distribution (DSD) by which the number density of drops scales as $d^{+-3/2}$, in the sub-Hinze range of diameters ($10 < d^+ < 110$), and as $d^{+-10/3}$ in the super-Hinze range of diameters ($110 < d^+ < 240$). With this approximation, and considering 7 classes of drops diameter for the sub-Hinze range, and 4 classes for the super-Hinze range, we can integrate equation 4.10 to obtain the time evolution of the temperature of each drop in time:

$$\theta_{d,i}^{n+1} = \theta_{d,i}^n + \Delta t^+ \mathcal{F}_i \,. \tag{4.11}$$

From a weighted average of the temperature (based on the number of drops in each class, as per the theoretical DSD), we obtain the average temperature of the drops, $\overline{\theta}_d$.

To obtain the mean temperature of the carrier fluid, we consider that (adiabatic condition at the walls), the heat released by the drops is entirely absorbed by the carrier

Die approbierte gedruckte Originalversion dieser Dissertation ist an der TU Wien Bibliothek verfügbar.
The approved original version of this doctoral thesis is available in print at TU Wien Bibliothek.
TU Bibliothek Your knowledge hub WIEN

fluid. The heat released by the drops with a certain diameter d_i^*, can be computed as:

$$Q_i^* = m_d^* c_p^* \frac{\partial \theta_d}{\partial t^+} N_d^*(i)\,, \tag{4.12}$$

where $N_d^*(i)$ is the number of drops for that specific diameter (as per the DSD). The overall heat released by all drops can be calculated as the summation over all different classes of diameters:

$$Q_{tot}^* = \sum_{i=1}^{N_c} Q_i^*\,, \tag{4.13}$$

where N_c is the employed number of classes. Finally, the mean temperature of the carrier fluid is

$$\overline{\theta}_c^{*,n+1} = \theta_c^{*,n} + \Delta t^+ \frac{Q_{tot}^*}{m_c^* c_p^*}\,. \tag{4.14}$$

In dimensionless form (dividing by the initial drop-to-carrier fluid temperature $\Delta\theta^*$) equation 4.14 becomes:

$$\overline{\theta}_c^{n+1} = \theta_c^n + \Delta t^+ Q_{tot}\,. \tag{4.15}$$

The results of the model are shown in figure 4.6. Interestingly, under the simplified hypothesis of the model (chiefly, the spherical shape of the drops, constant drop-size-distribution evaluated at the equilibrium), we observe that the behaviour of the mean temperature is very well captured by the model (represented by the solid lines in figure 4.6)

$$\frac{\partial \theta_d}{\partial t^+} = \mathcal{C} Pr^{-2/3} \left(d^+\right)^{-1} \left(\theta_c - \theta_d\right)\,, \tag{4.16}$$

i.e. when $\alpha = 1/3$ – typical of boundary layers around solid objects (i.e. solid particles). Reasons for this behaviour might be traced back to the weakening of convective phenomena induced by the interface of the drops [141]. This effects is more pronounced at the beginning of the simulation when large drops are not yet present. In addition, it must be also noticed that drops are strongly advected by the mean flow, and the flow condition at the drop surface can be different from the slip one and is in general not of simple evaluation. Given the relationship $\partial\theta_d/\partial t \sim Pr^{-2/3}$ postulated by the model (equation 4.16), which provides results in very good agreement with the numerical ones, it seems reasonable to rescale the time variable as:

$$\tilde{t}^+ = \frac{t^+}{Pr^{(1-\alpha)}} = \frac{t^+}{Pr^{(2/3)}}\,. \tag{4.17}$$

A representation of the DNS results in terms of the rescaled time, equation 4.17, is shown in figure 4.7. We observe a nice collapse of the two sets of curves – drops and carrier fluid (red and blue) – for the different values of Pr, which clearly demonstrates the self-similar behaviour of $\overline{\theta}$. For this reason, the rescaling of time $\tilde{t}^+ = t^+/Pr^{2/3}$, will be also used in the following.

Die approbierte gedruckte Originalversion dieser Dissertation ist an der TU Wien Bibliothek verfügbar.
The approved original version of this doctoral thesis is available in print at TU Wien Bibliothek.
TU Bibliothek Your knowledge hub WIEN

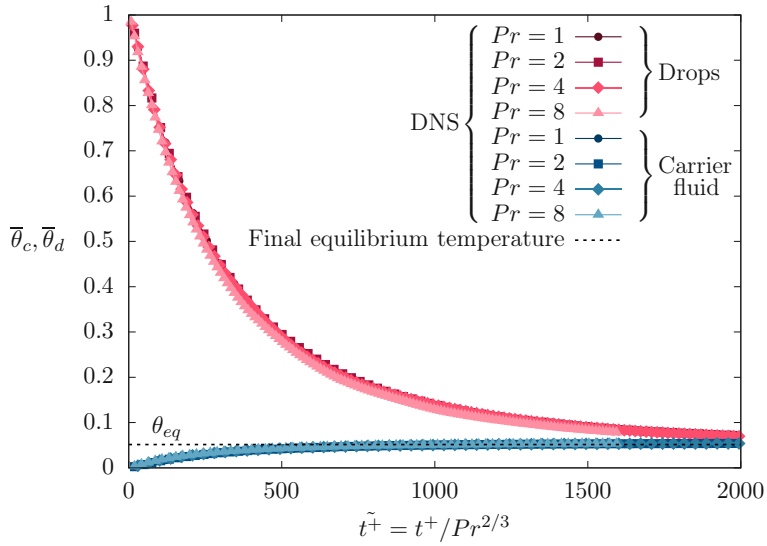

FIGURE 4.7 – Time evolution of the mean temperature of drops (violet to pink colors) and carrier fluid (blue to cyan colors) for the different Prandtl numbers considered obtained from DNS and reported against the dimensionless time $\tilde{t}^+ = t^+/Pr^{2/3}$. The equilibrium temperature of the system, θ_{eq}, is reported with a horizontal dashed line. The DNS results reported over the new dimensionless time nicely collapse on top of each other, highlighting the self-similarity of the $\overline{\theta}_{c,d}$ profiles.

4.2.5 Heat transfer from particles and drops/bubbles

It is now important to discuss the behaviour of the heat transfer coefficient (and its dimensionless counterpart, the Nusselt number Nu), also in the context of available literature results. Naturally, similar considerations can be made to evaluate the mass transfer coefficient, in particular at liquid/gas interfaces [92, 12].
For solid particles, a balance between the convective time scale near the surface, and the diffusion time scale, gives a heat transfer coefficient [87]:

$$\mathcal{H}^* \propto Pr^{-2/3}\,, \tag{4.18}$$

and the corresponding Nusselt number:

$$Nu \propto Re^{\beta} Pr^{1/3}\,, \tag{4.19}$$

where β is an exponent that depends on the flow conditions and links the boundary layer thickness to the particle Reynolds number. Usually, $\beta = 1/3$ for small Reynolds numbers [87] while $\beta = 1/2$ for large Reynolds numbers [130, 165, 112].
Using similar arguments (balance between convective and diffusion time scales), but considering now that at the surface of a drop/bubble a slip velocity, and therefore a certain degree of advection, can be observed [92, 12, 68], the heat transfer coefficient is found to scale as:

$$\mathcal{H}^* \propto Pr^{-1/2}\,, \tag{4.20}$$

Die approbierte gedruckte Originalversion dieser Dissertation ist an der TU Wien Bibliothek verfügbar.
The approved original version of this doctoral thesis is available in print at TU Wien Bibliothek.
TU Bibliothek Your knowledge hub WIEN

and the corresponding Nusselt number as:

$$Nu \propto Re^{\beta} Pr^{1/2}\,, \tag{4.21}$$

where also in this case the exponent β does depend on the considered Reynolds number. Two regimes are usually defined [152]: a low Reynolds number regime, for which $\beta = 1/2$, and a high Reynolds number regime, for which $\beta = 3/4$. An alternative approach, which gives similar predictions, is to use the penetration theory of Higbie [71], in which turbulent fluctuations are invoked to estimate a flow exposure (or contact) time, to compute the heat/mass transfer coefficient. Such an approach has been widely used in bubble-laden flows [35, 67, 68, 118].

We can now evaluate the heat transfer coefficient from our DNS at different Pr, and compare it to the proposed scaling laws. Note that the heat transfer coefficient is obtained as:

$$\mathcal{H} = \frac{(\overline{\theta}_d^{n+1} - \overline{\theta}_d^{n})}{A\Delta t(\overline{\theta}_d^{n+1/2} - \overline{\theta}_c^{n+1/2})}\,, \tag{4.22}$$

where the numerator represents the temperature difference of the drops between the time steps n and $n+1$, while the denominator represents the temperature difference between the drop and the carrier fluid evaluated halfway in time between step n and $n+1$ (i.e. at $n+1/2$). The quantity A is the total interfacial area between drops and carrier fluid, while Δt is the time step used to evaluate the heat transfer. Here, we have evaluated the heat transfer coefficient taking the heat released by the drops as a reference; an equivalent result, but with the opposite sign, can be obtained using the heat absorbed by the carrier fluid as a reference, and taking into account the different volume fraction of the two phases.

The dimensionless heat transfer coefficient, equation 4.22, is shown as a function of Pr, and at different time instants (based on the dimensionless time $\tilde{t}^{+}$, equation 4.17), in figure 4.8. Further details on the time evolution of $\mathcal{H}$ are given in Appendix 4.2.8. For a better comparison, the results are normalized by the value of the heat transfer coefficient for $Pr = 1$. The two reference scaling laws, $\mathcal{H} \sim Pr^{-2/3}$ obtained for $\alpha = 1/3$ and $\mathcal{H} \sim Pr^{-1/2}$ obtained for $\alpha = 1/2$ are also shown by a dotted and a dashed line. We note that at the beginning of the simulations (see for example $\tilde{t}^{+} = 250$), the heat transfer coefficient is close to $\mathcal{H} \sim Pr^{-2/3}$, while at later times it tends towards $\mathcal{H} \sim Pr^{-1/2}$, hence approaching the scaling law proposed for heat/mass transfer in gas-liquid flows [92, 105, 12, 67, 68, 36, 118].

A possible explanation is that, as time advances, the shape of the drops becomes complex, and coalescence/breakups more frequent, thus inducing a higher degree of internal mixing that is associated with a heat transfer increase. This is reflected in a heat transfer process that is slower at the beginning, $\mathcal{H}^{*} \sim Pr^{-2/3}$, and faster at later times $\mathcal{H}^{*} \sim Pr^{-1/2}$.

4.2.6 Influence of the drop size on the average drop temperature

In the previous sections, we have studied the behaviour of the mean temperature field of the drops and of the carrier fluid considered as single entities. However, while this

Die approbierte gedruckte Originalversion dieser Dissertation ist an der TU Wien Bibliothek verfügbar.
The approved original version of this doctoral thesis is available in print at TU Wien Bibliothek.
TU Bibliothek Your knowledge hub WIEN

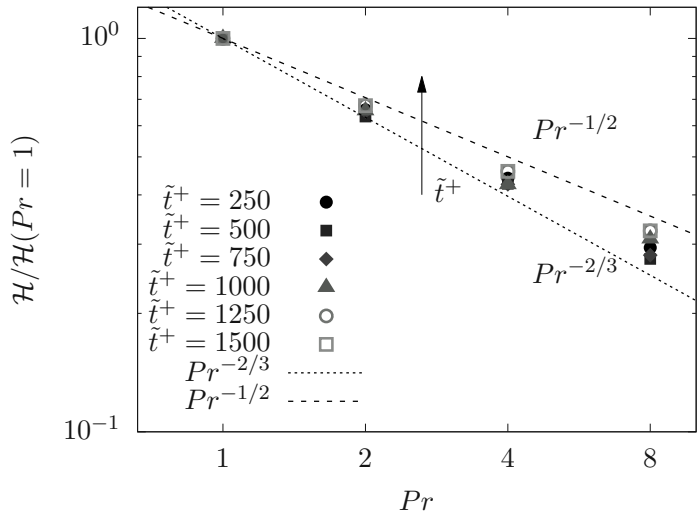

FIGURE 4.8 – Time behaviour of the dimensionless heat transfer coefficient for the different Prandtl numbers considered. The results are compared for different values of the newly defined dimensionless time $\tilde{t}^+ = t^+/Pr^{2/3}$. Heat transfer coefficients are reported normalized by the value of the heat transfer coefficient obtained for $Pr = 1$ (at the same time instant $\tilde{t}^+$). In this way, results obtained at different time instants can be conveniently compared. The two scaling laws that refer to $\alpha = 2/3$ and $\alpha = 1/2$ are also reported as references.

description is perfectly reasonable for the carrier fluid – which can be considered a continuum – it can be questionable for the drops, which are not a continuum phase by nature. We now take the dispersed nature of the drops into account and we evaluate, for each drop, the equivalent diameter and the corresponding mean temperature.

This is sketched in figure 4.9, where the average temperature of each drop (represented by a dot) is shown as a function of its equivalent diameter, at different time instants (between $t^+ = 1050$ and $t^+ = 2400$). Each panel refers to a different Prandtl number. Note that, at $t^+ = 2400$, the case $Pr = 1$ has almost reached the thermodynamic equilibrium (figure 4.6). It is clearly visible that, regardless of the considered time, small drops have an average temperature close to the equilibrium one. This is particularly visible at smaller Prandtl numbers, i.e. when heat transport is faster, but it can be observed also at larger Pr. In contrast, the average temperature of larger drops is larger. Hence, the average temperature of the drops seems directly proportional to the drop size, as can be argued considering that the heat released by the drop, and hence its temperature reduction, is $\partial\theta_d/\partial t \propto d^{-1}$ (equation 4.14). It is therefore not surprising that the scatter plot at a given time instant is characterized by dots distributing in a stripes-like fashion, with a slope that decreases with time. This behaviour is observed at all Pr, although the range of drops temperature (y axis) at small Pr is definitely narrower (because of their larger heat loss) compared to that at large Pr. It is also interesting to note – in particular at $Pr = 4$ and $Pr = 8$ (panels c and d) – the presence of drops with a temperature smaller than the equilibrium one (dots falling below the horizontal line that marks the equilibrium temperature). We can link this behaviour

Die approbierte gedruckte Originalversion dieser Dissertation ist an der TU Wien Bibliothek verfügbar.
The approved original version of this doctoral thesis is available in print at TU Wien Bibliothek.
TU Bibliothek Your knowledge hub WIEN

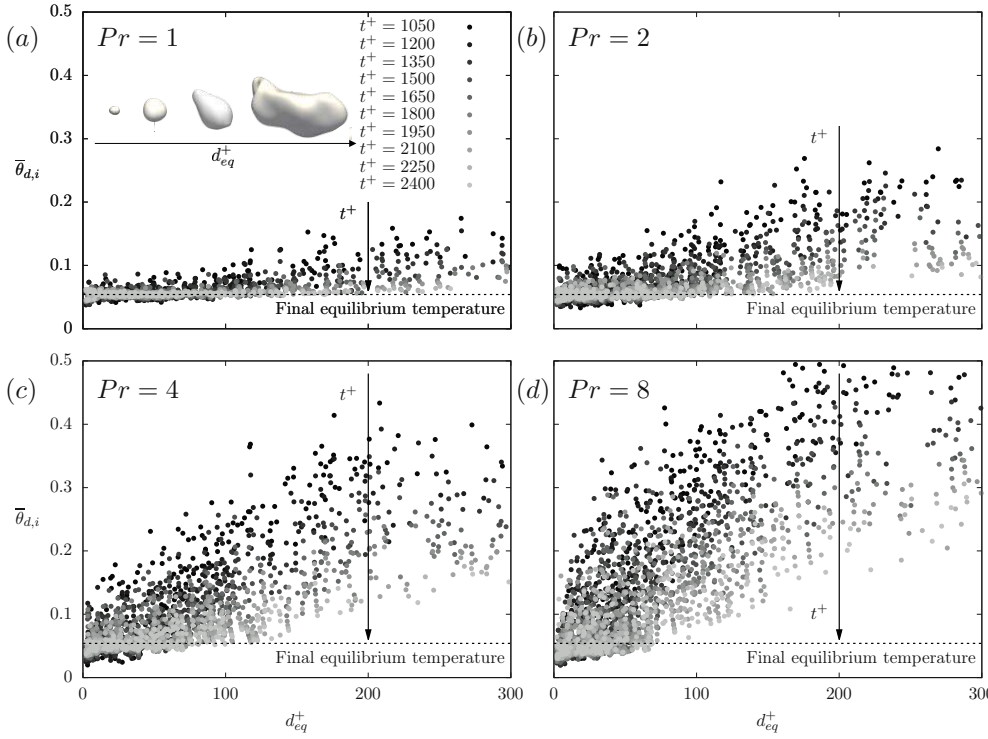

FIGURE 4.9 – Scatter plot of the drop equivalent diameter d_{eq}^+ against the drop average temperature, $\overline{\theta}_{d,i}$. Each dot represents a different drop while its color (black to gray colormap) identifies different times, from $t^+ = 1050$ (black) up to $t^+ = 2400$ (gray). Each panel refers to a different Prandtl number. A sketch showing drops of different equivalent diameters is reported in the upper part of panel *a*.

to the small relaxation time of small drops that therefore adapt quickly to the local temperature of the carrier fluid, which can be smaller than the equilibrium one for two main reasons. First, at the early stages of the simulations, and at high Prandtl numbers, the temperature of the carrier fluid is lower than the equilibrium one. Second, temperature fluctuations (of both negative and positive signs) are present also in the carrier fluid. These fluctuations, in the form of hot/cold striations, are more likely observed at large Pr (see the striation-like structures at $Pr = 8$ in figure 4.3*d*).

4.2.7 Temperature fluctuations inside the drops

In many applications, in particular, to evaluate mixing efficiency and flow homogeneity, not only the average temperature of drops is important, but also its space and time distribution inside the drops. To understand it, we now look at the PDF of the temperature fluctuations inside the drops,

$$\theta_d' = \theta_d - \overline{\theta}_d \,, \tag{4.23}$$

Die approbierte gedruckte Originalversion dieser Dissertation ist an der TU Wien Bibliothek verfügbar.
The approved original version of this doctoral thesis is available in print at TU Wien Bibliothek.
TU Bibliothek Your knowledge hub WIEN

where θ_d is the local temperature inside the drop, and $\overline{\theta}_d$ is the average temperature of all drops at a certain time (as per figure 4.6). Results are shown in figure 4.10. The first row of figure 4.10 shows the probability density function of θ'_d at different Pr, and at two different time instants: $t^+ = 600$ (panel a, left) and $t^+ = 1500$ (panel b, right). The second row of figure 4.10 shows the PDFs obtained at two different rescaled time instants, $\tilde{t}^+ = t^+/Pr^{2/3}$: $\tilde{t}^+ = 600$ (panel c, left) and $\tilde{t}^+ = 1500$ (panel d, right).

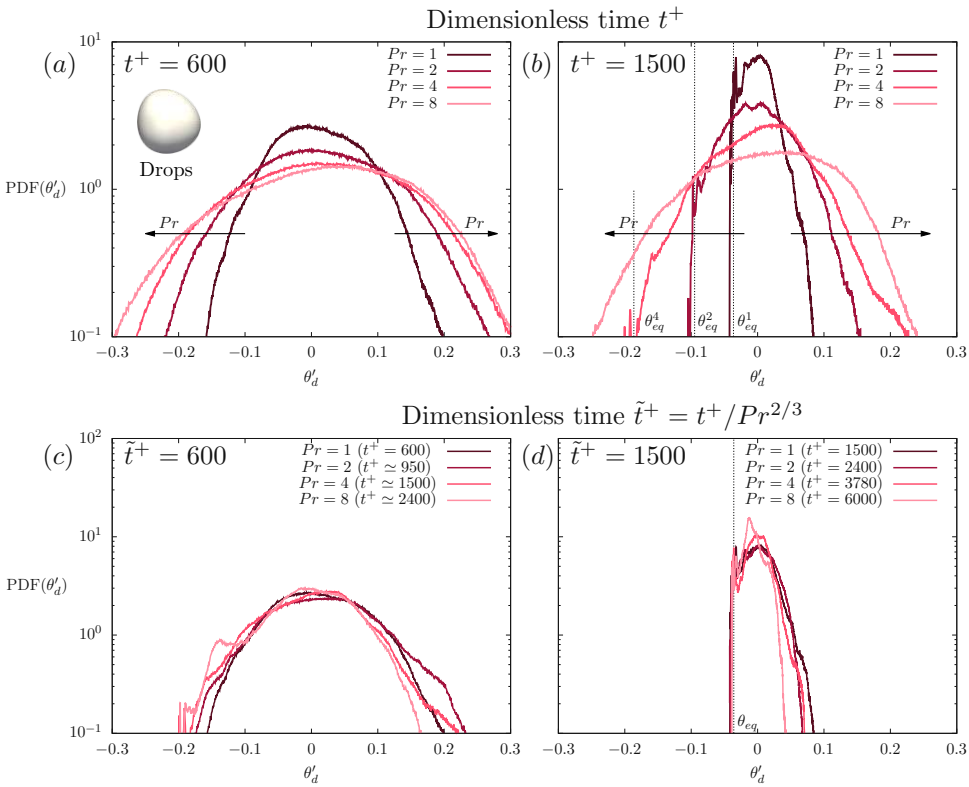

FIGURE 4.10 – Probability density function (PDF) of the temperature fluctuations, $\theta'_d = \theta_d - \overline{\theta}_d$ inside the drops. Each case is reported with a different color (violet to light pink) depending on the Prandtl number. The first row shows the PDFs obtained at two different time instants: $t^+ = 600$ (panel a) and $t^+ = 1500$ (panel b). The second row shows the PDFs obtained at two rescaled time instants $\tilde{t}^+ = 600$ (panel c) and $\tilde{t}^+ = 1500$ (panel d), where the rescaled time is computed as $\tilde{t}^+ = t^+/Pr^{2/3}$. For panels c-d, the corresponding t^+ is reported between brackets.

Considering first figure 4.10a ($t^+ = 600$), we notice that all PDFs have a rather regular shape, characterized by the presence of both positive and negative fluctuations (with respect to the average temperature), with a slight asymmetry towards the positive ones (positive fluctuations are more likely observed). A comparison between the curves obtained at different Pr shows that the range of temperature fluctuations is wider at larger Pr. This is due to the small thermal diffusivity at large Pr, which allows temperature fluctuations in the drop to survive much longer before they are damped

Die approbierte gedruckte Originalversion dieser Dissertation ist an der TU Wien Bibliothek verfügbar.
The approved original version of this doctoral thesis is available in print at TU Wien Bibliothek.
TU Bibliothek Your knowledge hub WIEN

and spread by diffusion. Naturally, at later times (figure 4.10*b*, $t^+ = 1500$), the range of temperature fluctuations reduces. Indeed, as heat is transferred from the drops to the carrier fluid, the maximum temperature of drops reduces, and so does the range of temperature fluctuations inside the drop. This trend is more pronounced for negative fluctuations, as the minimum temperature inside the drops is somehow bounded by the temperature of the carrier fluid (which increases only a little, from $\overline{\theta}_{c,0} = 0$ to $\theta_{eq} = 0.054$, during the simulation). This latter observation is visible in the shape of the PDFs at $Pr = 1, 2$ and 4, since the system is closer to the thermal equilibrium at this time instant (the thermal equilibrium is identified in panel *b* by a vertical dashed line and marked with a label, θ_{eq}^{Pr}): a sharp drop of the PDF, which does not significantly trespass the θ_{eq}^{Pr} limit, is observed. In contrast, positive temperature fluctuations are subject to relatively weaker constraints (they are only bounded by the maximum initial temperature of the drops). This results in a PDF that gets asymmetric, positively-skewed. It is also interesting to observe the development of a pronounced peak about the equilibrium temperature θ_{eq}^{Pr}, which corresponds to the presence of small drops (generated by breakages events) that – given their small thermal relaxation time and heat capacity – almost immediately adapt to the equilibrium temperature (see also figure 4.2*d*,*f*).

However, a discussion on the temperature fluctuations, captured from flows at different Pr and after the same time t^+ from the initial condition, could be misleading because it puts in contrast flows at different thermal states (i.e. different average temperatures, and different temperature gradients, see figure 4.6). To filter out this effect, we compute the PDFs of the temperature fluctuations at the same rescaled time instants $\tilde{t}^+ = t^+/Pr^{2/3}$. By doing this, all cases can be considered at similar thermal conditions (see also figure 4.7). The resulting PDFs, at $\tilde{t}^+ = 600$ and $\tilde{t}^+ = 1500$, are shown in figure 4.10*c*-*d*. Note that, for the sake of clarity, the corresponding t^+, which is different from case to case, is reported between brackets in the legend. In the rescaled time units, the collapse between the different curves is quite nice. The slight difference between the curves is due to the fact that, although the system is at the same thermal state (same $\tilde{t}^+$), it is at a different flow state (different t^+), i.e. the instantaneous drop size distributions are different. This gives the slightly larger negative fluctuations at larger Pr (which, being at a later stage, is characterized by the presence of smaller and colder drops), and slightly larger positive fluctuations at smaller Pr (which, being at an earlier flow state, is characterized by the presence of larger and warmer drops).

From a closer look at figure 4.10*d* ($\tilde{t}^+ = 1500$), we note very clearly the constraint set by the thermal equilibrium condition: the PDF cannot significantly trespass the limit represented by θ_{eq} (vertical dashed line), which is very similar for all Pr, given the similar thermal state.Also visible is the peak, already discussed in figure 4.10*b*, that emerges very close to the equilibrium temperature θ_{eq}, and which is due to the presence of small drops that adapt quickly to the local temperature of the carrier fluid. As previously noticed in figure 4.10*c*, the higher probability of finding small drops at lower Pr is also responsible for the narrowing of the PDF (reduction of positive temperature fluctuations).

Die approbierte gedruckte Originalversion dieser Dissertation ist an der TU Wien Bibliothek verfügbar.
The approved original version of this doctoral thesis is available in print at TU Wien Bibliothek.
TU Bibliothek Your knowledge hub WIEN

4.2.8 Time evolution of the heat transfer coefficient

In this section, we report the time evolution of the heat transfer coefficient $\mathcal{H}$, evaluated as per equation 4.22, for the different values of the Prandtl number Pr considered here. Results are shown in figure 4.11 as a function of the dimensionless time $\tilde{t}^+ = t^+/Pr^{2/3}$. Considering figure 4.11a, we can observe that the heat transfer coefficient exhibits a self-similar behaviour, and after an initial transient (after $\tilde{t} > 1000$) it attains a steady-state condition for all the different cases. Upon rescaling of the heat transfer coefficient $\mathcal{H}$ by the factor $Pr^{2/3}$, we observe a fair collapse of all curves on top of each other. Some minor differences are perhaps observed at high Prandtl numbers. Note indeed that at high Prandtl numbers the curves become a bit more noisy, as the rescaling factor amplifies the fluctuations of the heat transfer coefficient.

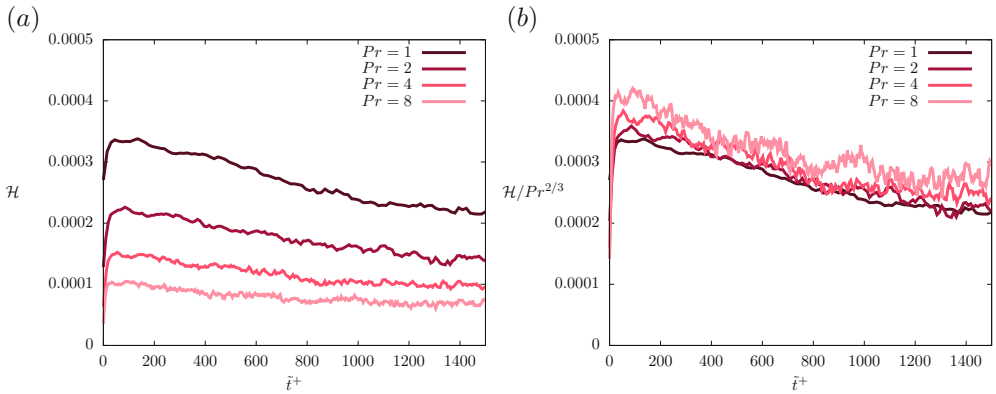

FIGURE 4.11 – Time evolution of the heat transfer coefficient as a function of the dimensionless time $\tilde{t}^+ = t^+/Pr^{2/3}$ for the different Prandtl numbers considered. In panel a, the heat transfer is shown as per equation 4.22, while in panel b it is rescaled by the factor $Pr^{2/3}$.

4.3 Conclusions

In this work, we studied heat transfer in a turbulent channel flow laden with large and deformable drops. The drops are initially warmer than the carrier fluid and as the simulations advance, heat is transferred from the drops to the carrier fluid. Simulations considered a fixed value of the Reynolds number, $Re_\tau = 300$, and Weber number, $We = 3$, and analyzed different Prandtl number values, from $Pr = 1$ to $Pr = 8$. The Prandtl number is changed by changing the thermal diffusivity. The investigation is based on the DNS of turbulent heat transfer, coupled with a phase-field method, used to describe interfacial phenomena. First, we focused on the drops dynamics, observing that after an initial transient (up to $t^+ = 1000$), the drop size distribution (DSD) reaches a quasi-equilibrium condition where it follows the scaling $d_{eq}^{+\,-3/2}$ in the coalescence-dominated regime and $d_{eq}^{+\,-10/3}$ in the breakage-dominated regime. The threshold between the coalescence-dominated and the breakage-dominate

Die approbierte gedruckte Originalversion dieser Dissertation ist an der TU Wien Bibliothek verfügbar.
The approved original version of this doctoral thesis is available in print at TU Wien Bibliothek.
TU Bibliothek Your knowledge hub WIEN

regimes is represented by the Kolmogorov-Hinze scale. Then, we characterize the behaviour of the average temperature of the drops and of the carrier fluid: as expected, the average temperature of drops decreases in time, while the average temperature of the carrier fluid increases in time, until reaching the equilibrium condition of uniform temperature in the whole system. We clearly observed that the higher the Prandtl number, the larger the time it takes for the system to reach the equilibrium temperature. Interestingly, the time behaviour of the temperature profiles of both drops and carrier fluid is self-similar.

Building on top of these numerical results, we developed a phenomenological model that can accurately reproduce the time evolution of the mean temperatures at all Prandtl numbers considered here. This model gave us the opportunity to introduce a new self-similarity variable (time, $\tilde{t}^+$) that accounts for the Prandtl number effect, and by which all results collapse on a single curve. In addition, we also computed the heat transfer coefficient $\mathcal{H}$ (and its dimensionless counterpart, the Nusselt number Nu) and showed that it scales as $\mathcal{H} \sim Pr^{-2/3}$ (which corresponds to a Nusselt number scaling $Nu \sim Pr^{1/3}$) at the beginning of the simulation, and tends to $\mathcal{H} \sim Pr^{-1/2}$ (or, alternatively, $Nu \sim Pr^{1/2}$) at later times. These different scalings are consistent with previous literature predictions and can be explained via the boundary layer theory (appendix B). The effects of the Prandtl number on the temperature distribution inside the drops have been investigated. We observe that by increasing the Prandtl number, the PDFs become wider and thus large temperature fluctuations are more likely to be observed. Interestingly, when the PDFs are compared at the same rescaled time $\tilde{t}^+$ (i.e. accounting for the Prandtl number effect), all curves collapse on top of each other, with only minor differences possibly due to the different instantaneous drop size distribution. The effect of the drop size was also discussed: small drops adapt faster to the equilibrium temperature, thanks to their small heat capacity, compared to larger drops. Finally, it must be pointed out that, since the different phases of a multiphase flow can have different thermophysical properties, Prandtl numbers can be also different from phase to phase. This aspect, which was not considered in the present work, will be the topic of a future study.

Die approbierte gedruckte Originalversion dieser Dissertation ist an der TU Wien Bibliothek verfügbar.
The approved original version of this doctoral thesis is available in print at TU Wien Bibliothek.
TU Bibliothek Your knowledge hub WIEN

Die approbierte gedruckte Originalversion dieser Dissertation ist an der TU Wien Bibliothek verfügbar.
The approved original version of this doctoral thesis is available in print at TU Wien Bibliothek.

5

Viscosity influence on heat transfer in drop-laden turbulence

Reproduced in part from:

F. Mangani and A. Soldati, *Viscosity influence on heat transfer in drop-laden turbulence*, in preparation.

Heat transfer in turbulent dispersed multiphase flows is a complex and rich-in-physics phenomenon. When heat is initially confined in the dispersed fluid and then transferred to the carrier fluid, the whole heat transfer process is significantly influenced by the presence of the interface separating the fluids, and by all related interfacial phenomena. Indeed, deformation, breakage and coalescence events, which normally affect drops in turbulent flows, can impact the heat transport by intensifying or hampering the mixing of heat. A central role in the heat transfer process is played by the thermophysical properties of the fluids, namely surface tension, density, viscosity and thermal diffusivity. All these properties directly or indirectly impact the heat transfer efficiency. Surface tension, viscosity and density (the latter only within the passive scalar approximation) indirectly influence heat transfer, acting on the flow field and drops dynamics, which, in turn, act on the heat transport. By contrast, thermal diffusivity directly influence heat diffusion, and consequently it has a direct effect on the overall heat transport. In most two-phase systems, the dispersed and carrier phase have different thermophysical properties, therefore the heat mixing inside the drops can differ from the heat mixing in the carrier fluid. Such differences increase as the ratio between the drops over carrier property increases.

This chapter aims at evaluating the effect produced by thermophysical properties contrasts on the heat transfer process in a drop-laden turbulent flow. The study here reported focuses in particular on the analysis of the effects induced by viscosity contrasts. Density and thermal diffusivity contrasts, instead, will not be taken into account. The investigation is performed by coupling direct numerical simulation (DNS) of turbulence with a phase-field method (PFM) for the interface description.

In order to mimic a realistic two-phase flow, an oil-water system will be considered, where water and oil have different viscosities but the same density and thermal diffusivity, which is a reasonable approximation for most oil-water mixtures. Two cases are investigated: the first case is characterized by warm water drops in a cold turbulent channel flow of oil, while the second case is characterized by warm oil drops in

a cold turbulent channel flow of water. The second case thus corresponds to the first case with the two fluids (oil and water) being switched. In addition, a case where the dispersed and carrier fluids have equal viscosities is simulated, as a reference. The oil considered for the present simulations has a viscosity four times larger than the water viscosity. The Prandtl number (ratio of momentum over thermal diffusivity) is set for the carrier phase and is automatically determined for the dispersed phase. More specifically, since a constant density and thermal diffusivity are considered, the ratio between the Prandtl number in the drops and the Prandtl number in the carrier fluid will be exactly equal to the viscosity ratio. The shear Reynolds number is also set for the carrier phase in each case, and its value is chosen in order to maintain a constant Péclet number in the system, namely a constant ratio between convective and diffusive heat transfer. This setup allows to focus on the effect of the viscosity ratio on the velocity field and consequently on the heat convection, while keeping a constant heat diffusion.

The objective of this study is to evaluate the impact of the viscosity ratio on the macroscopic heat transfer process, characterizing first the drops dynamics in terms of drop size distribution, and analysing then the time behaviour of the average temperature of the drops and carrier fluid.

The chapter is organized as follows: in section 5.2.1 the results are discussed from a qualitative viewpoint; then a more quantitative analysis is reported in 5.2.2 and 5.2.3, where the drop size distribution and the time evolution of the temperature field are discussed, respectively.

5.1 Simulation setup

A turbulent channel flow, driven by an imposed constant pressure gradient in the streamwise direction, is adopted for all the simulated cases. The dimensions of the computational domain are $L_x \times L_y \times L_z = 4\pi h \times 2\pi h \times 2h$. The value of the Weber number is kept constant and equal to $We = 3.0$, which is representative of liquid-liquid systems.

The influence of the viscosity on the heat transfer process is studied by considering two different viscosity ratios μ_r, where $\mu_r = \mu_d/\mu_c$, being μ_d the drops viscosity and μ_c the carrier fluid viscosity. The chosen viscosity ratios are $\mu_r = 0.25$ and $\mu_r = 4$, which mimic the real-case scenarios of water drops in oil and oil drops in water, respectively, considering an oil which has a viscosity four times larger than the water viscosity. A reference case with $\mu_r = 1$, namely with matched viscosity in the two phases, is additionally considered. The density and thermal diffusivity are kept constant. Therefore the density ratio, ρ_r (ratio of drops over carrier density) and the thermal diffusivity ratio, α_r (ratio of drops over carrier thermal diffusivity) are both unitary, which is a reasonable assumption for oil-water mixtures.

The Prandtl number, Pr, is set for the carrier phase and defined based on the carrier phase properties, according to Eq. 2.47. A value of $Pr = 16$ is chosen for the oil carrier phase (i.e. in the case with $\mu_r = 0.25$), while a value of $Pr = 4$ is chosen for the water carrier phase (i.e. in the case with $\mu_r = 4$). An intermediate value of $Pr = 8$ is used in the carrier phase of the reference case. The value of the Prandtl number in the dispersed phase is determined by the imposition of the viscosity ratio. Indeed,

Die approbierte gedruckte Originalversion dieser Dissertation ist an der TU Wien Bibliothek verfügbar.
The approved original version of this doctoral thesis is available in print at TU Wien Bibliothek.
TU Bibliothek Your knowledge hub WIEN

the ratio of Prandtl numbers, Pr_r, between the dispersed and carrier phase can be obtained from

$$Pr_r = \frac{\nu_r}{\alpha_r} = \frac{\mu_r}{\rho_r \alpha_r}\,, \tag{5.1}$$

where ν_r is the kinematic viscosity ratio (ratio of drops over carrier kinematic viscosity). Since ρ_r and α_r are unitary, the Prandtl ratio results in

$$Pr_r = \mu_r\,, \tag{5.2}$$

thus the Prandtl in the dispersed phase, Pr_d, can be calculated as

$$Pr_d = \mu_r Pr\,. \tag{5.3}$$

The shear Reynolds is also set for the carrier phase and defined based on the carrier phase properties, according to Eq. 2.45. In order to keep a constant Péclet number in the system - the dimensionless number that quantifies the ratio between diffusive and convective heat transfer, defined as $Pe = Re_\tau Pr$ - a shear Reynolds of $Re_\tau = 150$ is set in the oil carrier phase (i.e. in the case with $Pr = 16$ and $\mu_r = 0.25$), while a shear Reynolds of $Re_\tau = 600$ is imposed in the water carrier phase (i.e. in the case with $Pr = 4$ and $\mu_r = 4$). This choice allows to have a constant Péclet of $Pe = 2400$ in the two systems. In addition to the three drop-laden simulations, three isothermal single-phase flow simulations are performed with the corresponding shear Reynolds numbers, in order to provide initial velocity fields for the multiphase simulations.
The grid resolution used to resolve the continuity, Navier-Stokes and Cahn-Hilliard equations is equal to $N_x \times N_y \times N_z = 1024 \times 512 \times 1025$ in the non-matched-viscosity cases, and $N_x \times N_y \times N_z = 1024 \times 512 \times 513$ in the reference case. A more refined grid is instead adopted to solve the energy equation for all the three cases, with $N_x \times N_y \times N_z = 2048 \times 1024 \times 1025$ points. The computational grid has uniform spacing in the homogeneous directions, while a Chebyshev-Gauss-Lobatto spacing is used in the wall-normal direction. In table 5.1 an overview of the main physical and computational parameters of the simulations is given. Considering the chosen grid resolution, the Cahn number is set to $Ch = 0.01$, and the phase field Péclet number is therefore set as $Pe_\phi = 1/Ch = 100$, to achieve convergence to the sharp interface limit.
The grid resolution, above mentioned, has been chosen considering that when the drops and the carrier fluid have different viscosities, the local Reynolds number inside the drops changes with respect to the shear Reynolds number characterizing the carrier fluid. As a consequence, the range of spatiotemporal scales that needs to be resolved to comply with the DNS requirements changes as well. In order to properly simulate the flow in both the drops and carrier fluid, thus with the only purpose of choosing an adequate grid, the ratio between the drops and carrier Reynolds has been estimated as $1/\mu_r$, considering that the density ratio is $\rho_r = 1$ and using the same characteristic length scale h (channel height) and velocity scale u_τ (friction velocity) used for the carrier fluid. We consider this estimation to be cautionary, since we expect the drop size to be at most comparable to the channel height, and the velocity scale in the drops

Die approbierte gedruckte Originalversion dieser Dissertation ist an der TU Wien Bibliothek verfügbar.
The approved original version of this doctoral thesis is available in print at TU Wien Bibliothek.
TU Bibliothek Your knowledge hub WIEN

Case	Re_τ	Pr	μ_r	ρ_r	α_r	We	$N_x \times N_y \times N_z$ (NS+CH)	$N_x \times N_y \times N_z$ (Energy)
SP1	150	-	-	-	-	-	$512 \times 256 \times 513$	-
SP2	300	-	-	-	-	-	$512 \times 256 \times 513$	-
SP3	600	-	-	-	-	-	$512 \times 256 \times 513$	-
DL1	150	16	0.25	1	1	3.0	$1024 \times 512 \times 1025$	$2048 \times 1024 \times 1025$
DL2	300	8	1	1	1	3.0	$1024 \times 512 \times 513$	$2048 \times 1024 \times 1025$
DL3	600	4	4	1	1	3.0	$1024 \times 512 \times 1025$	$2048 \times 1024 \times 1025$

TABLE 5.1 – Overview of simulation parameter. Three viscosity ratio are considered, $\mu_r = 0.25$, 1 and 4. The Prandtl and shear Reynolds number, imposed for the carrier fluid, are $Pr = 16$ and $Re_\tau = 150$ for $\mu_r = 0.25$, $Pr = 8$ and $Re_\tau = 300$ for $\mu_r = 0.25$ and $Pr = 4$ and $Re_\tau = 600$ for $\mu_r = 4$. The density and thermal diffusivity ratios are kept unitary and the Weber number is fixed, $We = 3.0$, for all the cases. In addition, three single phase simulations are performed, for the three different shear Reynolds numbers. The grid resolution employed to solve the Navier-Stokes and Cahn-Hilliard equation (NS+CH) and the energy equation are also illustrated.

internal flow to be comparable or smaller than the friction velocity. The Reynolds in the dispersed phase, $Re_{\tau d}$, can be therefore estimated as

$$Re_{\tau d} \simeq \frac{Re_\tau}{\mu_r} \,. \tag{5.4}$$

In table 5.2 we report for each simulation the shear Reynolds set for the carrier phase Re_τ and the Reynolds estimated in the dispersed phase $Re_{\tau d}$, with the corresponding grid size in wall units for the carrier phase, based on Re_τ, and for the dispersed phase, based on $Re_{\tau d}$. All dimensions refer to the channel centre, where most drops are located. In addition, the Kolmogorov scale, which is used here to provide an estimation of the smallest length scale inside the drops and in the carrier fluid, has been computed as follows

$$\eta_k^+ = \left(\frac{1}{\epsilon^+}\right)^{1/4} \qquad \eta_{k,d}^+ = \left(\frac{\mu_r^3}{\rho_r^3 \epsilon^+}\right)^{1/4} \tag{5.5}$$

for the drops and carrier respectively, where ϵ^+ is the turbulent dissipation at the channel center evaluated in the region characterized by $\phi \geq 0$ for the drops, and by $\phi \leq 0$ for the carrier.

For the resolution of the energy field, a more refined grid is chosen in order to resolve all the spatiotemporal scales down to the Batchelor scale, which is defined based on the Kolmogorov scale as $\eta_\theta = \eta_k/\sqrt{Pr}$. In table 5.3, similarly to table 5.2, we report the Prandtl set for the carrier phase Pr and the Prandtl calculated in the dispersed phase Pr_d, with the more refined grid size in wall units for the carrier phase, based on Re_τ, and for the dispersed phase, based on $Re_{\tau d}$. Additionally, the Batchelor scale in the carrier and dispersed phases are also included, where their values have been calculated as

$$\eta_\theta^+ = \frac{\eta_k^+}{\sqrt{Pr}} \qquad \eta_{\theta,d}^+ = \frac{\eta_{k,d}^+}{\sqrt{Pr_d}} \tag{5.6}$$

Die approbierte gedruckte Originalversion dieser Dissertation ist an der TU Wien Bibliothek verfügbar.
The approved original version of this doctoral thesis is available in print at TU Wien Bibliothek.
TU Bibliothek Your knowledge hub WIEN

respectively, based on the value of the Kolmogorov scale reported in 5.2. It can be noticed that for all the cases presented here, the estimated Kolmogorov and Batchelor scales are of the order of the grid spacing or slightly bigger, thus ensuring a correct resolution of all the relevant scales.

Case	μ_r	Re_τ	Δx^+	Δy^+	Δz^+	η_k^+	$Re_{\tau d}$	$\Delta x^{+,d}$	$\Delta y^{+,d}$	$\Delta z^{+,d}$	$\eta_{k,d}^+$
DL1	0.25	150	1.84	1.84	0.46	3.54	600	7.36	7.36	1.84	1.34
DL2	1	300	3.68	3.68	1.84	4.17	300	3.68	3.68	1.84	4.16
DL3	4	600	7.36	7.36	1.84	4.84	150	1.84	1.84	0.46	13.7

TABLE 5.2 – Grid resolution of the flow field and Kolmogorov scale at the channel center, reported in wall units according to the shear Reynolds of the carrier fluid, Re_τ, (Δx^+, Δy^+, Δz^+ and η_k^+), and according to the estimated shear Reynolds of the drops, $Re_{\tau d}$, ($\Delta x^{+,d}$, $\Delta y^{+,d}$, $\Delta z^{+,d}$ and $\eta_{k,d}^+$), for the three considered viscosity ratios.

Case	μ_r	Pr	Δx_θ^+	Δy_θ^+	Δz_θ^+	η_θ^+	Pr_d	$\Delta x_\theta^{+,d}$	$\Delta y_\theta^{+,d}$	$\Delta z_\theta^{+,d}$	$\eta_{\theta,d}^+$
DL1	0.25	16	0.92	0.92	0.46	0.88	4	3.68	3.68	1.84	0.67
DL2	1	8	1.84	1.84	0.92	1.47	8	1.84	1.84	0.92	1.72
DL3	4	4	3.68	3.68	1.84	2.42	16	0.92	0.92	0.46	3.42

TABLE 5.3 – Grid resolution of the temperature field and Batchelor scale at the channel center, reported in wall units according to the shear Reynolds of the carrier fluid, Re_τ, (Δx_θ^+, Δy_θ^+, Δz_θ^+ and η_θ^+), and according to the estimated shear Reynolds of the drops, $Re_{\tau d}$, ($\Delta x_\theta^{+,d}$, $\Delta y_\theta^{+,d}$, $\Delta z_\theta^{+,d}$ and $\eta_{\theta,d}^+$), for the three considered viscosity ratios. The Prandtl numbers in the carrier fluid, Pr and in the drops Pr_d, employed for the estimation of the Batchelor scale, are also reported.

All drop-laden simulations are initialized with a regular array of 256 spherical drops with diameter $d = 0.4h$ inside a fully-developed turbulent flow field (obtained from the preliminary single-phase simulations). The drops volume fraction is $\Phi = V_d/(V_c + V_d) = 5.4\%$, where V_d and V_c are the volume of the drops and carrier fluid, respectively. The temperature field is initialized so that all drops are initially warm (with an initial temperature of $\theta_{d,0} = 1$) and the carrier fluid is initially cold (initial temperature $\theta_{c,0} = 0$). The transition between drops and carrier fluid in the temperature field is initially smoothed by means of an hyperbolic tangent kernel, to avoid numerical instabilities that might arise from a discontinuous temperature field.

Die approbierte gedruckte Originalversion dieser Dissertation ist an der TU Wien Bibliothek verfügbar.
The approved original version of this doctoral thesis is available in print at TU Wien Bibliothek.
TU Bibliothek Your knowledge hub WIEN

5.2 Results

In the following, the results obtained from the numerical simulations will be discussed from a qualitative viewpoint, by means of instantaneous drops, temperature and flow visualizations, and then evaluated from a more quantitative viewpoint, by looking at the influence of the viscosity ratio on the drop size distribution and on the average drops and fluid temperature.

5.2.1 Qualitative observations

In Figure 5.1 a qualitative view of the instantaneous temperature and velocity fields can be observed together with the drops interface, at a certain instant in time (t=6) and for the three different viscosity ratios: $\mu_r = 0.25$ top row, $\mu_r = 1$ middle row and $\mu_r = 4$ bottom row. The temperature field, θ, is shown on the left column while the velocity fluctuation magnitude field, $|\mathbf{u}'|$, is shown on the right column, where $|\mathbf{u}'| = \sqrt{u'^2 + v'^2 + w'^2}$ (being u', v' and w' the velocity fluctuations components). In each panel the temperature and velocity fields are visualized on a wall-parallel $x^+ - y^+$ plane located at the channel center ($z^+ = 0$). The temperature is shown with a blue-red scale (blue, low; red, high) while the velocity fluctuation is shown with a white-black scale (white, low; black, high). The drops interface, identified by the iso-contour of $\phi = 0$, is marked with a thin white line in each snapshot. We start by looking at the temperature field in the three different cases (Fig. 5.1*a*, 5.1*c* and 5.1*e*). We notice that in all the cases the temperature field is characterized by a similar range of values, and that the drop-to-fluid temperature difference is roughly the same. This seems to suggest that the three fields are at a similar stage of the thermal transient, in which drops have lost a similar amount of heat providing it to the carrier fluid. Focusing then exclusively on the carrier fluid, we observe that for $\mu_r = 0.25$ (panel *a*) the carrier temperature field is characterized by rather large structures, with significant temperature variations that can be appreciated by the presence of white-to-blue and blue-to-black colour contrasts. Moving on to $\mu_r = 1$ (panel *c*) and further to $\mu_r = 4$ (panel *e*), the smallest size of the temperature structures reduces progressively with respect to $\mu_r = 0.25$, as well as the temperature variations, as the colour contrasts are less pronounced and a more uniform temperature field can be observed. This outcome is coherent with the increase of the shear Reynolds in the carrier fluid, from $Re_\tau = 150$ (when $\mu_r = 0.25$) up to $Re_\tau = 600$ (when $\mu_r = 4$), which causes a reduction of the smallest turbulent structures and enhances the mixing of heat. An analogous difference, although less clear, can be noticed in the drops temperature field: for the high viscosity ratio $\mu_r = 4$ the smallest temperature structures are slightly bigger than for $\mu_r = 1$ and than for $\mu_r = 0.25$, as well as the temperature variations per each drop. In accordance with these observations, we notice that for $\mu_r = 0.25$, namely when drops are less viscous than the carrier fluid, smaller temperature structures and a higher mixing are visible inside the drops with respect to the carrier fluid, while for $\mu_r = 4$, namely when drops are more viscous than the carrier fluid, finer structures and a higher mixing are evident in the carrier fluid with respect to the drops. We now move on to discussing the velocity fluctuation fields (Fig. 5.1*b*, 5.1*d* and 5.1*f*). We notice that, similarly to the temperature structures, the velocity structures in

Die approbierte gedruckte Originalversion dieser Dissertation ist an der TU Wien Bibliothek verfügbar.
The approved original version of this doctoral thesis is available in print at TU Wien Bibliothek.
TU Bibliothek Your knowledge hub WIEN

the carrier fluid reduce their size while the ones in the drops increase their size as the viscosity ratio is increased (from panel b to panel d and further to panel f). As expected, there is a qualitative match between the velocity field and the corresponding temperature field for each case, as areas with a uniform temperature correspond to areas with uniform intensity of the velocity fluctuations.

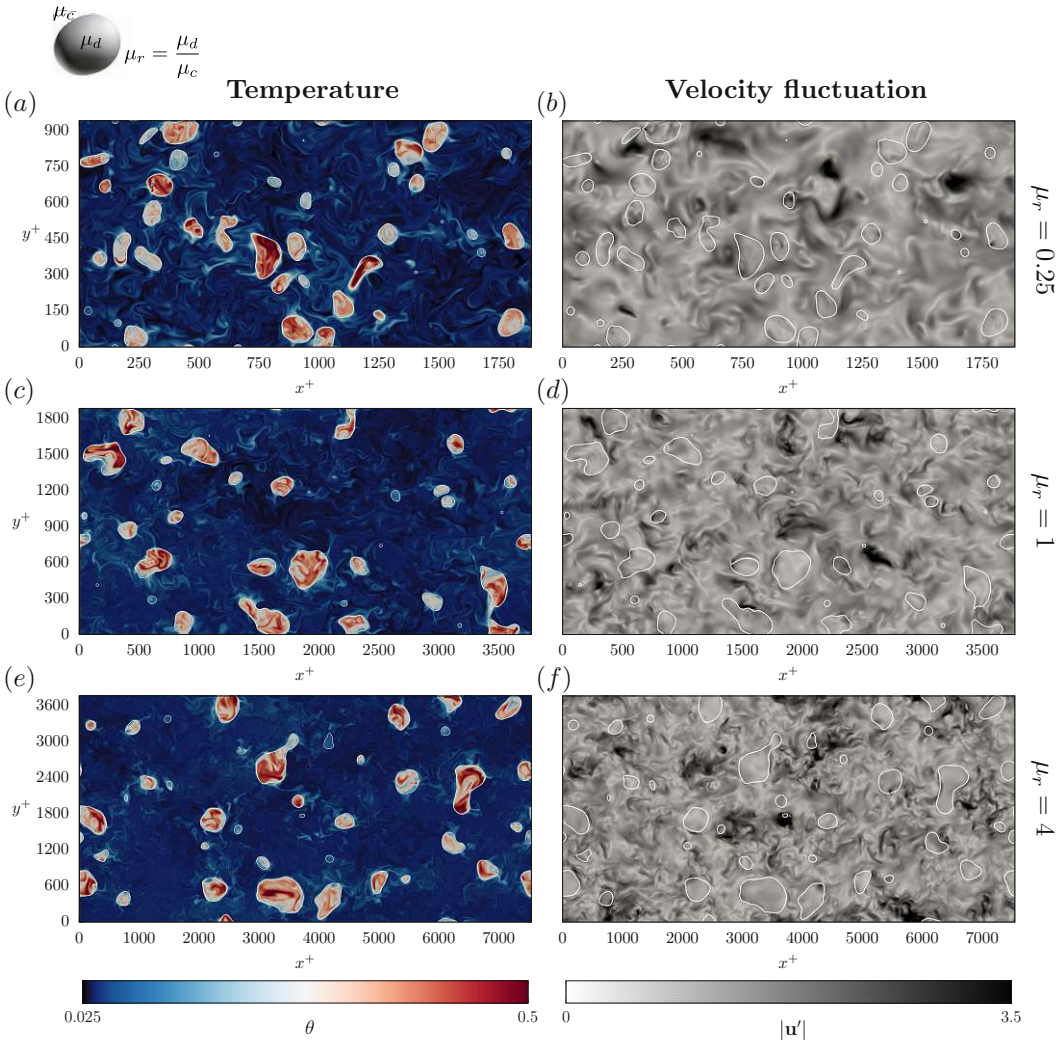

FIGURE 5.1 – Instantaneous visualizations of the temperature field (left column) and of the velocity fluctuation magnitude field (right column), for three different viscosity ratios μ_r (sketch and definition reported on the top left corner of the figure): $\mu_r = 0.25$ top row; $\mu_r = 1$ middle row; $\mu_r = 4$ bottom row. The temperature field is coloured with a blue-red scale (blue, low; red, high); the velocity fluctuation is coloured with a white-black scale (white, low; black, high). The drops interface (iso-contour $\phi = 0$) is marked by a white thin line.

Die approbierte gedruckte Originalversion dieser Dissertation ist an der TU Wien Bibliothek verfügbar.
The approved original version of this doctoral thesis is available in print at TU Wien Bibliothek.
TU Bibliothek Your knowledge hub WIEN

5.2.2 Drop size distribution

The drops dynamics is here analysed by computing the DSD at steady-state conditions. The steady state conditions are achieved approximately after $t = 6$ outer units; the DSD is obtained by averaging over a time window of $\Delta t = 5$, from $t = 7$ to 12. The steady state is evaluated by monitoring flow properties, as flow rate and wall stress, as well as drops properties like the overall drops surface area. Figure 5.2 reports the DSD obtained for the different considered cases: $\mu_r = 0.25$, representing the case of water drops in oil, is shown in blue, while $\mu_r = 4$, representing the case of oil drops in water, is shown in yellow. The reference case, $\mu_r = 1$, is reported in gray. The drop size has been characterized using the equivalent diameter, d_{eq}, i.e. the diameter of an equivalent spherical drop with the same volume as the drop considered [145]:

$$d_{eq} = \left(\frac{6V}{\pi}\right)^{1/3} \tag{5.7}$$

where V is the volume of the drop.
The three distributions are statistically similar but do not fully collapse on each other, as a trend can be slightly appreciated: as the viscosity ratio is increased, thus increasing the drops viscosity with respect to the carrier viscosity, the probability of having small drops ($d_{eq} < 0.15$ outer units) reduces, while the probability of having big drops increases. This outcome is in agreement with the reduction of drops deformability associated with an increase of viscosity, as discussed in chapter 3. In figure 5.2 the Kolmogorov-Hinze scale, d_H, is also marked for each case by a dashed line, with the colour of the corresponding DSD. The Kolmogorov-Hinze scale can be computed as

$$d_H = 0.725\left(\frac{We}{Re_\tau}\right)^{-3/5} |\epsilon_c|^{-2/5} \tag{5.8}$$

with ϵ_c the turbulent dissipation, here evaluated at the channel center where drops are mostly located. The Kolmogorov-Hinze scale slightly differ among the different cases, as they are characterized by a different shear Reynolds and turbulent dissipation. The scalings characterizing the coalescence-dominated regime, $PDF \simeq d_{eq}^{-10/3}$, and the breakage-dominated regime, $PDF \simeq d_{eq}^{-3/2}$, are reported with a dash-dotted line. Analogously to results of the DSDs obtained in section 4.2.2, our results are in agreement with the theoretical scaling law for equivalent diameters above the Kolmogorov-Hinze scale. Below the Kolmogorov-Hinze scale, our results match reasonably well the theoretical scaling law for equivalent diameters in the range $0.15 < d_{eq} < d_H$. An underestimation of the DSD with respect to the theoretical scaling law occurs instead for equivalent diameters $d_{eq} < 0.15$. This is related to the limitation of the grid resolution, and specifically to the difficulty in describing very small drops.

5.2.3 Mean temperature of drops and carrier fluid

We now characterize the heat transfer between the drops and the carrier fluid by looking at the average temperature of each fluid. Using the phase field as a phase discriminator, we compute the average temperature in the drops phase (ensamble of all drops), $\overline{\theta}_d$, and in the carrier phase, $\overline{\theta}_c$. In 5.3 the evolution in time of $\overline{\theta}_d$ and

Die approbierte gedruckte Originalversion dieser Dissertation ist an der TU Wien Bibliothek verfügbar.
The approved original version of this doctoral thesis is available in print at TU Wien Bibliothek.
TU Bibliothek Your knowledge hub WIEN

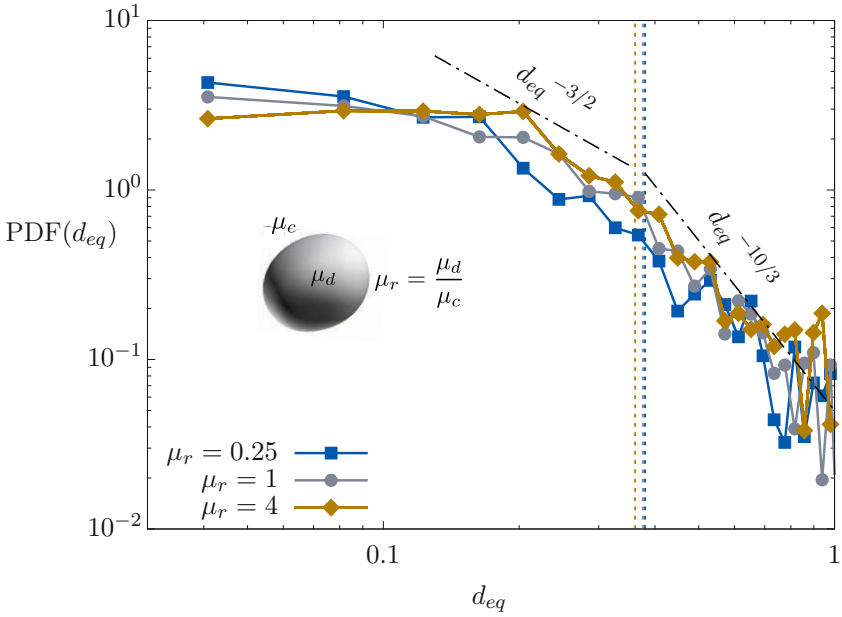

FIGURE 5.2 – Steady state DSD obtained for $\mu_r = 0.25$ (blue, squares), $\mu_r = 1$ (gray, circles) and for $\mu_r = 4$ (yellow, diamonds). The Kolmogorov-Hinze scale d_H is reported with a vertical dashed line, while the two analytical scaling laws, $d_{eq}^{-2/3}$ for the coalescence-dominated regime, and $d_{eq}^{-10/3}$ for the breakage-dominated regime, are reported with dash-dotted lines.

$\overline{\theta}_c$ are reported for the three considered cases: the colours blue, gray and yellow are associated with the water phase, the reference phase and the oil phase, respectively, for both drops and carrier fluid. For each colour, the full circle symbol indicates the drops phase, while the vertical trait symbol indicates the carrier phase. The case with water drops in an oil carrier fluid corresponds to the viscosity ratio $\mu_r = 0.25$; the case with oil drops in a water carrier fluid corresponds to the viscosity ratio $\mu_r = 4$; finally the reference case, with drops and carrier of a unspecified fluid, corresponds to the viscosity ratio $\mu_r = 1$. We notice that, as expected, the average temperature of the drops decreases in time, while the average temperature of the carrier fluid increases in time, until the thermodynamic equilibrium is asymptotically reached. At the equilibrium, the phases will have the same temperature, θ_{eq}. Since the two walls are adiabatic and the homogeneous directions are periodic, the energy of the system is conserved over time. Therefore, after some algebra, θ_{eq} can be easily estimated *a priori* as

$$\theta_{eq} = \theta_{c,0}(1 - \Phi) + \theta_{d,0}\Phi \ , \tag{5.9}$$

with $\theta_{d,0}$ and $\theta_{c,0}$ the initial temperature of the drops and of the carrier fluid, respectively, and recalling the definition of the volume fraction, $\Phi = V_d/(V_d + V_c)$. In 5.3 the equilibrium temperature is reported with a horizontal dashed line. Simulations have been run long enough for the average temperature of both phases to be sufficiently

Die approbierte gedruckte Originalversion dieser Dissertation ist an der TU Wien Bibliothek verfügbar.
The approved original version of this doctoral thesis is available in print at TU Wien Bibliothek.
TU Bibliothek Your knowledge hub WIEN

close to the equilibrium temperature, according to the following condition:

$$\frac{(\overline{\theta}_d - \theta_{eq})}{(\theta_{d,0} - \theta_{eq})} \leq 0.1\,. \tag{5.10}$$

We observe that the average temperature of the drops shows a nearly identical behaviour in the three different cases. Consequently, also the average temperature of the carrier fluid evolves with an almost identical behaviour in the three cases, as the two phases are mutually coupled (the heat released by the drops is absorbed by the carrier fluid). This outcome is in accordance with the previous qualitative observations, in relation to figure 5.1, which shows that the three cases are at a similar stage of the thermal transient. Since, however, the heat mixing appears qualitatively different in the water phases with respect to the oil phases, we attribute the identical evolution of the drops/carrier average temperature to the following reason: the mixing of heat is accelerated in the water phase and decelerated in the oil phase, with respect to the drops/carrier of the reference case, and the two effects balance each other, resulting in the same heat transfer rate. Hence, for $\mu_r = 0.25$ the mixing is faster in the drops and slower in the carrier with respect to the drops/carrier of $\mu_r = 1$, and *viceversa* for $\mu_r = 4$, where the mixing is faster in the carrier fluid and slower in the drops with respect to the drops/carrier of $\mu_r = 1$.

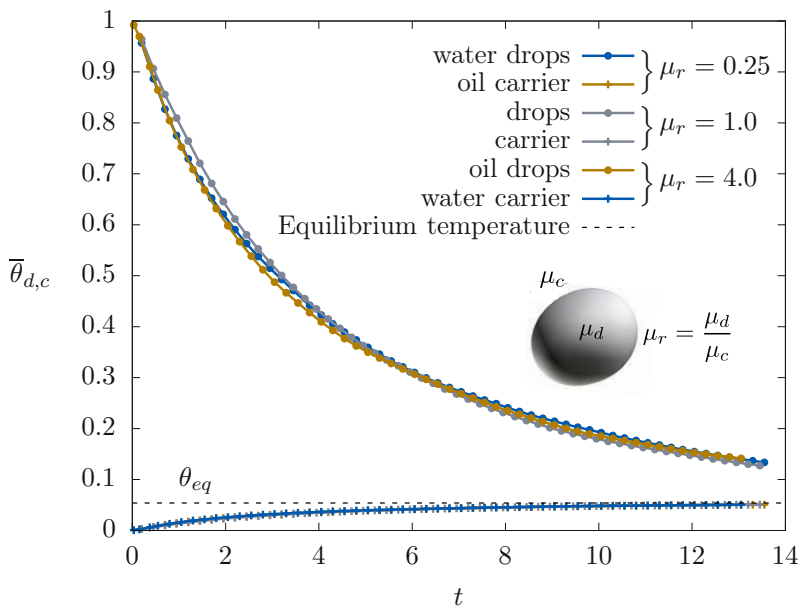

FIGURE 5.3 – Time evolution of the mean temperature of drops and carrier fluid for the different viscosity ratios considered. The water, the reference and the oil phases are reported with blue, gray and yellow lines, respectively, for both drops and carrier fluid. The drops phase are marked with a full circle symbol, while the carrier fluids are marked with a vertical trait symbol. The equilibrium temperature of the system, θ_{eq}, is reported with a horizontal dashed line.

Die approbierte gedruckte Originalversion dieser Dissertation ist an der TU Wien Bibliothek verfügbar.
The approved original version of this doctoral thesis is available in print at TU Wien Bibliothek.
TU Bibliothek Your knowledge hub WIEN

5.3 Conclusions

In this work we studied the influence of viscosity on the heat transfer in a turbulent channel flow laden with large and deformable drops. The drops are initially warmer than the carrier fluid, thus the heat is transferred from the drops to the carrier fluid until the thermodynamical equilibrium is attained, in which both fluids have the same temperature. The viscosity contrast and the Prandtl number are chosen in order to mimic an oil-water mixture, where the oil has a viscosity which is four times larger than the water. In particular, we simulate a first case where water drops are dispersed in an oil carrier fluid (with a viscosity ratio of $\mu_r = 0.25$), and a second case where oil drops are dispersed in a water carrier fluid (with a viscosity ratio of $\mu_r = 4$). For each case, a Prandtl number of $Pr = 16$ is imposed in the oil phase, while a Prandtl number of $Pr = 4$ is imposed in the water phase. In addition, a reference case with unspecified fluids is considered, characterized by $\mu_r = 1$ and $Pr = 8$. The shear Reynolds is chosen in order to maintain a constant Péclet of $Pe = 2400$ in all cases. The study is performed by means of DNS of turbulent heat transfer, coupled with a PFM for the description of the interfacial phenomena. We first investigate the drops dynamics analysing the steady-state DSD, which shows that the number of small drops ($d_{eq} < 0.15$) slightly decreases and the number of large drops slightly increases as the viscosity ratio is increased. This is due to a reduction of the drops deformability induced by an increase of the drops viscosity. Also, the DSD reasonably follows the theoretical scaling $d_{eq}^{-2/3}$ in the coalescence-dominated regime and $d_{eq}^{-10/3}$ in the breakage-dominated regime. Then we analyse the average temperature of the drops and carrier fluid. We notice that the time evolutions of the drops average temperature for the three viscosity ratios considered, as well as the evolutions of the carrier average temperature, are almost coincident. Since an increase of the viscosity is expected to reduce the heat mixing, while a decrease of the viscosity is expected to enhance the heat mixing, we attribute this outcome to the following fact: for $\mu_r = 0.25$ the enhancement of mixing in the water drops is compensated by its reduction in the oil carrier, while for $\mu_r = 4$ the opposite behaviour occurs (reduction of mixing in oil drops and enhancement of mixing in water carrier). Both cases thus result in having a drops/carrier average temperature evolution analogous to the one of the reference case. We plan to confirm this explanation with further temperature and heat transfer statistics. Moreover, future developments of this study would include more detailed statistics on the temperature and velocity field in both drops and carrier fluid, as well as an evaluation of the impact of deformation, breakage and coalescence on the heat transfer process.

Die approbierte gedruckte Originalversion dieser Dissertation ist an der TU Wien Bibliothek verfügbar.
The approved original version of this doctoral thesis is available in print at TU Wien Bibliothek.
TU Bibliothek Your knowledge hub WIEN

Die approbierte gedruckte Originalversion dieser Dissertation ist an der TU Wien Bibliothek verfügbar.
The approved original version of this doctoral thesis is available in print at TU Wien Bibliothek.
TU Bibliothek Your knowledge hub WIEN

Die approbierte gedruckte Originalversion dieser Dissertation ist an der TU Wien Bibliothek verfügbar.
The approved original version of this doctoral thesis is available in print at TU Wien Bibliothek.

6

Concluding remarks and future developments

Throughout this thesis, the dynamics and heat transfer of large and deformable drops (or bubbles) in turbulence has been studied with direct numerical simulations and phase field method. The drops dynamics in a turbulent flow has been first characterized in chapter 3, where the presence of density and viscosity contrasts between the dispersed and carrier phase has been taken into account. In particular, the role played by density and viscosity on drops topological and morphological modifications was investigated, considering also two surface tensions. Both density and viscosity have demonstrated to influence drops-turbulence interaction when the value of surface tension is sufficiently low. In this case, density and viscosity act in an opposite way on the deformability of the drop, and, for the density/viscosity ratios considered, viscosity show a stronger effect on the overall drops dynamics. Specifically, increasing the drops density slightly increases drops deformability: this effect manifests itself in an increase of the probability of large deformations (high curvatures) of the drop surface, and causes a larger global surface area. By contrast, increasing the viscosity decreases drops deformability: this reduces breakage and coalescence rates and it affects the drop shape reducing the probability of large deformations and the global drops surface area. Surface tension has a significant effect on drops behaviour in turbulence, and appears to be the only dominant parameter when sufficiently high: an increase of surface tension reduces drops deformability, strongly impacting drops dynamics from both a topological and morphological viewpoint. The presence of density and viscosity contrasts in the system, in addition, has an impact on the drops internal flow, where the turbulence intensity, as expected, depends by the properties of the drop. The drops internal flow has been analysed in terms of turbulent kinetic energy: it has been observed that an increase of density increases the turbulent kinetic energy, while a increase of viscosity reduces the turbulent kinetic energy. The study of drops-turbulence interaction is then extended in chapter 4 and in chapter 5 to the study of heat transfer within the framework of the passive scalar approximation. Both chapters investigate the heat transfer in a drop-laden turbulent flow, where warm drops release heat to the carrier fluid until the thermal equilibrium is attained. First, in chapter 4, the effect of the Prandtl number on the heat transfer process is investigated, changing the Prandtl through a change of the thermal diffusivity, and considering equal properties

of the fluids. It is found that an increase of the Prandtl number, as expected, slows down the heat transfer process. It is then observed that the time behaviour of the temperature profiles of both drops and carrier fluid is self-similar. A phenomenological model is thus developed to explain this result, and the scaling $t/Pr^{2/3}$ is introduced. Accordingly, the heat transfer coefficient H (respectively its dimensionless counterpart, the Nusselt number Nu) scales as $H \sim Pr^{-2/3}$ (respectively $Nu \sim Pr^{1/3}$) at the beginning of the simulation, and tends to $H \sim Pr^{-1/2}$ (respectively $Nu \sim Pr^{1/2}$) at later times. Finally, in chapter 5, properties contrasts are taken into account in the study of heat transfer in drop-laden turbulence, focusing on the influence of viscosity contrasts on the system. Different viscosity ratios are considered, while keeping a constant density and thermal diffusivity. In this last work the parameters are chosen in order to mimic an oil-water mixture, in which oil has a viscosity four times larger than the water. More specifically, a case with warm water drops in cold oil and a case with warm oil drops in cold water are simulated, as well as a reference case in which the two fluids have equal viscosities. Interestingly, for these cases the time behaviour of the temperature profile collapse on each other for all the viscosity ratios considered. This result is attributed to the fact that an acceleration of the heat mixing in water is compensated by a deceleration of the heat mixing in oil, thus causing an equal heat transfer rate in all the cases (the oil-water cases and the reference case).

The heat transfer, and in general the behaviour of a passive scalar, in drop-laden or bubble-laden flows, strongly depends on the turbulent flow field of the two-phase system. In particular, when the scalar transfer from the drops to the carrier fluid is considered, the turbulent flow field inside the drop and in the vicinity of the interface is crucial for the prediction of the heat transfer rate between the phases. The characterization of the drops internal turbulent flow is indeed a major future development of this thesis. In particular, understanding how turbulence is generated and forced inside the drops, and how this forcing depends on the drops thermophysical properties, would be interesting questions to investigate. Moreover, the analysis of the drops internal flow, would be valuable for the study of breakups, which are multi-scale phenomena that strongly depend on the characteristics of the turbulence around and inside the drop. A more direct follow-up of this work would be instead the study of the influence of thermal diffusivity contrasts on the heat transfer between the phases. Future investigations could also focus on assessing the role played by breakups and coalescences on the heat transfer and mixing processes.

Die approbierte gedruckte Originalversion dieser Dissertation ist an der TU Wien Bibliothek verfügbar.
The approved original version of this doctoral thesis is available in print at TU Wien Bibliothek.
TU Bibliothek Your knowledge hub WIEN

A

Wall units scaling system

In the context of wall-bounded turbulent flows, the wall unit scaling system is usually adopted. The dimensionless quantities in wall units, indicated with the superscript $^+$, can be obtained as follows

$$\mathbf{x}^+ = \frac{\mathbf{x}u_\tau}{\nu} \qquad \mathbf{u}^+ = \frac{\mathbf{u}}{u_\tau} \qquad t^+ = \frac{tu_\tau^2}{\nu} \qquad \phi^+ = \frac{\phi}{\sqrt{\beta/\alpha}}\,, \tag{A.1}$$

being $\nu = \mu_c/\rho_c$ the kinematic viscosity, with all dimensional quantities without any superscript. Considering the dimensionless quantities in outer units introduced in section 2.4, we can relate the wall units and outer units scaling systems with the following expressions:

$$\mathbf{x}^+ = Re_\tau \mathbf{x}^- \qquad \mathbf{u}^+ = \mathbf{u}^- \qquad t^+ = Re_\tau t^- \qquad \phi^+ = \phi^-\,. \tag{A.2}$$

In this thesis, results are presented in either outer units or wall units. The outer units superscripts $^-$ are dropped throughout the thesis after the dimensional analysis is presented in section 2.4, while wall units superscripts $^+$ are kept. All equations are solved in the outer units scaling system.

Die approbierte gedruckte Originalversion dieser Dissertation ist an der TU Wien Bibliothek verfügbar.
The approved original version of this doctoral thesis is available in print at TU Wien Bibliothek.

Die approbierte gedruckte Originalversion dieser Dissertation ist an der TU Wien Bibliothek verfügbar.
The approved original version of this doctoral thesis is available in print at TU Wien Bibliothek.

Die approbierte gedruckte Originalversion dieser Dissertation ist an der TU Wien Bibliothek verfügbar.
The approved original version of this doctoral thesis is available in print at TU Wien Bibliothek.

B

Effects of slip condition on the velocity and thermal boundary layer evolution

In this chapter, the equations that describe the evolution of the boundary layer are derived and solved on a heated flat plate that is parallel to a constant unidirectional flow.
In addition to the standard description of the boundary layer, where no-slip conditions on the plate are considered [127, 15], here we consider also the effect of a slip velocity on the velocity and thermal boundary layers [108, 11, 7]. Following the standard approach [142], the continuity, Navier-Stokes and energy equations in 2D are:

$$\frac{\partial u}{\partial x} + \frac{\partial v}{\partial y} = 0\,, \tag{B.1}$$

$$u\frac{\partial u}{\partial x} + v\frac{\partial u}{\partial y} = -\frac{1}{\rho}\frac{\partial p}{\partial x} + \nu\frac{\partial^2 u}{\partial y^2}\,, \tag{B.2}$$

$$u\frac{\partial T}{\partial x} + v\frac{\partial T}{\partial y} = a\frac{\partial^2 T}{\partial y^2}\,, \tag{B.3}$$

where x is the direction parallel to the wall, and y the direction normal to the wall, see figure B.1. The boundary conditions, accounting also for the slip velocity, read as:

$$u(x, y = 0) = k\frac{\partial u}{\partial y}(x, y = 0)\,, \tag{B.4}$$

$$v(x, y = 0) = 0\,, \tag{B.5}$$

$$u(x, y \to +\infty) = u_\infty\,, \tag{B.6}$$

$$T(x, y = 0) = T_w\,, \tag{B.7}$$

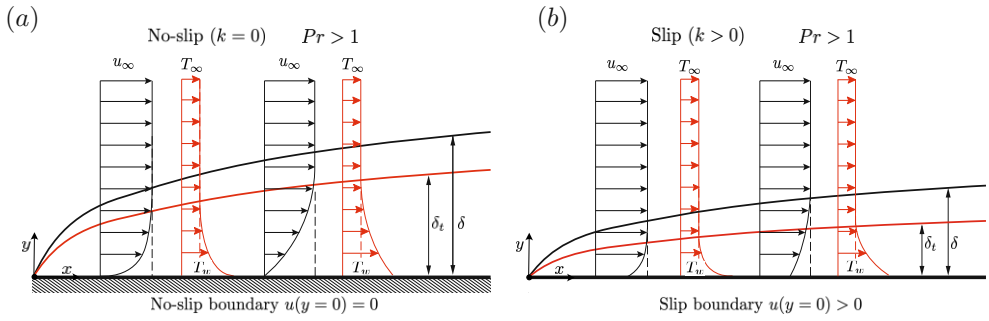

FIGURE B.1 – Sketch of the momentum and thermal boundary layer dynamics on a flat plate characterized by a uniform temperature, T_w, larger than the free stream temperature, T_∞. In panel *a* no-slip conditions are enforced at the wall (corresponding to a slip parameter $k = 0$) while in panel *b* partial slip is allowed at the wall. The qualitative behavior of the momentum and thermal boundary layer thickness is also shown for the two cases. Both panels refer to a super-unitary Prandtl number.

$$T(x, y \to +\infty) = T_\infty \,, \tag{B.8}$$

where k is a parameter that controls the amount of slip at the wall (no-slip for $k = 0$, up to free-slip for $k \to +\infty$), u_∞ and T_∞ are the free stream velocity and temperature, and T_w is the constant temperature of the flat plate.
To solve the system of equations, we use the method of similarity transformation. First, we consider the continuity and Navier-Stokes equations. Following Blasius [15], we introduce the following similarity transformation:

$$\eta = y\sqrt{\frac{u_\infty}{\nu x}} \,. \tag{B.9}$$

We can define a dimensionless stream function, $f(\eta)$, which depends only on the variable η,

$$f(\eta) = \frac{\psi(x, y)}{\sqrt{u_\infty \nu x}} \,, \tag{B.10}$$

from which we can express the two dimensionless velocity components:

$$\frac{u}{u_\infty} = f'; \qquad \frac{v}{u_\infty} = \frac{1}{2}\sqrt{\frac{u_\infty \nu}{x}}(\eta f' - f) \,, \tag{B.11}$$

where f' denotes the first derivative with respect to η (same notation is used for higher order derivatives). Upon substitution of these variables in the continuity and Navier-Stokes equations, we obtain the governing equation for the dimensionless stream function $f(\eta)$:

$$f''' + \frac{1}{2} f f'' = 0 \,, \tag{B.12}$$

Die approbierte gedruckte Originalversion dieser Dissertation ist an der TU Wien Bibliothek verfügbar.
The approved original version of this doctoral thesis is available in print at TU Wien Bibliothek.
TU Bibliothek Your knowledge hub WIEN

together with the boundary conditions:

$$f'(\eta = 0) = kf''(\eta = 0)\,, \tag{B.13}$$

$$f(\eta = 0) = 0\,, \tag{B.14}$$

$$f'(\eta \to +\infty) = 0\,. \tag{B.15}$$

Considering now the energy equation for the dimensionless temperature θ

$$\theta = \frac{T - T_\infty}{T_w - T_\infty}\,, \tag{B.16}$$

and using the similarity transformation, the governing equation for the dimensionless temperature becomes:

$$\theta'' + \frac{1}{2} Pr f \theta' = 0\,, \tag{B.17}$$

where $Pr = \nu/\alpha$ is the Prandtl number, and the following boundary conditions are applied:

$$\theta(\eta = 0) = 1\,, \tag{B.18}$$

$$\theta(\eta \to +\infty) = 0\,. \tag{B.19}$$

The governing equations B.12 and B.17, which constitute a boundary value problem, are solved numerically via a shooting method which, avoiding the imposition of the boundary condition B.6, stabilizes the computation over a wider range of η. The equations are solved for different values of k, from $k = 0$ (no-slip) up to $k = 5$, at which the velocity at the wall ($\eta = 0$) is $\simeq 70\%$ of the free stream velocity. The resulting velocity profiles, (rotated by 90 degrees to be consistent with the sketch of figure B.1) are shown in figure B.2 for different values of k . Panel a shows the effect of k on the streamwise component of the velocity, while panel b shows the effect of k on the temperature profile. All the results refer to $Pr = 1$, for which the temperature solution can be obtained as $\theta = 1 - f'$. For the no-slip case ($k = 0$), the Blasius solution (velocity and temperature, shown by the red circles) is recovered. As expected, by increasing k, the amount of slip at the plat increases. As a consequence, the temperature profiles are also modified, generating larger temperature gradients at the plate. This corresponds to an heat transfer increase, as also observed in previous studies [108, 7].

Of specific importance in the context of the model developed in the present paper, is the evaluation, as a function of the slip parameter k and for different values of Pr, of the ratio between the velocity and the thermal boundary layer thickness, respectively defined [108]:

$$\delta = \int_0^{+\infty} (1 - f')d\eta\,, \qquad \text{and} \qquad \delta_t = \int_0^{+\infty} \theta d\eta\,. \tag{B.20}$$

The ratio δ_t/δ is shown in figure B.3 as a function of Pr and for different values of the slip parameter k (different symbols). We notice that, when the no-slip condition

Die approbierte gedruckte Originalversion dieser Dissertation ist an der TU Wien Bibliothek verfügbar.
The approved original version of this doctoral thesis is available in print at TU Wien Bibliothek.
TU Bibliothek Your knowledge hub WIEN

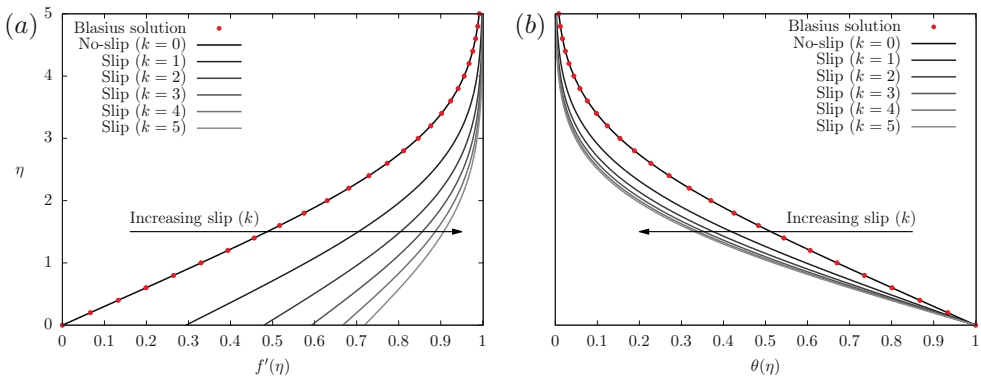

FIGURE B.2 – Streamwise velocity (panel a) and temperature profiles (panel b) obtained for different values of the slip parameter $k = 0$. Results are reported rotated by 90° degrees for sake of better interpretation and are obtained considering $Pr = 1$. For the no-slip case ($k = 0$), the classical Blasius solution available in archival literature for the velocity, f', and temperature, $\theta = 1 - f'$, is reported with red dots. By increasing the slip parameter k, velocity at the wall location $\eta = 0$ increases and larger temperature gradients are observed.

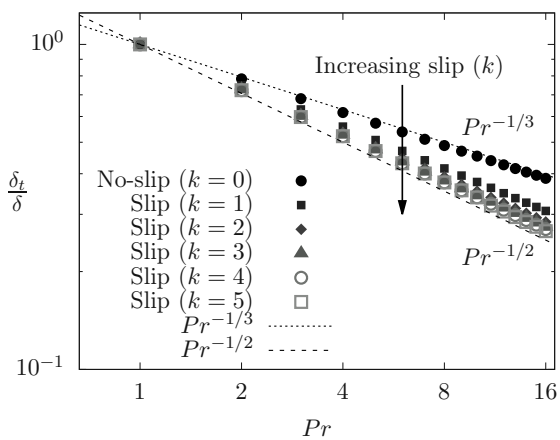

FIGURE B.3 – Ratio between the thermal and momentum boundary layer thickness as a function of the Prandtl number and the slip parameter k. The scaling laws $Pr^{-1/3}$ and $Pr^{-1/2}$ are reported as reference. Moving from $k = 0$ (no-slip) to $k = 5$ (slip), for a given value of the Prandtl number, the thermal boundary layer becomes thinner thus leading to an increase of the heat transferred from the wall.

Die approbierte gedruckte Originalversion dieser Dissertation ist an der TU Wien Bibliothek verfügbar.
The approved original version of this doctoral thesis is available in print at TU Wien Bibliothek.

is enforced ($k = 0$), the ratio $\delta_t/\delta \sim Pr^{-1/3}$, in agreement with the thermal boundary layer theory on flat plates [142]. However, when a slip condition is introduced at the wall ($k > 0$), the ratio δ_t/δ relaxes onto the scaling $\delta_t/\delta \sim Pr^{-1/2}$. This indicates that, at a given Pr, the thermal boundary layer for the slip case becomes thinner compared to the no-slip case, and the heat transfer increases. In other words, heat transfer coefficients for drops/bubbles (slip surfaces) can be higher compared to the corresponding values for solid particles (no-slip surfaces) [68]. In particular, based on the previous observations, and on the model developed in Sec. 4.2.4, we can obtain the following scalings for the heat transfer coefficients:

$$\mathcal{H}^* \propto Pr^{-2/3} \qquad \text{for no-slip,} \tag{B.21}$$

$$\mathcal{H}^* \propto Pr^{-1/2} \qquad \text{for free-slip.} \tag{B.22}$$

Die approbierte gedruckte Originalversion dieser Dissertation ist an der TU Wien Bibliothek verfügbar.
The approved original version of this doctoral thesis is available in print at TU Wien Bibliothek.
TU Bibliothek Your knowledge hub WIEN

Die approbierte gedruckte Originalversion dieser Dissertation ist an der TU Wien Bibliothek verfügbar.
The approved original version of this doctoral thesis is available in print at TU Wien Bibliothek.

Die approbierte gedruckte Originalversion dieser Dissertation ist an der TU Wien Bibliothek verfügbar.
The approved original version of this doctoral thesis is available in print at TU Wien Bibliothek.

C

Publications, Courses and Projects

C.1 Refereed journals

J1 **F. Mangani**, G. Soligo, A. Roccon and A. Soldati. Influence of density and viscosity on deformation, breakage, and coalescence of bubbles in turbulence. *Phys. Rev. Fluids*, **7**, 053601 (2022).

J2 **F. Mangani**, A. Roccon, F. Zonta and A. Soldati, *Heat transfer in drop-laden turbulence*, J. Fluid Mech., **978**, A12, (2024).

J3 **F. Mangani** and A. Soldati, *Viscosity influence on heat transfer in drop-laden turbulence*, in preparation.

J4 **F. Mangani**, L. D. Marocco, A. Schillaci and M. Quadrio, *On the role of heat transfer in the fluid mechanics of the human nose*, in preparation.

J5 **F. Mangani**, G. R. Godoberto, K. A. Schicho and F. Zonta, *Dynamics of drops containing photosensitizing agents in human upper airways*, in preparation.

C.2 Conferences

C1* **F. Mangani**†, G. Soligo, A. Roccon and A. Soldati, Density and viscosity effects on deformation, breakage and coalescence of large bubbles in turbulence, *30^{th} International Conference on Discrete Simulation of Fluid Dynamics (DSFD)*, Viterbo (Italy), September 13-17, 2021.

C2* **F. Mangani**†, G. Soligo, A. Roccon and A. Soldati, Large and deformable bubbles in wall-bounded turbulence: effects of inertial and viscous forces, *18^{th} Multiphase Flow Conference and Short Course: Simulation, Experiment and Application (MPF)*, Dresden (Germany), November 8-12, 2021.

C3 **F. Mangani**†, G. Soligo, A. Roccon and A. Soldati, Large deformable bubbles in wall-bounded turbulence: effects of inertial and viscous forces, *74^{th} APS-DFD Annual Meeting*, Phoenix (AZ, USA), November 21-23, 2021.

TU Bibliothek Your knowledge hub WIEN

C4 A. Soldati†, **F. Mangani**, G. Soligo, A. Roccon, Influence of density and viscosity on deformation, breakage and coalescence of bubbles in turbulence, *7th International Conference on Population Balance Modelling (PBM)*, Lyon (France), May 9-11, 2022.

C5 **F. Mangani**†, G. Soligo, A. Roccon and A. Soldati, Influence of density and viscosity on deformation, breakage and coalescence of bubbles in turbulence, *6th International Conference on Turbulence & Interactions (TI)*, Procchio (Elba, Italy), May 15-20, 2022.

C6 G. Soligo†, **F. Mangani**, A. Roccon and A. Soldati, Influence of density and viscosity on deformation, breakage and coalescence of bubbles in turbulence, *15th World Congress on Computational Mechanics (WCCM-XV)*, Yokohama (Japan), July 31 - August 5, 2022.

C7 **F. Mangani**†, G. Soligo, A. Roccon and A. Soldati, Influence of density and viscosity on deformation, breakage and coalescence of bubbles in turbulence, *4th International Conference on Numerical Methods in Multiphase Flow (ICNNMF-4)*, Venice (Italy), September 28-30, 2022.

C8 **F. Mangani**†, A. Roccon, F. Zonta and A. Soldati, Heat transfer in drop-laden turbulent channel flow, *75th APS-DFD Annual Meeting*, Indianapolis (IN, USA), November 20-22, 2022.

C9 **F. Mangani**†, A. Roccon, F. Zonta and A. Soldati, Heat transfer in drop-laden turbulent flows, *Treffen des Österreichisches Nationalkomitees für Theoretische und Angewandte Mechanik*, Vienna (Austria), December 2, 2022.

C10 A. Roccon†, **F. Mangani**, G. Soligo and A. Soldati, Influence of density and viscosity on deformation, breakage and coalescence of bubbles in turbulence, *11th International Conference on Multiphase Flow (ICMF)*, Kobe (Japan), April 2-7, 2023.

C11 **F. Mangani**†, A. Roccon, F. Zonta and A. Soldati, Heat transfer in drop-laden turbulent flows, *ERCOFTAC Spring festival & 31th ADA PC meeting*, Vienna (Austria), May 11-12, 2023.

C12 **F. Mangani**†, A. Roccon, F. Zonta and A. Soldati, Heat transfer in drop-laden turbulent flows, *14th Ercoftac Symposium on Engineering, Turbulence, Modelling and Measurements (ETMM14)*, Barcelona (Spain), September 6-8, 2023.

C13 **F. Mangani**†,⋆, A. Roccon, F. Zonta and A. Soldati, Heat transfer in drop-laden turbulent flows, *10th GACM Colloquium on Computational Mechanics*, Vienna (Austria), September 10-13, 2023.

C14 A. Soldati†, **F. Mangani**, A. Roccon and F. Zonta, *76th APS-DFD Annual Meeting*, Heat transfer in drop-laden turbulence, Washington (DC, USA), November 19-21, 2022.

Die approbierte gedruckte Originalversion dieser Dissertation ist an der TU Wien Bibliothek verfügbar.
The approved original version of this doctoral thesis is available in print at TU Wien Bibliothek.
TU Bibliothek Your knowledge hub WIEN

C15 **F. Mangani**‡, G. R. Godoberto, K. A. Schicho, F. Zonta and A. Soldati. Droplets inhalation and deposition in human upper airways. *1st Science Day - Faculty of Mechanical and Industrial Engineering - TU Wien*, Vienna (Austria), February 21, 2024.

* Online conference.
† Presentation speaker.
‡ Poster speaker.
⋆ Minisymposium co-organizer and co-chair.

C.3 Co-supervised projects

S1 "Dynamics of droplets in the human upper airways" - Student: Alex Werdaner (Batchelor thesis - TU Wien).

S2 "Analysis of heat transfer in drop-laden turbulent flow" - Student: Koen Mulder (Internship - Eindhoven University of Technology / TU Wien).

S3 "Voronoi tessellation of droplets in the human upper airways" - Student: Felix Stiessen (Master project - TU Wien).

S4 "Large Eddy simulation of human nasal airflow" - Student: Markus Lenarcic (Master thesis - TU Wien).

C.4 HPC projects

P1 **Effect of density and viscosity on large deformable BubbLes in tUrbulEnt flowS - BLUES**, Project ID: ISCRA B HP10BT74F1, 1 mln CPU Hours, MARCONI-100, CINECA HPC Centre, Bologna (Italy), 2021.

P2 **Viscosity stratified fluids in turbulent channel flow**, Project ID: 71026, 20 mln CPU Hours, VSC4 & VSC5, Vienna Scientific Cluster, Vienna (Austria), 2022.

P3 **BubbLe-modUlated Mixing in turbulENce - BLUMEN**, Project ID: EHPC-REG-2022R01-048, 18 mln CPU Hours, DISCOVERER, Sofia Tech, Sofia (Bulgaria), 2022.

P4 **Heat transfer in multiphase turbulence**, Project ID: EHPC-EXT-2022E01-003, 57 mln CPU Hours, LUMI-C, Finnish IT centre for science, Kajaani (Finland), 2023.

C.5 Advanced courses

A1 **Shared memory parallelization with OpenMP***, Vienna Scientific Cluster (VSC), Vienna (Austria), November 5-6, 2020. Coordinated by: Dr. Claudia Blaas-Schenner.

Die approbierte gedruckte Originalversion dieser Dissertation ist an der TU Wien Bibliothek verfügbar.
The approved original version of this doctoral thesis is available in print at TU Wien Bibliothek.
TU Bibliothek Your knowledge hub WIEN

A2 **Parallelization with MPI***, Vienna Scientific Cluster (VSC), Vienna (Austria), November 23-27, 2020. Coordinated by: Dr. Claudia Blaas-Schenner.

A3 **CUDA for dummies***, Vienna Scientific Cluster (VSC), Vienna (Austria), December 10-11, 2020. Coordinated by: Dr. Claudia Blaas-Schenner.

A4 **From Lagrangian Chaos To Turbulence In Dilute Polymer Solution***, Basque Center For Applied Mathematics, Bilbao (Spain), March 15-26, 2021. Coordinated by: Prof. I. Fouxon.

A5 **Fortran for Scientific Computing***, High Performance Computing Center (HLRS), Stuttgart (Germany), April 12-16, 2021. Coordinated by: Rolf Rabenseifner.

A6 **Parallel I/O***, Vienna Scientific Cluster (VSC), Vienna (Austria), May 18-19, 2021. Coordinated by: Dr. Claudia Blaas-Schenner.

A7 **Physics of Granular Suspensions: Micro-Mechanics of Geophysical Flows***, International Centre for Mechanical Sciences (CISM), Udine (Italy), July 14-18, 2021. Coordinated by: Prof. M. Mazzuoli and Prof. L. Lacaze.

A8 **XIV Workshop & Summer School "Multiphase Flows"**, IMP PAN, Gdańsk (Poland), September 2-3, 2021. Coordinated by: J. Pozorski.

A9 **Virtual School on Numerical Methods for Parallel CFD***, CINECA HPC Center, Bologna (Italy), December 13-27, 2021. Coordinated by: Dr. G. Amati.

A10 **Complex Flows and Complex Fluids**, International Centre for Mechanical Sciences (CISM), Udine (Italy), April 4-8, 2022. Coordinated by: Prof. F. Toschi.

A11 **Sports Physics and Technology**, International Centre for Mechanical Sciences (CISM), Udine (Italy), September 19-23, 2022. Coordinated by: Prof. C. Clanet and Prof. A. Hosoi.

A12 **CINECA GPU Hackathon*** CINECA HPC Center, Bologna (Italy), June 5,12,19-21, 2023. Coordinated by: CINECA Team.

A13 **Liquid Interfaces, Drops and Sprays**, International Centre for Mechanical Sciences (CISM), Udine (Italy), June 26-30, 2023. Coordinated by: Prof. A. Amirfazli, Prof. V. Bertola and Prof. M. Marengo.

* Online course.

Die approbierte gedruckte Originalversion dieser Dissertation ist an der TU Wien Bibliothek verfügbar.
The approved original version of this doctoral thesis is available in print at TU Wien Bibliothek.
TU Bibliothek Your knowledge hub WIEN

Bibliography

[1] A. W. Adamson and A. P. Gast. *Physical chemistry of surfaces*. Interscience publishers New York, 1967.

[2] D. L. Aksnes and J. K. Egge. A theoretical model for nutrient uptake in phytoplankton. *Mar. Ecol. Prog. Ser. Oldendorf*, 70(1):65–72, 1991.

[3] R.A. Antonia and P. Orlandi. Effect of schmidt number on small-scale passive scalar turbulence. *Appl. Mech. Rev.*, 56(6):615–632, 2003.

[4] R. Aris. *Vectors, Tensors and the Basic Equations of Fluid Mechanics*. Dover Publications, 1989.

[5] N. Ashgriz. *Handbook of atomization and sprays: theory and applications*. Springer Science & Business Media, 2011.

[6] P.S. Ayyaswamy, S.S. Sadhal, and L.J. Huang. Effect of internal circulation on the transport to a moving drop. *International communications in heat and mass transfer*, 17(6):689–702, 1990.

[7] A. Aziz, J.I. Siddique, and T. Aziz. Steady boundary layer slip flow along with heat and mass transfer over a flat porous plate embedded in a porous medium. *PloS one*, 9(12):e114544, 2014.

[8] S. Balachandar and J.K. Eaton. Turbulent dispersed multiphase flow. *Annu. Rev. Fluid Mech.*, 42:111–133, 2010.

[9] G.K. Batchelor. Small-scale variation of convected quantities like temperature in turbulent fluid Part 1. general discussion and the case of small conductivity. *J. Fluid Mech.*, 5(1):113–133, 1959.

[10] G.K. Batchelor, I.D. Howells, and A.A. Townsend. Small-scale variation of convected quantities like temperature in turbulent fluid Part 2. the case of large conductivity. *J. Fluid Mech.*, 5(1):134–139, 1959.

[11] K. Bhattacharyya, S. Mukhopadhyay, and G.C. Layek. Steady boundary layer slip flow and heat transfer over a flat porous plate embedded in a porous media. *J. Pet. Sci. Eng.*, 78(2):304–309, 2011.

[12] R.B. Bird, W.E. Stewart, and E.N. Lightfoot. *Transport Phenomena*. J. Wiley, 2002.

[13] M. Birouk and I. Gökalp. A new correlation for turbulent mass transfer from liquid droplets. *Int. J. Heat Mass Transf.*, 45(1):37–45, 2002.

Die approbierte gedruckte Originalversion dieser Dissertation ist an der TU Wien Bibliothek verfügbar.
The approved original version of this doctoral thesis is available in print at TU Wien Bibliothek.
TU Bibliothek Your knowledge hub WIEN

[14] M. Birouk and I. Gökalp. Current status of droplet evaporation in turbulent flows. *Progress in energy and combustion science*, 32(4):408–423, 2006.

[15] H. Blasius. Grenzschichten in flussigkeiten mit kleiner. *Reibung. Eng. transl. NACA TM*, 1256, 1908.

[16] D. Bothe, M. Koebe, K. Wielage, J. Prüss, and H.-J. Warnecke. *Direct numerical simulation of mass transfer between rising gas bubbles and water*. Springer, 2004.

[17] M. Bottoni and W. Sengpiel. *Review of mathematical and physical basis of two-phase flow modelling*. KfK–4759, 1992.

[18] J. Boussinesq. Calcul du pouvoir refroidissant des courants fluides. *J. Math. Pures Appl*, 1:285–332, 1905.

[19] B. Boyd and Y. Ling. A consistent volume-of-fluid approach for direct numerical simulation of the aerodynamic breakup of a vaporizing drop. *Comput. Fluids*, 254:105807, 2023.

[20] J.U. Brackbill, D.B. Kothe, and C. Zemach. A continuum method for modeling surface tension. *J. Comput. Phys.*, 335354, 1992.

[21] B. Bunner. Direct numerical simulations of three-dimensional bubbly flows. *Phys. Fluids*, 11(8), 1999.

[22] T. Jin C. Shao and K. Luo. The interaction between droplet evaporation and turbulence with interface-resolved direct numerical simulation. *Phys. Fluids*, 34(7):072102, 2022.

[23] J. W. Cahn. On spinodal decomposition. *Acta Metall.*, 9(9):795–801, 1961.

[24] J. W. Cahn. Phase separation by spinodal decomposition in isotropic systems. *J. Chem. Phys.*, 42(1):93–99, 1965.

[25] J.W. Cahn and J.E. Hilliard. Free Energy of a Nonuniform System. I. Interfacial Free Energy. *J. Chem. Phys*, 28:258–267, 1958.

[26] J.W. Cahn and J.E. Hilliard. Free Energy of a Nonuniform System. II. Thermodynamic Basis. *J. Chem. Phys*, 30(5):1121–1124, 1959.

[27] J.W. Cahn and J.E. Hilliard. Free Energy of a Nonuniform System. III. Nucleation in a Two-Component Incompressible Fluid. *J. Chem. Phys*, 31:688, 1959.

[28] I. Cannon, D. Izbassarov, O. Tammisola, L. Brandt, and M.E. Rosti. The effect of droplet coalescence on drag in turbulent channel flows. *Phys. Fluids*, 33:085112, 2021.

[29] J. C. Cano-Lozano, R Bolaños-Jiménez, C Gutiérrez-Montes, and C Martínez-Bazán. The use of volume of fluid technique to analyze multiphase flows: Specific case of bubble rising in still liquids. *Appl. Math. Model*, 39(12):3290–3305, 2015.

Die approbierte gedruckte Originalversion dieser Dissertation ist an der TU Wien Bibliothek verfügbar.
The approved original version of this doctoral thesis is available in print at TU Wien Bibliothek.
TU Bibliothek Your knowledge hub WIEN

[30] C. Canuto, M.Y. Hussaini, A.M. Quarteroni, and T.A. Zang. *Spectral Methods in Fluid Dynamics*. Springer-Verlag, 1988.

[31] S.L. Ceccio. Friction drag reduction of external flows with bubble and gas injection. *Annu. Rev. Fluid Mech.*, 42:183–203, 2010.

[32] W.H.R. Chan, P.L. Johnson, and P. Moin. The turbulent bubble break-up cascade. part 1. theoretical developments. *J. Fluid Mech.*, 912:A42, 2021.

[33] S. Chen and G. Doolen. Lattice boltzmann method for fluid flows. *Annu. Rev. Fluid Mech.*, 30(1):329–364, 1998.

[34] K.L. Chong, C.S. Ng, N. Hori, R. Yang, R. Verzicco, and D. Lohse. Extended lifetime of respiratory droplets in a turbulent vapor puff and its implications on airborne disease transmission. *Phys. Rev. Lett.*, 126(3):034502, 2021.

[35] D. Colombet, D. Legendre, A. Cockx, P. Guiraud, F. Risso, C. Daniel, and S. Galinat. Experimental study of mass transfer in a dense bubble swarm. *Chem. Eng. Sci.*, 66(14):3432–3440, 2011.

[36] D. Colombet, D. Legendre, U. Tuttlies, A. Cockx, P. Guiraud, U. Nieken, S. Galinat, and C. Daniel. On single bubble mass transfer in a volatile liquid. *Int. J. Heat Mass Transf.*, 125:1144–1155, 2018.

[37] M. Crialesi-Esposito, S. Chibbaro, and L. Brandt. The interaction of droplet dynamics and turbulence cascade. *Commun. Phys.*, 6(1):5, 2023.

[38] C.T. Crowe and C.T. Crowe. *Multiphase Flow Handbook*. CRC Press., 2005.

[39] J. C. Hermanson D. L. Albernaz, M. Do-Quang and G. Amberg. Droplet deformation and heat transfer in isotropic turbulence. *J. Fluid Mech.*, 820:61–85, 2017.

[40] G.B. Deane and M.D. Stokes. Scale dependence of bubble creation mechanisms in breaking waves. *Nature*, 418(6900):839, 2002.

[41] W.-D. Deckwer. On the mechanism of heat transfer in bubble column reactors. *Chem. Eng. Sci.*, 35(6):1341–1346, 1980.

[42] L. Deike. Mass transfer at the ocean–atmosphere interface: the role of wave breaking, droplets, and bubbles. *Annu. Rev. Fluid Mech.*, 54:191–224, 2022.

[43] L. Deike, W.K. Melville, and S. Popinet. Air entrainment and bubble statistics in breaking waves. *J. Fluid Mech.*, 801:91–129, 2016.

[44] O. Desjardins, V. Moureau, and H. Pitsch. An accurate conservative level set/ghost fluid method for simulating turbulent atomization. *J. Comput. Phys.*, 227:8395–8416, 2008.

[45] S. Di Giorgio, S. Pirozzoli, and A. Iafrati. On coherent vortical structures in wave breaking. *J. Fluid Mech.*, 947:A44, 2022.

Die approbierte gedruckte Originalversion dieser Dissertation ist an der TU Wien Bibliothek verfügbar.
The approved original version of this doctoral thesis is available in print at TU Wien Bibliothek.
TU Bibliothek Your knowledge hub WIEN

[46] M. S. Dodd, D. Mohaddes, A. Ferrante, and M. Ihme. Analysis of droplet evaporation in isotropic turbulence through droplet-resolved dns. *Int. J. Heat Mass Transf.*, 172:121157, 2021.

[47] M.S. Dodd and A. Ferrante. On the interaction of Taylor length scale size droplets and isotropic turbulence. *J. Fluid Mech.*, 806:356–412, 2016.

[48] H.A. Duguid and J.F. Stampfer Jr. The evaporation rates of small, freely falling water drops. *J. Atmos. Sci.*, 28(7):1233–1243, 1971.

[49] C.D. Eastwood, L. Armi, and J.C. Lasheras. The breakup of immiscible fluids in turbulent flows. *J. Fluid Mech.*, 502:309–333, 2004.

[50] J. Eggers. Theory of drop formation. *Phys. Fluids*, 7(5):941–953, 1995.

[51] S. Falzone, A. Buffo, M. Vanni, and D.L. Marchisio. Chapter three - simulation of turbulent coalescence and breakage of bubbles and droplets in the presence of surfactants, salts, and contaminants. In *Bridging Scales in Modelling and Simulation of Non-Reacting and Reacting Flows. Part I*, volume 52 of *Adv. Chem. Eng*, pages 125–188. 2018.

[52] P.K. Farsoiya, Q. Magdelaine, A. Antkowiak, S. Popinet, and L. Deike. Direct numerical simulations of bubble-mediated gas transfer and dissolution in quiescent and turbulent flows. *J. Fluid Mech.*, 954:A29, 2023.

[53] B. Figueroa-Espinoza and D. Legendre. Mass or heat transfer from spheroidal gas bubbles rising through a stationary liquid. *Chem. Eng. Sci.*, 65(23):6296–6309, 2010.

[54] A. Freund and A. Ferrante. Wavelet-spectral analysis of droplet-laden isotropic turbulence. *J. Fluid Mech.*, 875:914–928, 2019.

[55] N. Frössling. Über die verdunstung fallender tropfen. *Gerlands Beiträge zur Geophysik*, 52(1):170–216, 1938.

[56] X. Gao, J. Chen, Y. Qiu, Y. Ding, and J. Xie. Effect of phase change on jet atomization: a direct numerical simulation study. *J. Fluid Mech.*, 935:A16, 2022.

[57] C. Garrett, M. Li, and D. Farmer. The connection between bubble size spectra and energy dissipation rates in the upper ocean. *J. Phys. Oceanogr.*, 30(9):2163–2171, 2000.

[58] M. Gauding, F. Thiesset, E. Varea, and L. Danaila. Structure of iso-scalar sets. *J. Fluid Mech.*, 942:A14, 2022.

[59] S. M. Ghiaasiaan and G. F. Yao. A theoretical model for deposition of aerosols in rising spherical bubbles due to diffusion, convection, and inertia. *Aerosol Sci. Tech.*, 26(2):141–153, 1997.

[60] F. Gibou, R. Fedkiw, and S. Osher. A review of level-set methods and some recent applications. *J. Comput. Phys.*, 353:82–109, 2018.

Die approbierte gedruckte Originalversion dieser Dissertation ist an der TU Wien Bibliothek verfügbar.
The approved original version of this doctoral thesis is available in print at TU Wien Bibliothek.
TU Bibliothek Your knowledge hub WIEN

[61] J.R. Gissinger, A.Z. Zinchenko, and R.H. Davis. Internal circulation and mixing within tight-squeezing deformable droplets. *Phys. Rev. E*, 103:043106, Apr 2021.

[62] M. Gorokhovski and M. Herrmann. Modeling primary atomization. *Annu. Rev. Fluid Mech.*, 40:343–366, 2008.

[63] B. Gvozdić, E. Alméras, V. Mathai, X. Zhu, D.P.M. van Gils, R. Verzicco, S.G. Huisman, C.. Sun, and D. Lohse. Experimental investigation of heat transport in homogeneous bubbly flow. *J. Fluid Mech.*, 845:226–244, 2018.

[64] P.D.M. Spelt H. Ding and C. Shu. Diffuse interface model for incompressible two-phase flows with large density ratios. *J. Comput. Phys.*, 226(2):2078–2095, 2007.

[65] A. Hajisharifi, C. Marchioli, and A. Soldati. Particle capture by drops in turbulent flow. *Phys. Rev. Fluids*, 6:024303, Feb 2021.

[66] J. Hasslberger, P. Cifani, N. Chakraborty, and M. Klein. A direct numerical simulation analysis of coherent structures in bubble-laden channel flows. *J. Fluid Mech.*, 905, 2020.

[67] H. Herlina and J.G. Wissink. Direct numerical simulation of turbulent scalar transport across a flat surface. *J. Fluid Mech.*, 744:217–249, 2014.

[68] H. Herlina and J.G. Wissink. Isotropic-turbulence-induced mass transfer across a severely contaminated water surface. *J. Fluid Mech.*, 797:665–682, 2016.

[69] M. Herrmann. On Simulating Primary Atomization Using The Refined Level Set Grid Method. *Atomization Spray*, 21:283–301, 2011.

[70] N. Hidman, H. Ström, S. Sasic, and G. Sardina. Assessing passive scalar dynamics in bubble-induced turbulence using direct numerical simulations. *J. Fluid Mech.*, 962:A32, 2023.

[71] R. Higbie. The rate of absorption of a pure gas into a still liquid during short periods of exposure. *Trans. AIChE*, 31:365–389, 1935.

[72] J.O. Hinze. Fundamentals of the hydrodynamic mechanism of splitting in dispersion processes. *AIChE J.*, 1(3):289–295, 1955.

[73] N. Hiromitsu and O. Kawaguchi. Influence of flow turbulence on the evaporation rate of a suspended droplet in a hot air flow. *Heat Transf. Jap. Res.*, 24(8):689–700, 1995.

[74] C.W. Hirt and B.D. Nichols. Volume of fluid (VOF) method for the dynamics of free boundaries. *J. Comput. Phys.*, 39(1):201–225, 1981.

[75] M.Y. Hussaini and T.A. Zang. Spectral methods in fluid dynamics. *Annu. Rev. Fluid Mech.*, 19(1):339–367, 1987.

[76] M.N.J. Moore J. Mac Huang and L. Ristroph. Shape dynamics and scaling laws for a body dissolving in fluid. *J. Fluid Mech.*, 765:R3, 2015.

Die approbierte gedruckte Originalversion dieser Dissertation ist an der TU Wien Bibliothek verfügbar.
The approved original version of this doctoral thesis is available in print at TU Wien Bibliothek.
TU Bibliothek Your knowledge hub WIEN

[77] D. Jacqmin. Calculation of Two-Phase Navier–Stokes Flows Using Phase-Field Modelling. *J. Comput. Phys*, 155(1):96–127, 1999.

[78] D. Jamet, D. Torres, and J.U. Brackbill. On the theory and computation of surface tension: the elimination of parasitic currents through energy conservation in the second-gradient method. *J. Comput. Phys.*, 182(1):262–276, 2002.

[79] J.J. Jasper. The surface tension of pure liquid compounds. *J. Phys. Chem. Ref. Data*, 1(4):841–1010, 1972.

[80] D. D. Joseph. *Stability of fluid motions. I, II.* Springer Science & Business Media, 1976.

[81] J. Kamp, J. Villwock, and M. Kraume. Drop coalescence in technical liquid/liquid applications: a review on experimental techniques and modeling approaches. *Rev. Chem. Eng.*, 33(1):1–47, 2017.

[82] N. Kasagi, Y. Tomita, and A. Kuroda. Direct numerical simulation of passive scalar field in a turbulent channel flow. *J. Heat Transfer.*, 114(3):598–606, 08 1992.

[83] J. Kim and P. Moin. Transport of passive scalars in a turbulent channel flow. In *Turbulent Shear Flows 6: Selected Papers from the Sixth International Symposium on Turbulent Shear Flows, Université Paul Sabatier, Toulouse, France, September 7–9, 1987*, pages 85–96. Springer, 1989.

[84] Y. Kim, C. S. Peskin, Y. Kim, and C. S. Peskin. Numerical study of incompressible fluid dynamics with nonuniform density by the immersed boundary method. *Phys. Fluids*, 062101, 2008.

[85] A.N. Kolmogorov. The local structure of turbulence in incompressible viscous fluid for very large reynolds number. In *Dokl. Akad. Nauk SSSR*, volume 30, pages 9–13, 1941.

[86] D.J. Korteweg. Sur la forme que prennent les equations du mouvements des fluides si l'on tient compte des forces capillaires causées par des variations de densité considérables mais continues et sur la théorie de la capillarité dans l'hypothèse d'une variation continue de la densité. *Archives Néerlandaises des Sciences Exactes et Naturelles*, 6:1–24, 1901.

[87] D. Krishnamurthy and G. Subramanian. Heat or mass transport from drops in shearing flows. part 1. the open-streamline regime. *J. Fluid Mech.*, 850:439–483, 2018.

[88] J. G. Kuerten. Point-particle dns and les of particle-laden turbulent flow-a state-of-the-art review. *Flow Turbul. Combust.*, 97:689–713, 2016.

[89] F. Bianco L. Scarbolo and A. Soldati. Coalescence and breakup of large droplets in turbulent channel flow. *Phys. Fluids*, 27(7):073302, 2015.

Die approbierte gedruckte Originalversion dieser Dissertation ist an der TU Wien Bibliothek verfügbar.
The approved original version of this doctoral thesis is available in print at TU Wien Bibliothek.
TU Bibliothek Your knowledge hub WIEN

[90] J.C. Lasheras, C. Eastwood, C. Martınez-Bazán, and J.L. Montanes. A review of statistical models for the break-up of an immiscible fluid immersed into a fully developed turbulent flow. *Int. J. Multiphas. Flow*, 28(2):247–278, 2002.

[91] M. Lee and R.D. Moser. Direct numerical simulation of turbulent channel flow up to $Re_\tau \approx 5200$. *J. Fluid Mech.*, 774:395–415, 2015.

[92] V. G. Levich. *Physicochemical Hydrodynamics*. Prentice-Hall, 1962.

[93] V.G. Levich and R.J. Seeger. Physicochemical hydrodynamics. *Am. J. Phys.*, 31(11):892–892, 1963.

[94] Y. Li, J. Choi, and J. Kim. A phase-field fluid modeling and computation with interfacial profile correction term. *Commun. Nonlinear Sci.*, 30(1-3):84–100, 2016.

[95] H.-R. Liu, K.L. Chong, R. Yang, R. Verzicco, and D. Lohse. Heat transfer in turbulent rayleigh–bénard convection through two immiscible fluid layers. *J. Fluid Mech.*, 938:A31, 2022.

[96] J. Lu, A. Fernández, and G. Tryggvason. The effect of bubbles on the wall drag in a turbulent channel flow. *Phys. Fluids*, 17:095102, 2005.

[97] J. Lu, M. Muradoglu, and G. Tryggvason. Effect of insoluble surfactant on turbulent bubbly flows in vertical channels. *Int. J. Multiphas. Flow*, 95:135–143, 2017.

[98] J. Lu and G. Tryggvason. Effect of bubble size in turbulent bubbly downflow in a vertical channel. *Chem. Eng. Sci.*, 62:3008–3018, 2007.

[99] J. Lu and G. Tryggvason. Effect of bubble deformability in turbulent bubbly upflow in a vertical channel. *Phys. Fluids*, 20(4), 2008.

[100] J. Lu and G. Tryggvason. Direct numerical simulations of multifluid flows in a vertical channel undergoing topology changes. *Phys. Rev. Fluids*, 3:084401, 2018.

[101] J. Lu and G. Tryggvason. Multifluid flows in a vertical channel undergoing topology changes: Effect of void fraction. *Phys. Rev. Fluids*, 4:084301, 2019.

[102] C. Bruin M. J. P. Nijmeijer, A. F. Bakker and J. H. Sikkenk. A molecular dynamics simulation of the lennard-jones liquid-vapor interface. *J. Chem. Phys.*, 89(6):3789–3792, 1988.

[103] F. Magaletti, F. Picano, M. Chinappi, L. Marino, and C.M. Casciola. The sharp-interface limit of the Cahn–Hilliard/Navier–Stokes model for binary fluids. *J. Fluid Mech.*, 714:95–126, 2013.

[104] V. Magar and T. J. Pedley. Average nutrient uptake by a self-propelled unsteady squirmer. *J. Fluid Mech.*, 539:93–112, 2005.

Die approbierte gedruckte Originalversion dieser Dissertation ist an der TU Wien Bibliothek verfügbar.
The approved original version of this doctoral thesis is available in print at TU Wien Bibliothek.
TU Bibliothek Your knowledge hub WIEN

[105] J. Magnaudet and I. Eames. The motion of high-reynolds-number bubbles in inhomogeneous flows. *Annu. Rev. Fluid Mech.*, 32(1):659–708, 2000.

[106] F. Mangani, G. Soligo, A. Roccon, and A. Soldati. Influence of density and viscosity on deformation, breakage, and coalescence of bubbles in turbulence. *Phys. Rev. Fluids*, 7(5):053601, 2022.

[107] F. Marti, O. Martinez, D. Mazo, J. Garman, and D. Dunn-Rankin. Evaporation of a droplet larger than the kolmogorov length scale immersed in a relative mean flow. *Int. J. Multiph. Flow.*, 88:63–68, 2017.

[108] M.J. Martin and I.D. Boyd. Momentum and heat transfer in a laminar boundary layer with slip flow. *J. Thermophys. Heat Transf.*, 20(4):710–719, 2006.

[109] F. Mashayek and N. Ashgriz. Nonlinear oscillations of drops with internal circulation. *Phys. Fluids*, 10(5):1071–1082, 1998.

[110] M. Maxey. Simulation methods for particulate flows and concentrated suspensions. *Annu. Rev. Fluid Mech.*, 49:171–193, 2017.

[111] L. Méès, N. Grosjean, J.-L. Marié, and C. Fournier. Statistical lagrangian evaporation rate of droplets released in a homogeneous quasi-isotropic turbulence. *Phys. Rev. Fluids*, 5(11):113602, 2020.

[112] E.E. Michaelides. Hydrodynamic force and heat/mass transfer from particles, bubbles, and drops—the freeman scholar lecture. *J. Fluids Eng.*, 125(2):209–238, 2003.

[113] S. Mirjalili, S. S Jain, and A. Mani. A computational model for interfacial heat and mass transfer in two-phase flows using a phase field method. *Int. J. Heat Mass Transf.*, 197:123326, 2022.

[114] S. Mukherjee, A. Safdari, O. Shardt, S. Kenjereš, and H. E. A. Van den Akker. Droplet-turbulence interactions and quasi-equilibrium dynamics in turbulent emulsions. *J. Fluid Mech.*, 878:221–276, 2019.

[115] R. Ni. Deformation and breakup of bubbles and drops in turbulence. *Annu. Rev. Fluid Mech.*, 56:319–47, 2024.

[116] Y. Ohta, K. Shimoyama, and S. Ohigashi. Vaporization and combustion of single liquid fuel droplets in a turbulent environment. *Bulletin of JSME*, 18(115):47–56, 1975.

[117] S. Osher and R. Fedkiw. Level set methods: An overview and some recent results. *J. Comput. Phys.*, 169(2):463–502, 2001.

[118] S. Popinet P. K. Farsoiya and L. Deike. Bubble-mediated transfer of dilute gas in turbulence. *J. Fluid Mech.*, 920:A34, 2021.

[119] C. Liu P. Yue, J. Feng and J. Shen. A diffuse-interface method for simulating two-phase flows of complex fluids. *J. Fluid Mech.*, 515:293–317, 2004.

Die approbierte gedruckte Originalversion dieser Dissertation ist an der TU Wien Bibliothek verfügbar.
The approved original version of this doctoral thesis is available in print at TU Wien Bibliothek.
TU Bibliothek Your knowledge hub WIEN

[120] F. Pelusi, S. Ascione, M. Sbragaglia, and M. Bernaschi. Analysis of the heat transfer fluctuations in the Rayleigh-Bénard convection of concentrated emulsions with finite-size droplets. *Soft Matter*, 19, 2023.

[121] P. Perlekar, L. Biferale, and M. Sbragaglia. Droplet size distribution in homogeneous isotropic turbulence. *Phys. Fluids*, 065101:1–10, 2012.

[122] R. Peyret. *Spectral Methods for Incompressible Viscous Flow*. Springer Science+Business Media, 2002.

[123] S. Pirozzoli, M. Bernardini, and P. Orlandi. Passive scalars in turbulent channel flow at high reynolds number. *J. Fluid Mech.*, 788:614–639, 2016.

[124] S. Pirozzoli, J. Romero, M. Fatica, R. Verzicco, and P. Orlandi. One-point statistics for turbulent pipe flow up to. *J. Fluid Mech.*, 926:A28, 2021.

[125] S.B. Pope. *Turbulent flows*. Cambridge university press, 2000.

[126] S. Popinet. Numerical models of surface tension. *Annu. Rev. Fluid Mech.*, 50:1–28, 2018.

[127] L. Prandtl. Uber flussigkeitsbewegung bei sehr kleiner reibung. *Verhandl. 3rd Int. Math. Kongr. Heidelberg (1904), Leipzig*, 1905.

[128] A. Prosperetti and G. Tryggvason. *Computational Methods for Multiphase Flow*. Cambridge University Press, 2009.

[129] Y. Qi, S. Tan, N. Corbitt, C. Urbanik, A. K. R. Salibindla, and R. Ni. Fragmentation in turbulence by small eddies. *Nat. Commun.*, 13(1):469, 2022.

[130] W. E. Ranz. Evaporation from drops-i and-ii. *Chem. Eng. Progr*, 48:141–146, 1952.

[131] L. Rekvig and D. Frenkel. Molecular simulations of droplet coalescence in oil/water/surfactant systems. *J. Chem. Phys.*, 127(13):134701, 2007.

[132] A. Roccon, M. De Paoli, F. Zonta, and A. Soldati. Viscosity-modulated breakup and coalescence of large drops in bounded turbulence. *Phys. Rev. Fluids*, 2:083603, 2017.

[133] A. Roccon, F. Zonta, and A. Soldati. Turbulent drag reduction by compliant lubricating layer. *J. Fluid Mech.*, 863:R1, 2019.

[134] A. Roccon, F. Zonta, and A. Soldati. Energy balance in lubricated drag-reduced turbulent channel flow. *J. Fluid Mech.*, 911, 2021.

[135] A. Roccon, F. Zonta, and A. Soldati. Phase-field modeling of complex interface dynamics in drop-laden turbulence. *Phys. Rev. Fluids*, 8:090501, Sep 2023.

[136] E. Russo, J. G. Kuerten, C. Van Der Geld, and B. J. Geurts. Water droplet condensation and evaporation in turbulent channel flow. *J. Fluid Mech.*, 749:666–700, 2014.

Die approbierte gedruckte Originalversion dieser Dissertation ist an der TU Wien Bibliothek verfügbar.
The approved original version of this doctoral thesis is available in print at TU Wien Bibliothek.
TU Bibliothek Your knowledge hub WIEN

[137] W. Mostert S. Perrard, A. Rivière and L. Deike. Bubble deformation by a turbulent flow. *J Fluid Mech.*, 920:A15, 2021.

[138] N. Scapin, F. Dalla Barba, G. Lupo, M. E. Rosti, C. Duwig, and L. Brandt. Finite-size evaporating droplets in weakly compressible homogeneous shear turbulence. *J. Fluid Mech.*, 934:A15, 2022.

[139] L. Scarbolo, F. Bianco, and A. Soldati. Turbulence modification by dispersion of large deformable droplets. *Eur. J. Mech. B-Fluid*, 55:294–299, 2016.

[140] L. Scarbolo, F. Bianco, and A. Soldati. Turbulence modification by dispersion of large deformable droplets. *Eur. J. Mech. B/Fluids*, 55:294–299, 2016.

[141] L. Scarbolo and A. Soldati. Turbulence modulation across the interface of a large deformable drop. *J. Turbul.*, 14:27–43, 2013.

[142] H. Schlichting and K. Gersten. *Boundary-Layer Theory*. Springer Berlin Heidelberg, 2016.

[143] G. Segré and a. Silberberg. Behaviour of macroscopic rigid spheres in Poiseuille flow Part 1. Determination of local concentration by statistical analysis of particle passages through crossed light beams. *J. Fluid Mech.*, 14(01):115, 1962.

[144] A. Soldati and S. Banerjee. Turbulence modification by large-scale organized electrohydrodynamic flows. *Phys. Fluids*, 10(7):1742–1756, 1998.

[145] G. Soligo, A. Roccon, and A. Soldati. Breakage, coalescence and size distribution of surfactant-laden droplets in turbulent flow. *J. Fluid Mech.*, 881:244–282, 2019.

[146] G. Soligo, A. Roccon, and A. Soldati. Coalescence of surfactant-laden drops by Phase Field Method. *J. Comput. Phys.*, 376:1292–1311, 2019.

[147] G. Soligo, A. Roccon, and A. Soldati. Mass conservation improved Phase Field Methods for turbulent multiphase flow simulation. *Acta Mech.*, 230:683–696, 2019.

[148] G. Soligo, A. Roccon, and A. Soldati. Effect of surfactant-laden droplets on turbulent flow topology. *Phys. Rev. Fluids*, 5(7):073606, 2020.

[149] G. Soligo, A. Roccon, and A. Soldati. Turbulent flows with drops and bubbles: what numerical simulations can tell us – freeman scholar lecture. *ASME J. Fluids Eng.*, 143:080801–1, 2021.

[150] Y. Sun and C. Beckermann. Sharp interface tracking using the phase-field equation. *J. Comput. Phys.*, 220(2):626–653, 2007.

[151] P. Than, L. Preziosi, D.D. Joseph, and M. Arney. Measurement of interfacial tension between immiscible liquids with the spinning road tensiometer. *J. Colloid Interface Sci.*, 124(2):552 – 559, 1988.

Die approbierte gedruckte Originalversion dieser Dissertation ist an der TU Wien Bibliothek verfügbar.
The approved original version of this doctoral thesis is available in print at TU Wien Bibliothek.
TU Bibliothek Your knowledge hub WIEN

[152] T.G. Theofanous, R.N. Houze, and L.K. Brumfield. Turbulent mass transfer at free, gas-liquid interfaces, with applications to open-channel, bubble and jet flows. *Int. J. Heat Mass Transf.*, 19(6):613–624, 1976.

[153] G. Tryggvason, B. Bunner, A. Esmaeeli, D. Juric, W. Tauber, J. Han, S. Nas, and Y. Jan. A front-tracking method for the computations of multiphase flow. *J. Comput. Phys.*, 759:708–759, 2001.

[154] S.and Aboulhasanzadeh B. Tryggvason, G.and Dabiri and J. Lu. Multiscale considerations in direct numerical simulations of multiphase flows. *Phys. Fluids*, 25(3):031302, 2013.

[155] S. Unverdi and G. Trygvasson. A Front-Tracking Method for Viscous , Incompressible , Multi-fluid Flows. *J. Comput. Phys.*, 100(1), 1992.

[156] H. D. Ceniceros V. E. Badalassi and S. Banerjee. Computation of multiphase systems with phase field models. *J. Comput. Phys*, 190(2):371–397, 2003.

[157] D.P.M. van Gils, D. Narezo Guzman, C. Sun, and D. Lohse. The importance of bubble deformability for strong drag reduction in bubbly turbulent Taylor–Couette flow. *J. Fluid Mech.*, 722:317–347, 2013.

[158] A. Vela-Martín and M. Avila. Memoryless drop breakup in turbulence. *Sci. Adv.*, 8(50):eabp9561, 2022.

[159] A. Vela-Martín and M. Avila. Deformation of drops by outer eddies in turbulence. *J Fluid Mech.*, 929:A38, 2021.

[160] R.A. Verschoof, R.C.A. Van Der Veen, C. Sun, and D. Lohse. Bubble drag reduction requires large bubbles. *Phys. Rev. Lett.*, 117(10):104502, 2016.

[161] T. Von Kármán. Mechanical similitude and turbulence. *Reprint from Nachrichten von der Gesellschaft der Wissenschaften zu Gottingen*, 1931.

[162] J. Wang, M. Alipour, G. Soligo, A. Roccon, M. De Paoli, F. Picano, and A. Soldati. Short-range exposure to airborne virus transmission and current guidelines. *Proc. Natl. Acad. Sci. U.S.A.*, 118(37):e2105279118, 2021.

[163] J. Wang, F. Dalla Barba, and F. Picano. Direct numerical simulation of an evaporating turbulent diluted jet-spray at moderate reynolds number. *Int. J. Multiph. Flow .*, 137:103567, 2021.

[164] R. Wanninkhof. Relationship between wind speed and gas exchange over the ocean. *J. Geophys. Res.*, 97(C5):7373–7382, 1992.

[165] S. Whitaker. Forced convection heat transfer correlations for flow in pipes, past flat plates, single cylinders, single spheres, and for flow in packed beds and tube bundles. *AIChE J.*, 18(2):361–371, 1972.

[166] J.-S. Wu, K.-H. Hsu, P.-M. Kuo, and H.-J. Sheen. Evaporation model of a single hydrocarbon fuel droplet due to ambient turbulence at intermediate reynolds numbers. *Int. J. Heat Mass Transf.*, 46(24):4741–4745, 2003.

Die approbierte gedruckte Originalversion dieser Dissertation ist an der TU Wien Bibliothek verfügbar.
The approved original version of this doctoral thesis is available in print at TU Wien Bibliothek.
TU Bibliothek Your knowledge hub WIEN

[167] P. Yue, C. Zhou, and J.J. Feng. Spontaneous shrinkage of drops and mass conservation in phase-field simulations. *J. Comput. Phys.*, 223(1):1–9, 2007.

[168] Y. Zhang and W. Ye. A Flux-Corrected Phase-Field Method for Surface Diffusion. *Commun. Comput. Phys.*, 22(2):422–440, 2017.

[169] X. Zheng, H. Babaee, S. Dong, C. Chryssostomidis, and G.E. Karniadakis. A phase-field method for 3d simulation of two-phase heat transfer. *Int. J. Heat Mass Transf.*, 82:282–298, 2015.

[170] F. Zonta, C. Marchioli, and A. Soldati. Modulation of turbulence in forced convection by temperature-dependent viscosity. *J. Fluid Mech.*, 697:150–174, 2012.

[171] F. Zonta, M. Onorato, and A. Soldati. Turbulence and internal waves in stably-stratified channel flow with temperature-dependent fluid properties. *J. Fluid Mech.*, 697:175–203, 2012.

[172] F. Zonta and A. Soldati. Effect of temperature-dependent fluid properties on heat transfer in turbulent mixed convection. *J. Heat Transfer - Trans. ASME*, 136:022501, 2014.

Die approbierte gedruckte Originalversion dieser Dissertation ist an der TU Wien Bibliothek verfügbar.
The approved original version of this doctoral thesis is available in print at TU Wien Bibliothek.
TU Bibliothek Your knowledge hub WIEN